

國立交通大學
土木工程學系
博士論文

以空載光達資料進行台灣地區山崩型態測計之研究

Characterizing Morphologic Features of Taiwan
Landslides with Airborne LiDAR Data



研究生：劉進金

指導教授：史天元

中華民國一〇二年一月

以空載光達資料進行台灣地區山崩型態測計之研究

**Characterizing Morphologic Features of
Taiwan Landslides with Airborne LiDAR Data**

研究生：劉進金

Student: Jin-King Liu

指導教授：史天元 博士

Advisor: Dr. Tian-Yuan Shih

國立交通大學
土木工程學系
博士論文



**A Dissertation
Submitted to Department of Civil Engineering
College of Engineering**

**National Chiao Tung University
in Partial Fulfillment of the Requirements
for the Degree of
Doctor of Philosophy
in
Civil Engineering**

**January 2013
Hsinchu, Taiwan, Republic of China**

中華民國一〇二年一月

以空載光達資料進行台灣地區山崩型態測計之研究

學生：劉進金

指導教授：史天元

國立交通大學土木工程學系博士班

摘 要

空載光達資料可用於各種淺層與深層山崩之探討。雖然空載光達資料為山崩研究開啟嶄新的一頁，但是由於許多新的分析方法有待開發，所以尚未成為普遍使用的工具。空載光達資料用於山崩研究主要可分為三方面：（1）山崩偵測，經由光達資料辨認山崩並且清點山崩的分佈特性與幾何特性，並可進而進行山崩潛感性分析；（2）山崩監測，經由多期光達資料分析山崩的變動或山崩的體積及其變化；（3）山崩辨認或山崩變動模型建立，經由光達資料產生之山崩型態測計參數建立預測與評估模式。本研究之目的即針對這三個山崩研究面向分別提出分析方法，並選擇台灣的案例進行實驗：（1）山崩辨識，以專家法與半自動法，進行台灣北部與南部之淺層山崩與深層山崩案例之探討；（2）山崩監測，提出個體山崩體積與全區山崩體積估算法，對高雄市案例進行個體深層山崩與區域性淺層山崩體積之估算；（3）山崩自動萃取建模，利用光達資料產生之山崩型態測計參數，以高雄市案例建立預測與評估模式。結果顯示，本研究所提出之各種光達山崩分析法均有其可行性，空載光達資料確實對於各種淺層與深層山崩之探討均有其效用。

首先，為了解空載光達技術用於山崩研究之潛力與限制，本論文首先彙整用於型態測計的重要的山崩分類與幾何特徵，進而對空載光達技術應用於台灣山崩的經驗予以審視。並分別就空載光達技術在山崩研究應用上的主要有利與不利因素加以探討。以申論空載光達資料用於山崩研究隱含之基本問題。

在淺層山崩辨識的探討上，本研究提出的方法包括（1）專家法：包括數值表面模型暈渲法與數值高程模型暈渲法；（2）半自動法：包括點雲密度指標法與物件導向分析法；與（3）自動法：本研究提出一個混合影像分割與物件導向法，並以傳統逐像元方式的分類法比較。在深層山崩辨識的探討上，本研究提出的方法包括（1）專家法；（2）半自動法：影像組織分析與物件導向分析法；（3）多期光達變動分析法：以三期光達資料檢視深層山崩之活動性。專家法分別以數值表面模型暈渲圖及數值高程模型暈渲圖作為專家判釋的依據，結果顯示淺層山

崩判釋上，數值表面模型暈渲法優於數值高程模型暈渲法；相反地，深層山崩判釋上，反映林木遮蔽下之微地形的數值高程模型暈渲圖優於數值高程模型暈渲圖。半自動法先進行光達影像增揚處理 (enhancement)，產生之結果再由地質專家進一步分析判釋。光達點雲密度指標法提出四種光達點雲密度指標及其計算方法，其處理結果再與正規化數值表面模型暈渲法 (nDSM-shaded relief) 專家判釋成果進行比較，結果顯示問題的關鍵在於點雲密度指標之參數的選擇。物件導向分析法以區域影像分割法 (area-based segmentation) 產生物件再以支持向量機法 (SVM) 完成分類，分類結果分別與傳統逐像元分類法 (pixel-based method) 及專家判釋成果進行比較，結果顯示整體精度達 93.4%，Kappa 係數達 0.817，物件導向法優於傳統逐像元分類法。至於深層山崩，利用影像組織分析與物件導向分析法進行之山崩活動性探討，本研究顯示台灣的地質與地形環境的複雜度在這方法仍有很大探討空間。在多期光達變動分析上，本研究以簡單數值高程模型差異法檢視三期光達資料，確實可以觀察到深層山崩之活動性。

在山崩體積估計的探討上，本研究提出兩種山崩體積估計方案，全區性山崩體積評估的方法包括：簡易數值高程模型相減法 (Difference of DEMs, 簡稱 Simple DoD Method) 與個體山崩體積累計法；個體山崩體積評估的方法包括：山崩三維斷面法、平均切片法、與網格式法等。本研究以小林山崩及高雄市納馬夏區之一個圖幅進行實例示範。此外，一個山崩圖幅之個別山崩可予以分割，從而產生每一個山崩的精確體積，因而可以進而探討山崩之面積 A (m^2) 與體積 V (m^3) 的冪次法則關係式， $V = kA^a$ 。本研究納馬夏案例，獲得 $k = 0.099$ ， $a = 1.395$ ，相關係數 $R^2 = 83.7\%$ 。此冪次法則可以反映不同地質、土壤、與風化侵蝕的特性。

在山崩自動萃取模式的建立上，本研究利用 2005 年與 2009 年兩期的光達資料建立一個山崩自動萃取的山崩型態測計模式。首先利用研究區的衛星影像進行自動山崩分類，其後以專家法，逐一檢視與修正山崩分佈圖。利用山崩分佈圖作為切割版，萃取發生山崩地區之光達山崩型態測計參數如坡度、地形曲率、物件高程模式 (OHM)、OHM 粗糙度、與地形濕度指數等。再統計產生山崩型態測計參數之區間值，由而建立一個二元多評準決策模式，此為一線性組合模式，所有落入山崩型態測計參數之區間值範圍者即為山崩。結果顯示此山崩模式之整體精度為 64.9%。當進一步考慮將舊山崩區與河岸區納入，精度為 64.4%，並沒有改善。當排除面積小於 $50m^2$ (即小於 $10m \times 5m$) 之山崩時，2005 年與 2009 年之山崩預測精度分別成為 76.6% 與 72.5%，有明顯改善。成果顯示此山崩型態測計模式是有效的，唯型態測計參數的選擇與參數區間值的產生仍值得進一步探討。

總結而言，本研究針對空載光達資料用於山崩研究之三個面向分別提出分析方法，並選擇案例進行實驗，結果顯示本研究提出之方法可行，空載光達資料確

實是山崩研究有用的工具。中央地質調查所在 2009 年莫拉克風災後推動全國光達測繪計畫，期間從 2010 年至 2015 年，其目的在獲取全區之一公尺解析力之光達數值表面模型(DSM) 與數值高程模型 (DEM)、以及 0.5 公尺解析力之正攝影像。這可提供未來多期體積變化研究的基準，亦可提供本研究後續之應用與探討，以了解不同地文環境之適用性。此外，因為森林覆蓋下深層山崩不易被察覺，值得進一步開發半自動化的物建導向分析法予以探討。森林覆蓋區是多期變動監測之誤差主要來源，光達全光譜分析用於萃取森林底層較微弱的反射訊號，以增加森林地區數值高程模型的精度，並降低多期變動監測的不確定性，值得進一步探討。未來也可以考慮加入山崩誘因作為參數，併入本研究提出之山崩模式。

關鍵詞：遙測、自然災害、地形測計、影像增揚、國家空間資訊基礎建設。



Characterizing Morphologic Features of Taiwan Landslides with Airborne LiDAR Data

Student : Jin-King Liu

Advisors : Dr. Tian-Yuan Shih

Department of Civil Engineering

National Chiao Tung University

ABSTRACT

Taiwan is located on the active collision zone between the Eurasian plate and the Philippine Sea plate. Mountains have a high relief, and rock formations are highly fractured and fragile. These physiographic settings are unfavorable to landslide susceptibility. LiDAR-derived data can be used to investigate any type of landslides including both shallow and deep-seated ones. Nevertheless, LiDAR data are not yet a common tool for landslides investigations though this technique has opened new domains of applications that still have to be developed. Applications of LiDAR in landslide investigations can be classified as: (1) Detection and characterization of landslides which include the recognition of landslides and their subsequent application in susceptibility analysis; (2) Monitoring of displacement or volume change of landslide bodies; (3) Modeling for the movement of landslides or the automatic extraction of landslides. The purposes of this research are to develop methods for understanding all these 3 aspects: (1) Landslide recognition for both shallow and deep-seated landslides with expert-based and semi-automatic approaches with cases from northern and southern Taiwan; (2) Landslide volume estimation for both shallow and deep-seated landslides with multi-temporal LiDAR data in southern Taiwan; and (3) Modeling landslide extraction with 6 geomorphometric features including slope, curvature, OHM (object height model), OHM roughness, and topographic wetness index which are derived from multi-temporal LiDAR data acquired in 2005 and 2009 in southern Taiwan.

For exploring the prospects and limitations of LiDAR Technology, the significant classification scheme and landslide features are concisely reviewed. Subsequently, both favorable and adverse factors of applying LiDAR data for landslide investigation are discussed on basis of the experiences gained so far in Taiwan. It is concluded that the awareness of the adverse factors is critical in using the LiDAR products for landslide investigations..

In the experiment of landslide detection by indices of LiDAR point-cloud density, classification results from the indices derived from the proposed four kinds of densities are verified by the result obtained by manual interpretation of the derived nDSM images. The datasets for this study are in I-Lan County after Typhoon Kalmaegi on 17 July 2008. The results show that a proper definition of the parameters for the indices is most critical for the detection of shallow landslides. Landslides recognition of the same area was also done by a pixel-based method and an object-oriented method combining area-based segmentation and a Supported Vector Machine (SVM) method. The geomorphometric features applied in the classification include Slope, OHM, and Shaded Relief which are derived from LiDAR data , as well as features of RGB, Greenness, and NDVI which are derived from concurrent images. This case shows the object-oriented SVM method is better than a pixel-based SVM method in classification accuracy and the most important features include slope and OHM. In addition, deep-seated landslide under forest can be detected in this area under expert-based shaded-relief analysis of micro-morphology.

In the experiment of landslide volume change with multi-temporal LiDAR data acquired in 2005 and 2010 in southern Taiwan, both regional approach and approach of individual landslides for volume estimation are raised. For the estimation of regional sedimentation, two methods are proposed: (1) a simple DoD method; (2) Method of Accumulating Individuals. For the estimation of each individual landslide, three methods are proposed: (1) Method of 3D Sections; (2) Method of Average Sections; and (3) Grid Method. These methods are tested with a deep-seated landslide (Hsiaolin Landslide) and with a selected map-sheet area in Namashia District of

Kaohsiung City. Because the area and volume of each individual landslide in an area can be estimated, it is straightforward to model the relation between A (m^2) and volume V (m^3) of landslides, $V = kA^a$. The result of the Ternbausan-One area shows that $k = 0.099$, $a = 1.395$, and R-squared coefficient of determination = 83.7%. The empirical formula reflects different physiographic conditions including geology, soils, climate and denudation processes.

In the experiment of establishing a geomorphological model for extracting landslides using multi-temporal LiDAR data of high accuracy and high resolution. Two sets of LiDAR data were acquired for before and after a heavy rainfall event. The landslides which took place from 2005 to 2009 were classified automatically by satellite images, and subsequently the landslides were interpreted and edited manually. Geomorphometric parameters including slope, curvature, OHM, OHM roughness, and topographic wetness index were then extracted using stencils of landslide polygons overlaid on respective thematic maps derived from LiDAR, DEM and DSM. The ranges of every parameter were derived from the statistics of the landslide area. Some selected non-morphometric parameters were also included in a later stage to account for all possible features of landslides, such as vegetation index and geological strength. The ranges of the parameters of landslides were optimized for the model by the statistics of the landslide area. The overall accuracy predicted by the model was 64.9%. When the buffer zones of old landslides and riverside areas were included, the overall accuracy was 64.4%, showing no improvement. When landslides smaller than 50 m^2 were filtered, the overall accuracy reached 76.6% and 72.5% for 2005 and 2009, respectively. The results show that the geomorphological model proposed in this research is effective for landslide extraction.

In conclusion, the methods developed in this research for landslide detection, for multi-temporal volume change analysis, and for establishing a landslide extracting model are proved to be effective for the cases in Taiwan and for the airborne LiDAR data acquired. Generally, LiDAR data can be a good tool for landslides investigations. A national geohazard mapping program employing integrated airborne LiDAR and

digital photography was launched by the Central Geological Survey after Typhoon Morakot hit southern Taiwan in 2009. The national mapping program, spanning 2010 to 2015, was dedicated to capture an entire territory of the country with airborne LiDAR and digital imagery. More datasets of multi-temporal and various physiographical settings are becoming available. Technique of OOA segmentation method for the detection of deep-seated landslides in dense forest should be developed especially for the high relief terrain of Taiwan. Other research topics include uncertainties of LiDAR analysis, the dependence of morphometric parameters on triggering events or geographical locations, and full waveform for detect the subtle reflection from the forest floor, thus to increase ground point densities of densely-vegetated area and to suppress the uncertainties of the DEM in this environment.

Keywords: remote sensing, natural hazards, geomorphometry, image enhancement, NSDI



DEDICATION

This dissertation is dedicated to the memory
of my beloved father, Liu Ma-Hsiang (1910-1993)
and mother, Liu Jhuang-Hsio (1916-2008)
for their love, humble, and hard-work in raising 7 children:

Jin-Tsai Liu, Jin-Shi Liu,
Jin-Cheng Liu, Jin-Shing Liu,
Yue-Mei Liu, Me and Chiu-Guei Hsu.



ACKNOWLEDGEMENTS

Many people have contributed to my success in completing this dissertation, especially my family, my advisor Prof. Tian-Yuan Shih, the outstanding committee members for reviewing my dissertation, my colleagues in Industrial Technology Research Institute (ITRI) and in LIDAR Technology Co. Ltd., and peers of professional geo-infomatics worldwide.

I am fortunate to have an outstanding committee for reviewing my dissertation including Prof. Dr. Liang-Chien Chen, Prof. Dr. Chyi-Tyi Lee, Associate Prof. Dr. Yu-Chang Chan, Prof. Dr. Jyh-Jong Liao, Prof. Dr. Cheinway Hwang, Associate Prof. Dr. Tee-Ann Teo, and Prof. Dr. Tian-Yuan Shih.

I have been involved in the profession of remote sensing and photogrammetry since my first job in 1977 when I enrolled to the newly-established remote sensing group in Mining Research and Service Organization of ITRI. I started with aerial photo-interpretation for geological applications. With the advancement of the technology, Prof. Shih cooperated with ITRI introduced airborne LiDAR technology to Taiwan after the major disaster JiJi Earthquake in 1999. Subsequently, with supports by National Chiao Tung University, National Central University, National Taiwan University, and National Cheng Kung University, ITRI started an operational experiment of airborne LiDAR from 2004 to 2006 and introduced this new technology to the industry of Taiwan with sponsorship of the Ministry of the Interior, Republic of China (Taiwan). In 2005, Dr. Yu-Chang Chan of Institute of Earth Sciences, Academia Sinica coordinated with ITRI and Chung-Hsing Survey Company initiated a geological study using airborne LiDAR with sponsorship of Central Geological Survey. The study continued from March 2005 till December 2010. The effectiveness and significance of airborne LiDAR for geological study have been explored and validated by this 7-years 2 phases of study. Thus, after Morakot disaster in 2009, Central Geological Survey launched a national LiDAR mapping program dedicated to the investigation of geological hazards. I gained the knowledge of airborne LiDAR as well as natural hazards from peers of this profession. Especially, I acknowledge all of the

colleagues in ITRI worked with me in this period of time for promoting airborne LiDAR technology including Kuo-Shin Hsiao, Da-ko Chen, Wei-Chen Hsu, Hsin-Yu Hou, Tzu-Yi Liao, Chi-Chung Lau, Miao-Hsiang Peng, and Chieh-Cheng Yen.

I also must acknowledge Dr. Jiann-Yeou Rau for his invaluable discussion when he was a Ph. D student and associate specialist in Center for Space and Remote Sensing Research, National Central University, under the supervision of Prof. Dr. Liang-Chien Chen. From 2004 to 2009, with the cooperation of ITRI, Prof. Dr. Chen was in charge of research and development on building reconstruction from LIDAR Data and Aerial Imagery. The discussion with Dr. Rau includes monitoring scheme of landslides and joint efforts in developing software tools for manual interpretation of shallow landslides in addition to the application of photogrammetric means for automatic detection of landslides.

I am also indebted to Prof. Dr. Chyi-Tyi Lee for his friendship and long support. Since Prof. Lee inaugurated the first Director of Graduate Institute of Applied Geology in 1991, National Central University, I have learnt so much landslide-related knowledge from him because seismic and landslide hazard analyses are his academic interests and I have the privilege to discuss with him and his research students.

Finally, to my family, my wife Linda Feng-Chin Lin, my son Luis Yao Liu, and my daughter Sofia Shao-Wen Liu, thank you for listening and understanding when I responded to your many requests with excuses of professional matters.

TABLE OF CONTENTS

中文摘要	iii
ABSTRACT	vi
DEDICATION	x
ACKNOWLEDGEMENTS	xi
LIST OF TABLES	xvi
LIST OF FIGURES	xvii
CHAPTER 1 INTRODUCTION.....	1
1.1 Research Background and Motivation	1
1.2 Research Purposes	6
1.3 Organization of the Dissertation.....	7
CHAPTER 2 GEOMORPHOMETRY OF LANDSLIDES AND AIRBORNE LIDAR TECHNOLOGY.....	9
2.1 Significance of Geomorphometry of Landslides.....	9
2.2 Introduction to Airborne LiDAR Technology	13
2.3 Favorable Factors of using LiDAR for Landslide Investigations	17
2.4 Adverse Factors of using LiDAR for Landslide Investigations	20
CHAPTER 3 LANDSLIDE DETECTION USING AIRBORNE LIDAR DATA .25	
3.1 Detection of Shallow Landslides.....	26
3.1.1 Introduction	26
3.1.2 Method 1: Expert-based Method.....	27

3.1.3 Method 2: Method with Indices of Point Cloud Density	30
3.1.4 Method 3: Method of nDSM Slicing.....	38
3.1.5 Method 4: A Hybrid Object-oriented Method	44
3.2 Detection of Deep-seated Landslides	52
3.2.1 Introduction	52
3.2.2 Method 1: Expert-based Methods	54
3.2.3 Method 2: Texture or OOA Methods.....	57
3.2.4 Method 3: Multi-temporal Analysis	62

CHAPTER 4 LANDSLIDE MONITORING AND VOLUME CHANGE

ANALYSIS OF LANDSLIDES.....	72
4.1 Introduction	72
4.2 Methods of Landslide Volume Analysis.....	73
4.3 Study Area and Materials	81
4.4 Results and Discussion.....	83

CHAPTER 5 LANDSLIDE EXTRACTION WITH A GEOMORPHOLOGICAL

MODEL.....	89
5.1 Introduction	89
5.2 Study Area and Materials	90
5.3 The Geomorphological Model for Landslide Extraction	96
5.4 Results and Discussion.....	103
5.5 Summary of establishing the geomorphologic model.....	112

CHAPTER 6 CONCLUSIONS AND FUTURE WORKS	114
6.1 Conclusions and contributions	114
6.2 Recommendation for future study	114
REFERENCES.....	116
APPENDIX 1 ACRONYM.....	139



LIST OF TABLES

Table 2.1 Table 2.1 Types of landslides (Varnes, 1978)	10
Table 2.2 Simplified classification landslide scheme applied to Taiwan	12
Table 3.1 The criteria for the recognition of rainfall-induced landslides	28
Table 3.2 Attributes of the LiDAR data used in point density study.....	35
Table 3.3 Confusion table of OOA classification and pixel-based classification	52
Table 5.1 Tries of different combinations of thresholds for model parameters	110
Table 5.2 Model accuracy for 2008 training samples in polygons.....	110
Table 5.3 Model accuracy for 2009 training samples in polygons.....	110



LIST OF FIGURES

Figure 2.1 An idealized rotational slide showing commonly used nomenclature for labeling the parts of a landslide (Cruden and Varnes, 1996).....	10
Figure 2.2 Suggested nomenclature for landslides by IAEG Commission on Landslides (1990).....	11
Figure 2.3 Flowchart of Airborne LiDAR Survey and Applications..	15
Figure 2.4 Multiple echoes (returns) of LiDAR pulses. G denotes a point on the bare ground.....	19
Figure 2.5 Manual editing of point clouds is a must, especially for vegetated and complex terrain.....	24
Figure 2.6 Example of the resultant DEMs due to data voids and artifacts.....	24
Figure 3.1 A scheme showing the methods proposed in this study for landslide detection using LiDAR standard products.	26
Figure 3.2 Shaded-relief image of LiDAR DSM (Left) and DEM (Right) at the southern bank of Shimen Reservoir, North Taiwan..	30
Figure 3.3 Orthographic aerial photograph (Left) and DSM-shaded relief (Right) at Alishan of central Taiwan.....	30
Figure 3.4 Schematic diagram showing the geometry of airborne LiDAR scanning...	32
Figure 3.5 Selected results of four types of point density and their distribution under various searching radii with 1m grid.....	37
Figure 3.6 (A) Point cloud distribution with attribute of flight strip source ID. (B) Density map of multiple-return echoes with $r=1.414m$ and grid spacing = 1m.....	38
Figure 3.7 (A) Gray map of nDSM of the study area. (B) Distribution of the locations of points with extra-ordinary values.....	42
Figure 3.8 Gray maps of nDSM(A), DSM(B) and DEM(C).....	43
Figure 3.9 Gray-level slicing of various nDSM ranges.....	44
Figure 3.10 Flowchart of OOA data processing.....	49
Figure 3.11 The three derivatives of othophoto, DEM and DSM for data entry.....	49

Figure 3.12 Study Area and Ground Truth for OOA Test.	50
Figure 3.13 Results of the hybrid OOA method.....	51
Figure 3.14 The results generated by pixel-based SVM classification.	52
Figure 3.15 A comparison of two images: color aerial photograph (left) and shaded-relief image of airborne LiDAR DEM (right) (Lewis, 2006).....	56
Figure 3.16 Deep-seated landslides revealed in LiDAR-derived image at I-Lan.....	57
Figure 3.17 Shaded relief image of the Coringa Landslide and immediate surroundings. The primary kinematic units within the slide are earthflows E1 and E2, the area of compression U1 and the Blocky area with incorporated limestone blocks (McKean and Roering, 2004).....	59
Figure 3.18 Shaded relief image of the Salmon Falls landslides for semivariogram and fractal analyses. UB=Upper block, B=Body, T=Toe. (Glenn et al., 2006).....	60
Figure 3.19 LiDAR-derivatives of Li-Shan landslide complex, central Taiwan.....	61
Figure 3.20 The location of Hsiaolin Slide and the vicinity. The landslide boundary is draped on the 3D perspective view of aerial photograph taken after the event.....	65
Figure 3.21 Three DSMs and DEMs of Hsiaolin Slide.....	66
Figure 3.22 Topographic Features of Hsiaolin Slide and its Subdivisions.	68
Figure 3.23 (A) color coded image of V32; (B) shaded relief image of V32..	69
Figure 3.24 Cross section of Hsiaolin Slide along A-B-B' shown in top diagram of Fig. 3. $\alpha=31.7^\circ$, $\beta=22.3^\circ$, $\gamma=8.6^\circ$	70
Figure 3.25 A close-up of the depletion area of Hsiaolin Slide. Remnants of unconsolidated materials still existed on the bare surface. The dash-line is the isoplethic line with -20 m. The area covers 48.68 hectares..	70
Figure 4.1 A simple difference of 2010 DEM and 2005 DEM and the DoD result where the legend shows the value of the difference in meters.....	75
Figure 4.2 Different thresholds applied to the DoD results: (A) not applied; (B) a threshold of -3 m..	76
Figure 4.3 Each individual landslide (B) can be extracted from the overall landslide	

map (A) generated by DoD method.	77
Figure 4.4 Landslide volume estimation using three landslide dimensions.....	78
Figure 4.5 Landslide volume estimation using areas of cross sections of fixed-interval.	80
Figure 4.6 Landslide volume estimation using a grid of landslide depths.....	80
Figure 4.7 The study area of Namashia District of Kaohsiung City.	82
Figure 4.8 LiDAR Data used in Namashia study area.	83
Figure 4.9 Hsiaolin Slide and its 7 subdivisions. The landslide is represented by an ellipse for the dimensions of width and length. Black lines are isopleths of -5 m and red lines are isopleths of +4m. Subdivision A is the major landslide body.	84
Figure 4.10 Interpretation of a 2D landslide map on basis of orthophoto and DoD-shaded images.....	87
Figure 4.11 extraction of individual landslides are made one by one from the whole landslide map.....	88
Figure 4.12 Empirical formula of landslide area A (m^2) and volume V (m^3) of the data points of landslides in the study area, $V=kA^a$..	88
Figure 5.1 SPOT image taken on 2009/08/24 after Typhoon Morakot. The 8-digit numbers are the map numbers of national 1/5000 map series.	91
Figure 5.2 A regional geological map near the Hsiaolin village (Song et al., 2000).. ..	92
Figure 5.3 Satellite images of the study area from 2005 to 2009. Bright grey features on the images are mostly landslide scars. Landslide occurrence increasingly increases in this period of time, as shown in Figure 5.8.	93
Figure 5.4 DEM and DSM images before Typhoon Morakot.....	95
Figure 5.5 3D perspective views of Hsiaolin Village before and after Typhoon Morakot. Hsiaolin Landslide has a volume of ~25 million cubic meters with a maximum depth of 85 m on top area and a maximum length of 3396 m from top to the other side of Chisan River. The landslide completely destroyed the village.....	95

Figure 5.6 DEM and DSM obtained after Typhoon Morakot. As compared to those of Fig. 4, dramatic landform change can be found in river valley as well as mountain slopes, especially the example of Hsiaolin Landslide.	96
Figure 5.7 Flowchart of the geomorphometric model.....	98
Figure 5.8 Landslide distribution between 2005 and 2009. Landslides on images are high-lighted with yellow polylines. New landslides are in red polylines when comparing images taken in 2005 and 2008 (E) and those in 2008 and 2009, respectively.....	105
Figure 5.9 The distributions of major LiDAR-derived geomorphometric parameters selected for landslide recognition in this study. The coordinates of the maps are (209810 , 2566339) and (217609 , 2557916) for the lower right and upper left, respectively.....	106
Figure 5.10 Frequency distribution of geomorphologic parameters of landslides in 2005.	108
Figure 5.11 Frequency distribution of geomorphologic parameters of landslides in 2009.....	108
Figure 5.12 Landslide prediction with geomorphometric model: (A) Prediction of 2008 landslide susceptibility based on 2005 landslides in vector segments. (B) Prediction of 2009 landslide susceptibility based on 2005 landslides in vector segments.	112

Chapter 1 Introduction

1.1 Research background and motivation

Motivated by the tremendous loss and damages of Taiwan due to natural disasters caused by the vulnerable physiographic environment (NFA, 2012) and the newly availability of airborne LiDAR technology due to the launch of a national airborne LiDAR mapping program (Liu and Fei, 2011) and advances in the researches on the use of LiDAR in landslide investigations (Jaboyedoff et al., 2010&2012), this study is devoted to explore the applicability of airborne LiDAR data for investigation of landslides in Taiwan.

Nearly three-quarters of the territory of Taiwan, and 95% of its population, are exposed to frequent natural hazards (Dilley et al., 2005). In the aftermath of Typhoon Morakot, which dramatically affected southern Taiwan on August 8, 2009, and August 9, 2009, and caused the worst flooding in a century, authorities realized that the country is lacking detailed, accurate, and current elevation data and aerial imagery covering the entire territory of 36 000 km². To address this problem, a national mapping program, spanning 2010 to 2015, was launched to capture an entire territory of the country with airborne LiDAR (Light Detecting And Ranging) and digital imagery (Liu and Fei 2011). A LiDAR DEM (Digital Elevation Model) and DSM (Digital Surface Model) and color orthophotos represent a core part of this national spatial data infrastructure.

Taiwan is located on the active collision zone between the Eurasian plate and the Philippine Sea plate. Mountains have a high slope and high relief, and rock formations are highly fractured and fragile. These physiographic settings are unfavorable to slope stabilities. Taiwan is also located on the path of typhoons in northwest Pacific area. Torrential rainfall during the typhoon season often triggers geological hazards. Landslides are one of the most important primary disasters.

In Taiwan, a typhoon can trigger hundreds, even thousands, of shallow landslides in mountainous areas (Lin and Jeng, 2000; Cheng et al., 2005; Lin et al., 2006). These landslides can deliver large amounts of sediment into local reservoirs, reducing their water storage capacity (Dadson et al., 2004; Mikos et al., 2006). In addition, the turbidity of the water in the reservoirs has a negative effect on the sustainable operation of water supply reservoirs. The assessment and inventory of landslides is essential for effective watershed management and sustainable development. However, because of the steep terrain in Taiwan's mountainous watersheds, most landslides are unreachable. The detailed topographic mapping required for emergency mitigation measures cannot be completed within a short period using conventional on-site surveying. Therefore, improving the efficiency and accuracy of landslide monitoring and mapping using remote sensing techniques has become an important research issue (Liu, 1987; Raju and Saibaba, 1999; Rau et al., 2007; Borghuis et al., 2007; Herva et al., 2003).

In planning optimal measures of disaster mitigation, researchers often use remote sensing images and digital elevation models to map disaster features and to predict disaster susceptibility. During or immediately after a disaster event, ground survey or photogrammetry, in addition to remote sensing images, can be used to obtain detailed topography data of the subjected area. Because of its ability to obtain high-density point clouds and direct geo-referencing, LiDAR can be used to obtain a more accurate and detailed topographic survey. LiDAR generates accurate 3D coordinates of discrete measurements. Subsequently, DEM and DSM can be produced with high efficiency. In tropical and sub-tropical zones of Taiwan, most of the terrains are covered by dense forestry. Ground surface would be normally predicted by the surface of canopy in photogrammetry if the ground points cannot be seen from two different perspectives of a stereo-pair. One of the most important advantages of airborne LiDAR compared with conventional photogrammetry is that photogrammetry requires two different lines of sight to both see the same points on the ground from two different perspectives, but LiDAR only needs a single laser pulse to penetrate through the trees to measure the ground beneath. This means that LiDAR will have far fewer areas where the terrain is obscured by trees that block the lines of sight. The images of bare ground before and after the event are thus derived from LiDAR surveys to understand changes in the landscape and their possible consequences. The geomorphometric features become good tools for landslide detection, and are adopted in this study.

The general feature of a rainfall-induced landslide on aerial photograph is a fresh landslide scar with an elongated shape located on a relatively steep slope. Landslides can occur in any kind of geology, as there are some weathered overburdens on steep slopes. In aerial photographs, landslide features include a bright tone, bare surface, and the other features shown in Table 1. Manual interpretation uses both 2D and 3D features of the landslides for recognition: 2D features include tone, location, and shape, and 3D features include location, direction, slope, and shadow effects. A sound consideration of the automation of landslide recognition should consider all these aspects.

Geomorphometry is a major concern in manual interpretation. Geomorphometry, also known as geomorphological analysis, terrain morphometry, terrain analysis, and land surface analysis (Hengl and Reuter, 2009), is the science of quantitative land surface analysis. The purpose of geomorphometry is to extract surface parameters and objects using input from digital terrain models. Pike (1988) used a dozen groups of parameters as terrain descriptors by manually digitized digital terrain models. Pike used the resulting "geometric signature or topographic signature" to categorize terrain characteristics, and suggested the degree of landslide danger. Topographic signature of life and their processes are deemed to be strongly influenced by biota (Dietrich and Perron, 2006). Guth (2001&2003) used terrain fabric as measures of a point property of the digital terrain models and the underlying topographic surface. This technique is also called topographic fingerprinting

(Densmore and Hovius, 2000), and determines the location of a landslide on the slope. State-of-the-art technology such as high resolution satellite images, digital aerial photography, and airborne LiDAR has opened a new era in the automation of landslide recognition, especially the possibility of applying geomorphometrics. The extraction of land surface parameters is becoming increasingly attractive for both stochastic and process-based modeling, as it makes use of all the levels of detailed digital terrain models. Topographic-based analyses can be used to objectively delineate landslide features, generate mechanical inferences about landslide behavior, and evaluate recent landslide activity (Glenn et al., 2006; Mckean and Roering, 2004). Surface roughness derived from LiDAR DTM allows the objective measurement of landslide topography. Eigenvalues of surface normals are an effective parameter for differentiating shallow landslides and debris flows (Woodcock, 1977). Expert knowledge of the geomorphometric properties of landslides may be required to establish an automatic interpretation method. High resolution and high accuracy LiDAR DEM and DSM and orthophotos are now basic constituents of NSDI in Taiwan (Liu and Fei, 2011). Therefore, it is high time to further apply geomorphometry in active landslide study (Liu et al., 2009).

Airborne LiDAR make it possible to map and evaluate landslides in a survey type of regional level (typically at scales ranging from 1:10,000 down to 1:4,000,000 or even smaller), whereas the accuracy can be as good as or community level or site-specific level (typically vary from 1:1,000 to 1:10,000).

1.2 Research purposes

The major future challenges in landslide investigations as reviewed by van Westen et al. (2005) includes: (1) the use of very detailed topographic data; (2) the generation of event-based landslide inventory maps; (3) the use of event-based maps in spatial-temporal probabilistic modeling; and (4) the use of land use and climatic change scenarios in deterministic modeling. This viewpoint was also supported by a recent review by Jaboyedoff et al. (2010&2012) on the use of LiDAR in landslide investigations. The later stressed on airborne LiDAR for imaging relief by high-resolution digital elevation models or 3D models and gave a general review of different applications of LiDAR for landslide, rockfall and debris-flow. This review shows that LiDAR-derived data can be used to investigate any type of landslides including both shallow and deep-seated ones. Nevertheless, LiDAR data are not yet a common tool for landslides investigations though this technique has opened new domains of applications that still have to be developed.

Applications of LiDAR in landslide investigations can be classified as: (1) Detection and characterization of landslides which include the recognition of landslides and their subsequent application in susceptibility analysis; (2) Monitoring of displacement or volume change of landslide bodies; (3) Modeling for prediction of landslides. Therefore, the purposes of this research are to develop methods for understanding all these 3 aspects: (1) Landslide

recognition for both shallow and deep-seated landslides with expert-based and semi-automatic approaches with cases from northern and southern Taiwan; (2) Landslide volume change with multi-temporal LiDAR data in southern Taiwan; and (3) geomorphometric modeling for the automatic extraction of shallow landslides with selected geomorphometric features such as including slope, curvature, OHM (object height model), OHM roughness, and topographic wetness index which are derived from multi-temporal LiDAR data acquired in 2005 and 2009 in southern Taiwan.

1.3 Organization of the dissertation

The remainder of this dissertation is organized as follows. In Chapter 2, summaries of classification schemes of landslides and morphologic features of landslides are introduced with subsequent review of favorable and adverse factors of applying LiDAR data for landslide investigation, thus to perceive the prospects and limitations of the new technology. In Chapter 3, methods and experiments for landslide detection for both shallow and deep-seated landslides are presented including expert-based interpretation and semi-automated methods. In Chapter 4, methods and experiments for the volume estimation of regional sedimentation and individual landslides with multi-temporal LiDAR data are presented and an empirical power law is derived to model the relation between A (m^2) and volume V (m^3) of landslides. In Chapter 5, methods and experiments for establishing a geomorphological model for extracting landslides using

multi-temporal LiDAR data are presented. Final concluding remarks and suggestions for future researches are presented in Chapter 6. Appendix 1 gives a list of acronym for the abbreviations used in this dissertation.



Chapter 2 Geomorphometry of Landslides and Airborne

LiDAR Technology

This chapter is served as basics to the applications of airborne LiDAR data for landslide investigations. At first, summaries of classification schemes of landslides and standard morphologic features of landslides are introduced. Secondly, a review of favorable and adverse factors of applying LiDAR data for landslide investigation is made, thus to perceive the prospects and limitations of the new technology.

2.1 Significance of Geomorphometry of Landslides

Landslide refers to any mass of earth material displaced by gravity. The various types of landslides can be differentiated by the kinds of material involved and the mode of movement. The most popular classification system based on these parameters is shown in Table 2.1 (Varnes, 1978). Geomorphometry is measurement of forms (size and shape) of geological phenomena or features. Morphological features of landslides are properties related to the external structure of landslides. Airborne LiDAR survey acquires digital elevation models in a resolution as high as one meter which may reveal detailed landslide features. The dimensions and geometry of a landslide have been described by Varnes (1978) and subsequently modified by Cruden and Varnes (1996) using the cutaway drawing in Figure 2.1. Subsequently, the International Association

of Engineering Geologists (IAEG) created a Commission on Landslides that has produced the section and definitions of a landslides for landslide features and dimensions (Figure 2.2) (IAEG Commission on Landslide, 1990). The feature of different parts of a landslide may thus be recognized from airborne LiDAR data.

Table 2.1 Types of landslides (Varnes, 1978).

TYPE OF MOVEMENT		TYPE OF MATERIAL		
		BEDROCK	ENGINEERING SOILS	
			Predominantly coarse	Predominantly fine
FALLS		Rock fall	Debris fall	Earth fall
TOPPLES		Rock topple	Debris topple	Earth topple
SLIDES	ROTATIONAL	Rock slide	Debris slide	Earth slide
	TRANSLATIONAL			
LATERAL SPREADS		Rock spread	Debris spread	Earth spread
FLOW		Rock flow	Debris flow	Earth flow
		(deep creep)	(soil creep)	
COMPLEX (Combinations of two or more principal types of movement)				

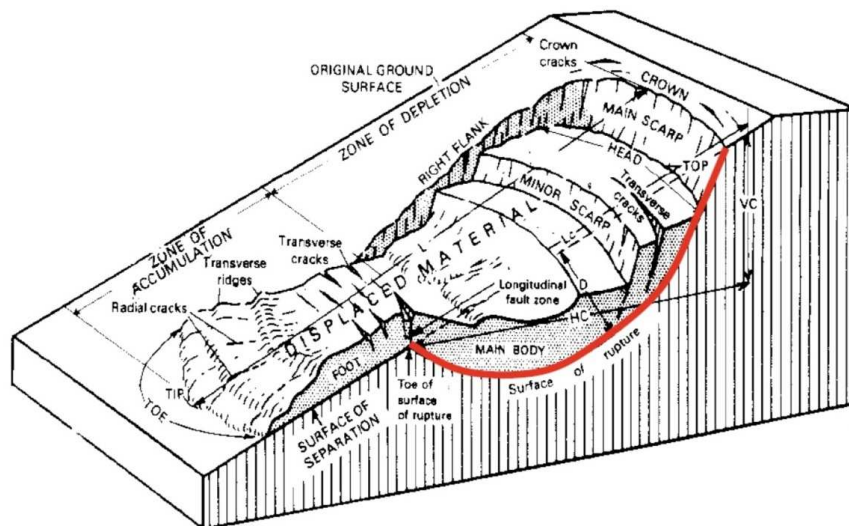
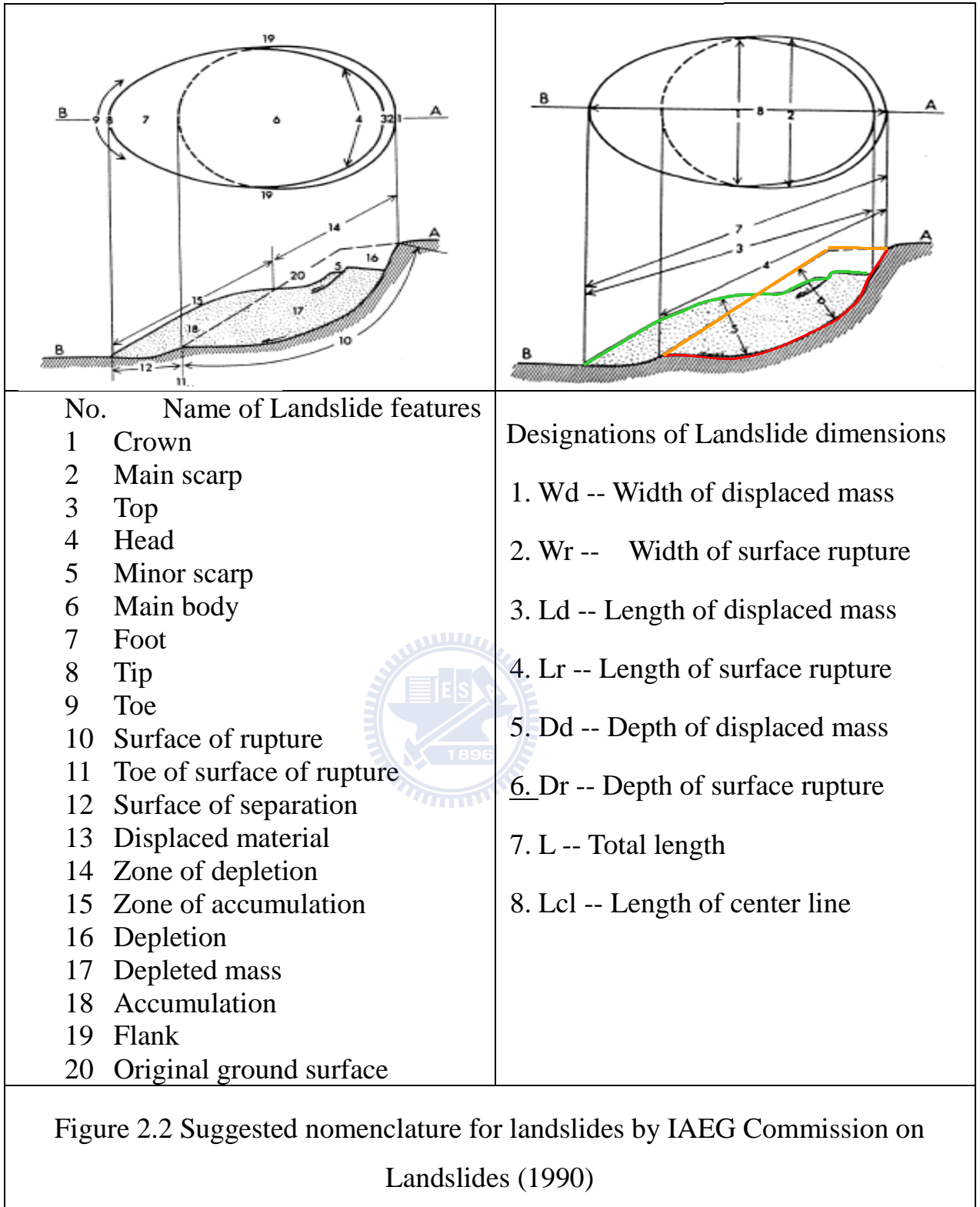


Figure 2.1 An idealized rotational slide showing commonly used nomenclature for labeling the parts of a landslide (Cruden and Varnes, 1996)



For practical applications in the physiographic environments of Taiwan, the classification scheme of landslides developed by Varnes (1978) is simplified

into five major categories, namely, rock falls, shallow-seated landslides, deep-seated landslides, dip-slope and wedge slides, and debris flows, as shown in Table 2.2. Thus, types of landslides can be differentiated by their physical appearance, which is especially useful for practical applications with remotely sensed images.

Table 2.2 Simplified classification landslide scheme applied to Taiwan

Type of Movements		Type of Materials		
		Bed rock	Engineering Soils	
			Debris	Soils
Falls	Rock falls	Shallow-seated slide		
Topples				
Slide	Translational			Dip-slope and wedge slide
	Rotational			
Flows	(not applicable)	Debris flow	(not applicable)	

In this dissertation, for the detection of landslide features only shallow and deep-seated landslides are differentiated. Shallow landslide refers to the landslide in which the sliding surface is located within the soil mantle or weathered bedrock (typically to a depth from few decimeters to some meters). Shallow landslides usually include debris slides, debris flow, and failures of road cut-slopes. Deep-seated landslide refers to the landslide in which the sliding surface is mostly deeply located below the maximum rooting depth of trees (typically to depths greater than ten meters). Deep-seated landslides

usually involve deep regolith, weathered rock, and/or bedrock and include large slope failure associated with translational, rotational, or complex movement. These typically move slowly, only several meters per year, but occasionally move faster. They tend to be larger than shallow landslides and form along a plane of weakness such as a fault or bedding plane.

As pointed out by Pike (1988&2000), geological phenomena such as landslides may be characterized by sets of diagnostic measurements of geo-features which is known as geometric signature. Therefore, morphological features of landslides of the properties related to the external structure of landslides can be used for landslide detection, for multi-temporal change analysis, and landslide modeling. Spatial measures of landslide include both 2D planimetric attributes (X, Y) and 3D continuous elevation or relief attributes (X, Y, Z). Obviously, airborne LiDAR survey with standard products of point clouds and grids of digital elevation models and digital surface models should have high potentials for obtaining the spatial measures of landslides.

2.2 Introduction to Airborne LiDAR Technology - standard products

Airborne LiDAR is mainly used for landslide investigation to create accurate and precise high resolution digital elevation models (DEM) and digital surface models (DSM) in raster grids. Basic products of airborne LiDAR usually include all points, ground points, DEM, and DSM (MOI, 2006). The former two are vectors of discrete points and the later two are interpolated raster grids of the

discrete points of the former two. Nevertheless, new specifications and recommendations may require products such as simultaneous digital aerial photographs, full waveforms, and so on (Heidemann, 2012).

Figure 2.3 is a flowchart showing the general process of an airborne LiDAR survey and applications. Generally, five phases of tasks are implemented for an airborne LiDAR survey, including: (1) The planning step; (2) Flights and pre-processing – obtaining point clouds in local projected coordinate system, such as Taiwan Geodetic Datum 1997 (TWD97), Taiwan Vertical Datum 2001 (TWVD 2001); (3) Classification step – The extraction of points hitting the bare earth from all point clouds for the production of LiDAR DEM; (4) Quality validation step - for assuring the conformance of quality and quantity requirements of the results to the selected guidelines or specifications, such as MOI (2006) or USGS Lidar base specification (Heidemann, 2012); and (5) The output step – Interpolation of discrete points is made to obtain grids of specified resolution and specified map-sheet extent, such as 1 m grid of national 5k map-sheets in Taiwan. Thus, DEMs and DSMs with ellipsoid height are created by interpolation of the discrete ground points. In Taiwan, DEMs and DSMs with orthometric heights are then prepared by applying a reduction of geoid undulation model published by the Ministry of The Interior, namely Taiwan Vertical Datum 2001 (TWVD2001). Subsequently, applications can be made with or without former or ancillary data. And, most importantly domain knowledge of the applications are critical and required.

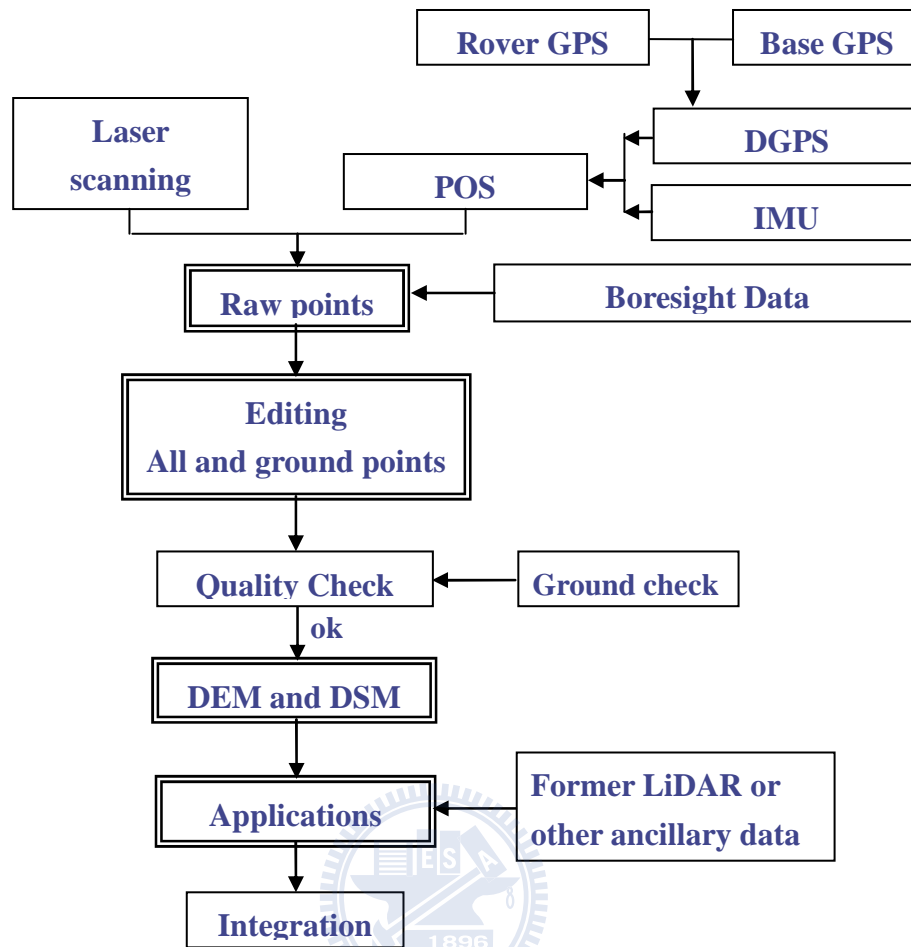


Figure 2.3 Flowchart of Airborne LiDAR Survey and Applications

A common practice of using rectangular grid for interpolation from vector format of discrete points to raster format is due to its ease of use and availability of interpolation tools. TIN (Triangulated Irregular Network) or other raster format can also be applied for geological applications when point clouds are available.

Usually, vertical accuracy will be specified in the LiDAR survey. The vertical accuracy of DEM is evaluated by a direct comparison of LiDAR DEM and ground survey for the analyzed study areas. According to the accuracy

specification of LiDAR DTM by the Ministry of the Interior, Taiwan (MOI, 2006), the accuracy of elevation should satisfy the following formula based on some environment conditions and the production of DEM:

$$\sigma = a + b + ct \quad (2.1)$$

where σ is the tolerable error, a is fundamental accuracy based on the product level of DEM, b is the topography-adjustment factor, c is the vegetation-adjustment factor, and t is the mean height of trees. The DEM used in this study is derived from point cloud data with manual editing and strip adjustment so the fundamental accuracy a is equal to 0.3 m and the topography-adjustment factor b is 0 in an area with a slope smaller than 5° , 0.2 m in an area with a slope 5° - 15° , 0.5 m in an area with a slope 15° - 30° , and 1.0 m in an area with a slope greater than 30° . The vegetation-adjustment factor c is 0 for bare land, 0.2 for grass land, 0.3 for forest, and 0.5 for dense forest. According to the accuracy specification, the maximum tolerable error of DEM in the dense forest area will be 8.3 m with a slope greater than 30° if the mean height of trees is 14 m. In geological applications, most of the time expert interventions are required for interpretation. Therefore, such a stunning tolerance of absolute accuracy would usually not cause problems in applications though cares and awareness always have to be taken.

The relative error is also evaluated with overlap data and absolute error is evaluated by a comparison with ground control points. According to the LiDAR

guide (MOI, 2006), the residuals between strips in this study are smaller than 10 cm. A cross flight is designed in every 30 km perpendicular to major flight lines for checking discrepancies between flight strips. Five land-types and transactions for ground survey are also selected for validating the accuracy achieved in this phase. Ground data are collected by GPS and Total Stations. The 5 designated land-cover types include (1) bare land, (2) low vegetation, (3) sparsely-vegetated forest, (4) dense forest, and (5) building-up area. At least 30 measurements are collected for each of the cover types. In addition, 50 check points are collected along a profile of 20 km in length crossing the flight strips. As an example, the RMSE (root mean square error) accuracies on cover types of bare land, low vegetation, sparse forest and building-up areas are better than 0.16m for the datasets used in this study for Namashia case (see paragraph 4.3 in Chapter 4). The average error for transactions in the study area is 0.131 m. And, the RMSE is around 0.25 m for dense forest. These standardized procedures assure the requirements of geodetic and vertical survey datum, as well as the quality of the datasets.

2.3 Favorable Factors of using LiDAR for Landslide Investigations

The favorable factors or unique features that make airborne LiDAR data so useful for landslide investigations are summarized in this paragraph. These unique features include (1) multiple echoes and/or full waveform; (2) high density and high resolution; (3) high accuracy, in terms of large area survey; (4)

direct geo-referencing.

The capability of multiple echoes for one laser pulse make it possible to "see through" the forest. As shown in Fig.2.4, when a pulse is traveling down it might hit an object before reaches the ground, and thus, an echo or return can be expected from the point where the beam hit the object. The beam will travel further downward and may hit another objects except completely blocked by an object or the ground. Currently, LiDAR sensors are able to record up to 7 echoes per pulse and every echo can give a coordinate of the interaction location. Whereas, 4 echoes are recorded for most of LiDAR sensors, such as the prevailing sensor producers Leica and Optech. Points for both of types A and B are created by single echo, also known as only echo. For type A, the points hit the bare ground. For type B, the points hit on object above the ground. Points of type C~F are created by multiple echoes and the points may hit several objects before reach the bare ground. Types C and D include two echoes, namely first echo and last echo. Types E and F include three echoes, namely first echo, intermediate echo and last echo. This feature of multiple echoes is used in assisting automatic and manual editing of ground points.

The state-of-the-art pulse rate of airborne LiDAR can be as high as 500 KHz (Roth and Thompson, 2008; Roth, 2010 & 2011). Average point density of airborne LiDAR survey can be as high as 20 points per square meter. The most common specification is with an average point density of 1 or 2 points per square meter, which has been practiced in Taiwan. Therefore, DEM/DSM grid is

usually with 1 m or 2m. Because of the nature of airborne survey with a nominal flight speed of circa 100 knots, efficiency of large area survey with high resolution and high accuracy can be achieved. In addition, the technology of direct geo-referencing of airborne LiDAR makes it possible to have accurate coordinates of each individual points as well as the derived grid. As compared to the traditional stereoscopic study of aerial photo-interpretation, the direct geo-referencing is an important favorable factor. Thus, it is possible to obtain results of interpreted landslides with high position accuracy.

All these unique features of airborne LiDAR make it possible (1) to observe 3D features of landslides; (2) to observe landslides under forest cover; (3) to detect micro-morphological features of deep-seated landslides; and (4) to observe minor offset of lineaments of geological structure.

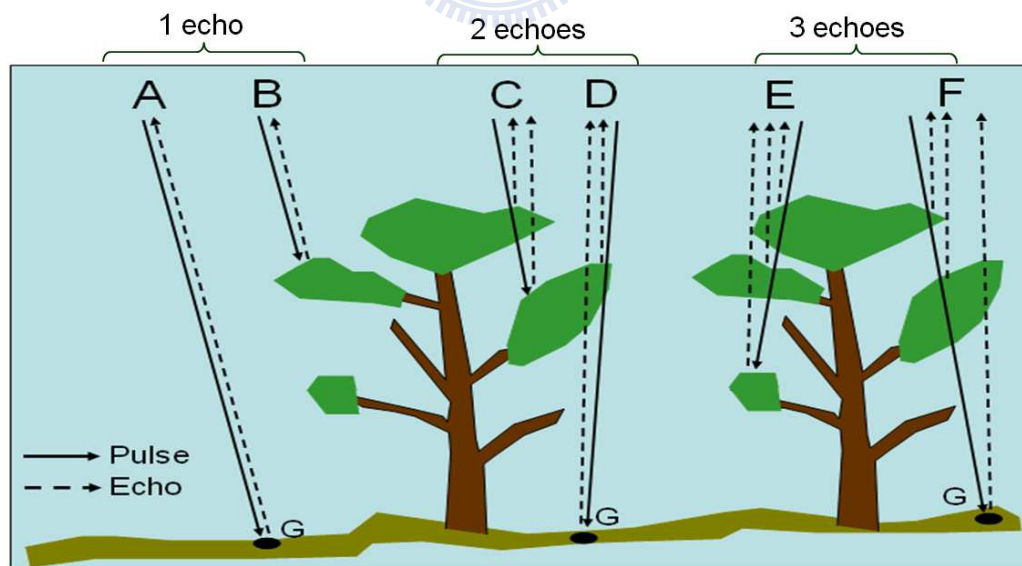


Figure 2.4 Multiple echoes (returns) of LiDAR pulses. G denotes a point on the bare ground.

2.4 Adverse Factors of using LiDAR for Landslide Investigations

This paragraph is to discuss some pitfalls which may mislead the applications of airborne LiDAR data for landslide investigations. Cares and awareness have to be taken for these pitfalls though researches can also be conducted to find out methods for suppressing the uncertainties caused by these pitfalls. Trade-offs of resource allocations for the compensation between ideal products and de facto products can be perceived in this discussion (Liu et al., 2010).

These adverse factors are inherent in every stage of LiDAR data production: (1) In general handling of data, there are problems of edge-matching between map-sheets and interpolation methods; (2) In project preparation and acquisition stage, there are problems of setting up a common datum for all surveys, and acquisition with an optimal point density for all points and ground points; (3) In acquisition and editing stage, the problem of artifacts (commission error) and voids (omission error) (Liu et al., 2010; Hopkinson, 2006).

Due to the large volume of LiDAR point clouds, interpolation for DEM/DSM grids is usually carried out on basis of map-sheets which may extend only around 2.5 km by 2.5 km as the instance of 1/5000 Taiwan National Map-sheet Series. For a large study area which is composed of multiple map-sheets, discontinuities will exist between map-sheets. Measures are required to handle this problem though it is not specified in LiDAR guidelines (MOI, 2006). In addition, different interpolation algorithm may generate

different results of DEM/DSM form identical discrete point cloud. Users must be aware of this problem when using DEM/DSM datasets, especially when comparing two different datasets.

A national common datum is required to keep all spatial data under the same frame for analysis and comparison. Nevertheless, in practice, this may not be the case. Some dedicated LiDAR survey may apply their own datum for some reasons. As an example, the datum adopted by Taiwan LiDAR Survey project is TWD97_CGS and the ground control points of this datum are with different coordinates in 2009 and 2011. Other source of datum problem may be due to that the DEM/DSM datasets are generated by different sensors or by different sensors such as InSAR or photogrammetry.

Density of ground points is an important index of DEM quality. However, high density of ground points may not be easily achieved for areas of high relief or dense forest (Hsu et al., 2012; Liu and Fei, 2011). In general, low penetration rate (i.e. the ratio between number of ground points and that of all points) may be due to factors such as (a) nature of vegetation cover; (2) complexity of topography; (3) ground surface conditions such as wetness, grass, or bushes; (4) flight parameters which may be limited by constraints of schedule and budgets; and others. Lack of ground points in certain areas will cause data voids, and thus cause problems or misunderstanding in applications. In addition, high overall point density may produce high density of ground points, whereas it cannot be assured due to the un-controllable factors aforementioned.

Figure 2.5 is an example of point cloud editing for filtering non-ground points and retaining ground points. Manual editing of point clouds is a must, especially for vegetated and complex terrain. Even though after manual editing, the resultant DEM is still prone to errors in the viewpoints of users in geology. Why? Usually, there are around 4 millions of ground points in a map-sheet of 2.5 km by 2.5 km. If the acceptability criterion is set to 1 percent for either commission error and omission error, the total erroneous points will be as many as 80,000 points in one map-sheets. Points of commission error result in artifacts in LiDAR image where the height of trees are used in the interpolation of DEM. Points of omission error take place very often in dense forest area and thus result in flat mountain tops and rough terrains in sloping area. Figure 2.6 shows examples of voids (A) due to lacking ground points on top of mountains and artifacts (B) due to imperfect filtering of trees on sloping areas. Figure 2.6(C) shows that it is possible to improve this type of flaws by good practice of manual editing.

Data voids mostly are resulted from gaps of flight coverage and occlusion by topography, clouds, and trees. in the experience of Taiwan National LiDAR Mapping, Hsu et al. (2012) indicated that there are 8 types of gaps, namely (a) water bodies; (b) cloud covers; (c) steep slopes; (d) volley bottoms; (e) mountain ridges and tops; (f) lateral winds on high mountain tops; (g) sudden change of topography at the ends of a flight-line; and (h) possible mirror reflection or absorption of laser energy on certain high mountain slopes. For the area covered

by water bodies, there are no echoes due to water absorption of LiDAR IR wavelength in 1064 nm. Cloud covers are the most serious problem in the high mountains. Steep slopes in this area are almost as high as 90 degrees. Valley bottoms and mountain ridges or tops are out of range of the setting pulse rates and thus caused no returns of signals recorded. The lateral winds on high mountain tops causes the plane drifts, deviate from the scheduled flight path, and thus cause gaps of point clouds. Sudden change of topography at the ends of a flight-line due to safety reasons and thus causes the width of flight-strip becomes smaller on ridges. An unusual phenomena with no LiDAR echoes is the possible mirror reflection or moisture absorption on certain high mountain slopes where in reality are landslide terrains with medium slopes.

Due to the unique features of airborne LiDAR data, the number of publications discussing the use of LIDAR in landslide studies has grown considerably during the last decade (Derron and Jaboyedoff, 2010). Nevertheless, some of the adverse factors discussed above are inherent to the datasets. Awareness and cares have to be taken into consideration in the applications. Some of the adverse factors that concerning with the settings of flight parameters might be amended with strict specifications, and thus requiring more cost in data acquisition. A trade-off between quality and cost is obvious in this case.

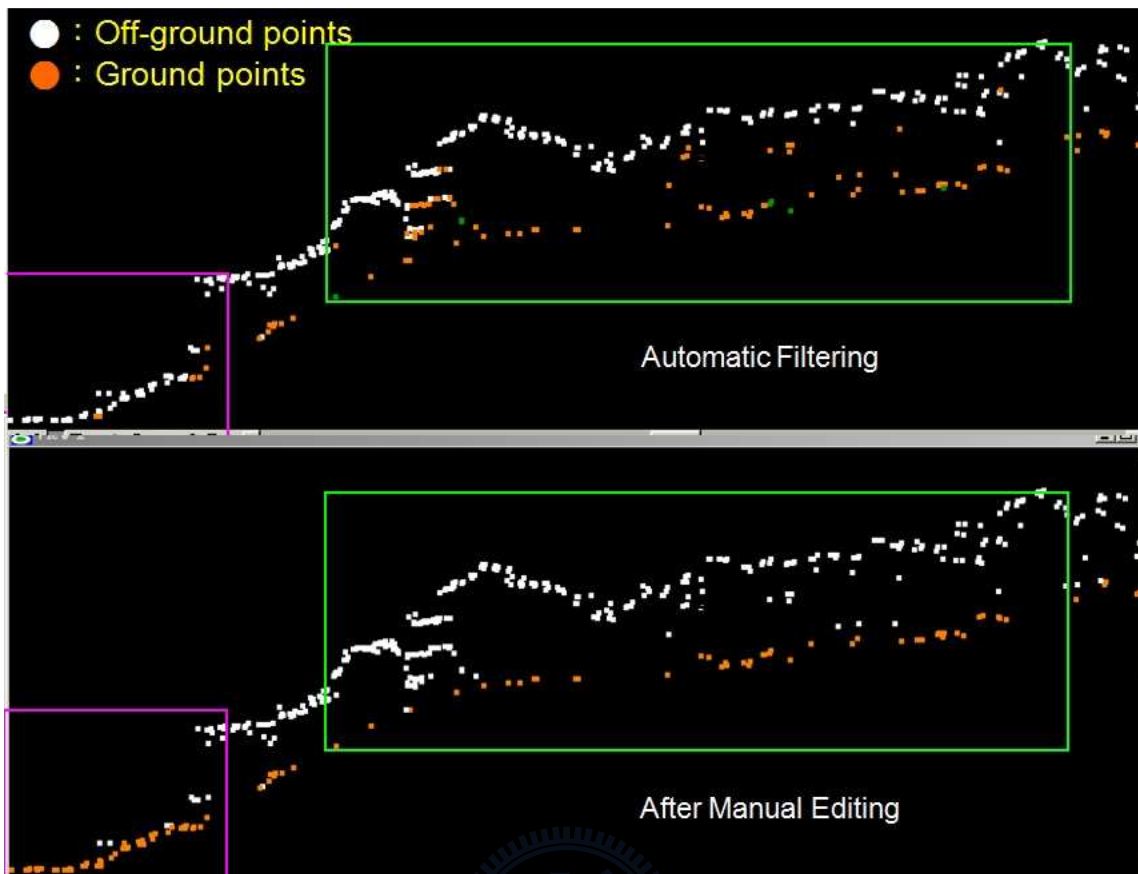


Figure 2.5 Manual editing of point clouds is a must, especially for vegetated and complex terrain.

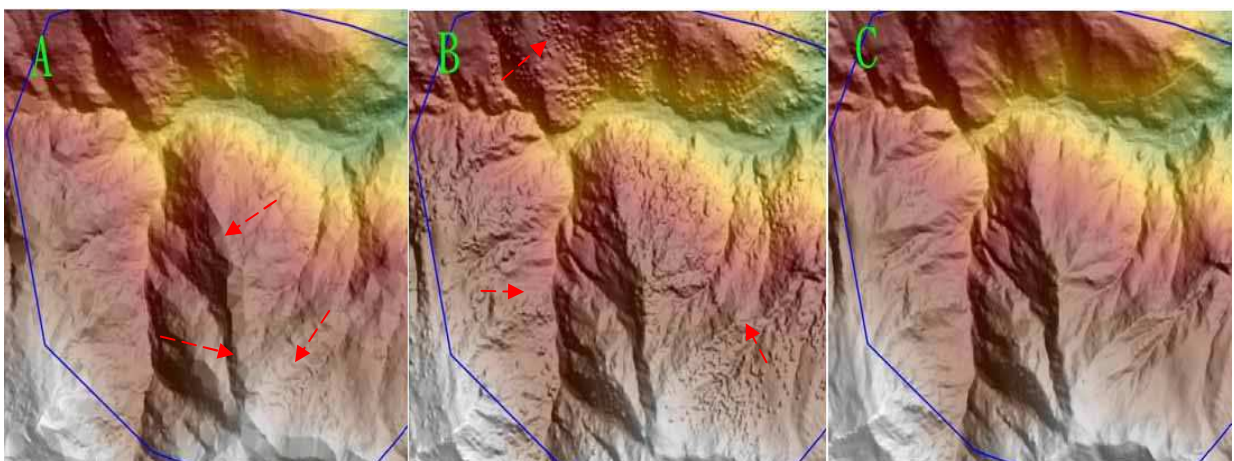


Figure 2.6 Example of the resultant DEMs due to data voids and artifacts

Chapter 3 Landslide Detection Using Airborne LiDAR Data

In this chapter, methods and experiments for landslide detection for both shallow and deep-seated landslides are presented including expert-based interpretation and automated methods.

In the experiment of shallow landslide detection (Figure 3.1), four methods are proposed and tested in this research, namely (1) Expert-based Method - a test of conventional approach of manual photo-interpretation; (2) Method of Indices of Point Density - using LiDAR point clouds; (3) Method of nDSM Slicing - using DSM and DEM; and (4) A hybrid OOA Method - using all standard products of LiDAR survey in an object-oriented classifier.

In the experiment of deep-seated landslide detection, three methods are raised and two of them are tested in this research, namely (1) Expert-based method - a test of conventional approach of manual photo-interpretation with the new possibility of micro-morphology analysis using LiDAR-derived shaded-relief images. This is the main application of LiDAR data for the study of deep-seated landslides; (2) Method of Texture-related or OOA Method - though this is not tested in this study whereas a brief review is made for demonstrating the significance; (3) Method of Multi-temporal Analysis - the major extension of expert-method using multiple times of LiDAR data for

perceiving the activeness of deep-seated landslides.

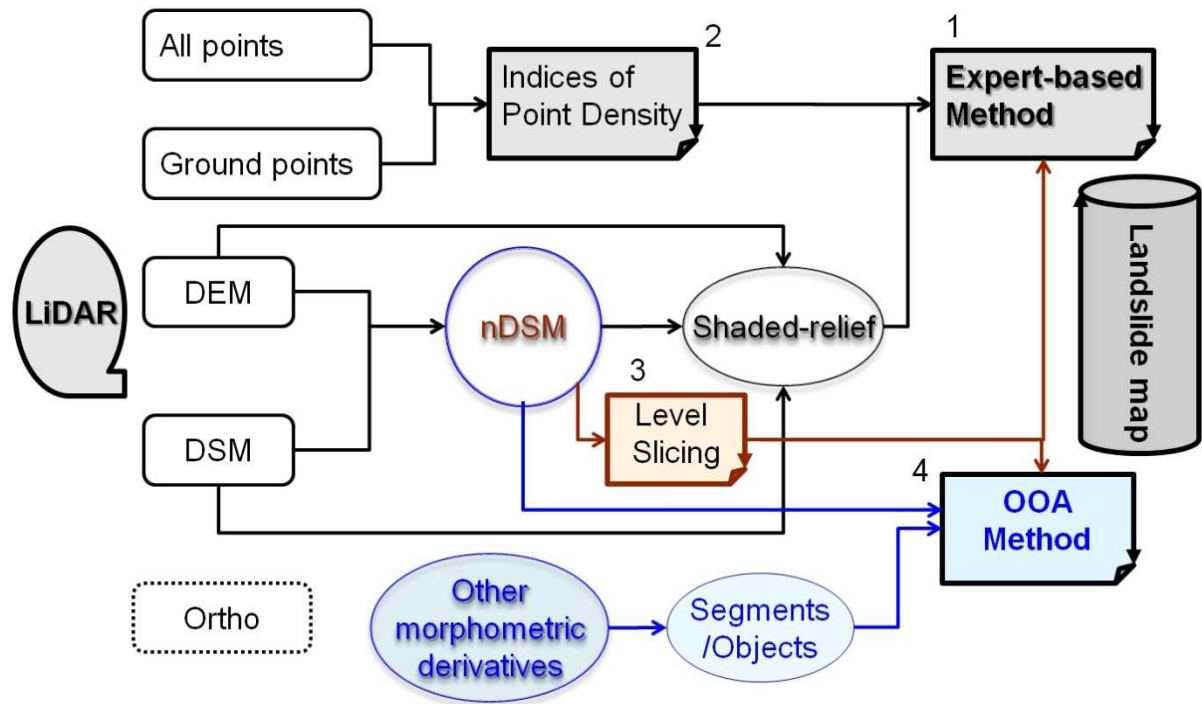


Figure 3.1 A scheme showing the methods proposed in this study for landslide detection using LiDAR standard products

3.1 Detection of Shallow Landslides

3.1.1 Introduction

An effective method for landslide detection has to be able to give a correct recognition of landslide body and to give an accurate delineation of landslide. In other words, area size and spatial distribution of landslides should be correctly enumerated. In this research, four methods are proposed, tested, and discussed. Only samples are demonstrated for expert-based method. Each of the other three methods uses the same datasets and discussed with four parts including introduction of the method, methodology, materials, and results and discussion.

3.1.2 Method 1: Expert-based Method

Rainfall-induced landslides are in majority shallow-seated in the high relief terrains of Taiwan. Techniques of stereoscopic airphoto interpretation have been adopted for landslide inventory in Taiwan since 1973 when an aerial survey team was established under Agricultural Council of the government (Liu, 1987). Though it is labor intensive, it is believed to be reliable. The core spirit of this approach is the synergy of human perception to include both 2D and 3D features of the target and its environment. In the traditional photo-interpretation procedures, the most critical technique is to use stereoscope for perceiving the sense of 3D features and an expert should be acquainted with interpretation key for the study area (Chang and Liu, 2004; Van Den Eeckhaut, et al., 2005). Shaded-relief images of DEM and DSM can be good substitutes for aerial photographs for expert interpretation.

Table 3.1 shows the criteria used for the recognition of landslides on aerial photographs which are also applicable for using LiDAR-derived shaded-relief images. The general feature of a rainfall-induced landslide is characterized by the fresh landslide scars in elongated shape and located in a relatively steep slope. It takes place in any kind of geology so long as there are some weathered overburdens. Features on aerial photographs include the bright tone, the bare surface, and the features shown in Table 3.1. Manual interpretation uses both 2D and 3D features of the landslides for recognition. The 2D features include tone,

location, and shape. The 3D features include location, direction, slope, and shadow effects.

Table 3.1 The criteria for the recognition of rainfall-induced landslides

Feature	Description	Discrimination rule
Tone	Light, grey light	Brightness value > Threshold
Location	Near ridges, cut-off slopes, road-sides	Trigger events and buffer zone of the feature
Shape	Spoon-shaped, elongated-oval, dendritic, rectangular, triangular	Location-specific and topography-specific
Direction	The drop direction of the landslide is the gravitational vector on the ground surface.	Roughly perpendicular to the streams and topography-specific
Slope	Depend on types of landslides. E.G. Shallow-seated landslides > 45%; Deep-seated landslides ~40%; Debris flows ~10-20%.	Slope > Threshold
Shadow	Depend on whether the landslides are in shadow-side or sunny-side	Solar azimuth in related to slope aspect

Figure 3.2 shows two shallow landslides on shaded-relief images derived from LiDAR DSM and DEM, respectively. Obviously, due to the contrast of surface smoothness the landslide can be observed better on DSM-shaded image rather than on DEM-shaded image. Another important issue is the occlusion of landslide due to high relief. As shown in Figure 3.3, occlusion of landslide features takes place everywhere in high mountain areas due to the nature of central projection of aerial photography. Shadow effect may become an annoyance or disturbance rather than an advantage in the high relief mountain areas.

LiDAR-derived images can be treated as true-ortho images because they are derived from point clouds of high accuracy.

The advantages in using LiDAR-derived images for landslide detection for expert method can be summarized as follows:

(1) Landslide features maybe overlooked or omitted due to shadow, occlusion and vegetation cover using aerial photo-interpretation approach. These adverse problems can be minimized by using DEM-shaded and DSM-shaded images as surrogates to aerial photographs.

(2) The objects above ground surface have been removed for DEM whereas those are remained for DSM. Therefore, DSM-shaded images exhibit better contrast of landslides with surroundings than that of DEM-shaded images. Therefore, for image interpretation of shallow landslides, DSM-shaded images are better than DEM-shaded images.

(3) Various angles of illumination can be visualized and tested for gaining better perception of landslides. As a comparison, the sun angle is fixed for aerial photography. Shadow effects which are used to be important factor for visual interpretation can be optimized using LiDAR-derived images.

(4) LiDAR-derived images are true-ortho images with which relief displacement and distortions due to object heights are removed. Therefore, the result of landslide map obtained by interpreting LiDAR-derived images possesses accurate coordinates on the map.

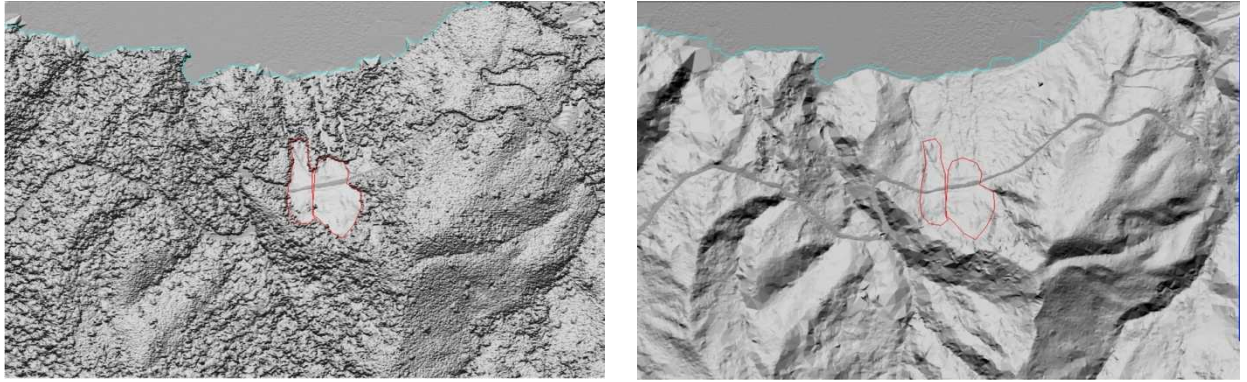


Figure 3.2 Shaded-relief image of LiDAR DSM (Left) and DEM (Right) at the southern bank of Shimen Reservoir, North Taiwan

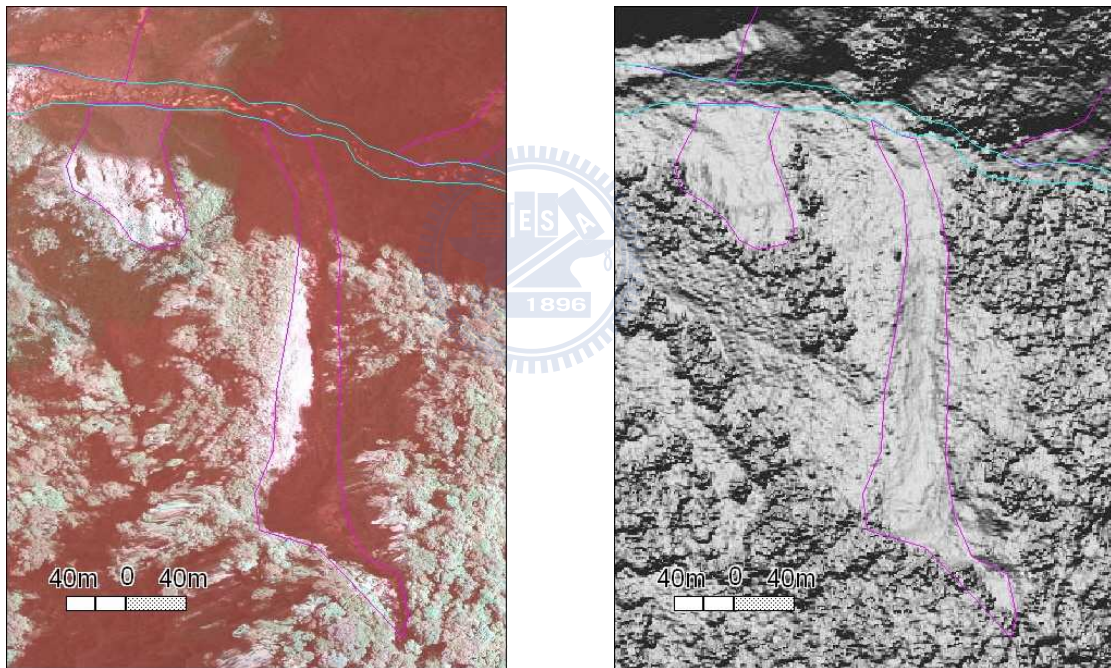


Figure 3.3 Orthographic aerial photograph (Left) and DSM-shaded relief (Right) at Alishan of central Taiwan.

3.1.3 Method 2: Method with indices of point cloud density

(A) Introduction

Basic products of airborne LiDAR include all points, ground points, digital

elevation model (DEM), and digital surface model (DSM). The former two are vectors of discrete points and the later two are interpolated raster grids of the discrete points of the former two. The DEM and DSM grids are commonly used for applications whereas point clouds are rarely used. LiDAR discrete points are worthy of a further study due to the fruitful information adhered with the attributes of individual points. Point density has been used as an important indicator of DEM/DSM quality (Shih and Huang, 2006; Liu et al., 2007; Puetz et al., 2009; Raber, 2003). An understanding of the forest closure and crown density can be obtained by inspection of the point-density distribution of point clouds (Dubayah and Blair, 2000; Means et al., 2000; Naesset, 2002). Therefore, point density derived from specific properties of point clouds can be used to explore the possibility of extracting landslide information from point clouds. Visual interpretation of shaded-relief image derived from DEM is usually adopted by geologists whereas other LiDAR products have not been commonly applied. In this paper, possible derived indices from point clouds are discussed first and then experiments of selected indices are made to find out the most descriptive ones for landslide detection.

(B) Deriving a point density map

The attributes of individual points of LiDAR point clouds are recorded in a LAS format. The format contains binary data consisting of a header block, variable length records, and point data (ASPRS, 2008&2009). Each point data record

includes the XYZ coordinates, intensity, return number, number of returns, scan direction, and classification of the point. These attributes of point cloud are closely related to the geometry of laser scanning configuration and thus relevant to the point density of unit ground area. The spatial distribution of point density implies the properties of the land surface. Exact coordinates of each point are determined by the relationship between the location of laser head, scanning angle, location of object and shape of the ground surface, as schematically shown in Figure 3.4. In other words, factors for point density include all these flight design parameters and the effects of ground conditions: (1) pulse rate; (2) look angle; (3) flight height; (4) plane attitude (roll, yaw, pitch); (5) flight speed; (6) strip overlap; (7) terrain relief; and (8) above-ground objects.

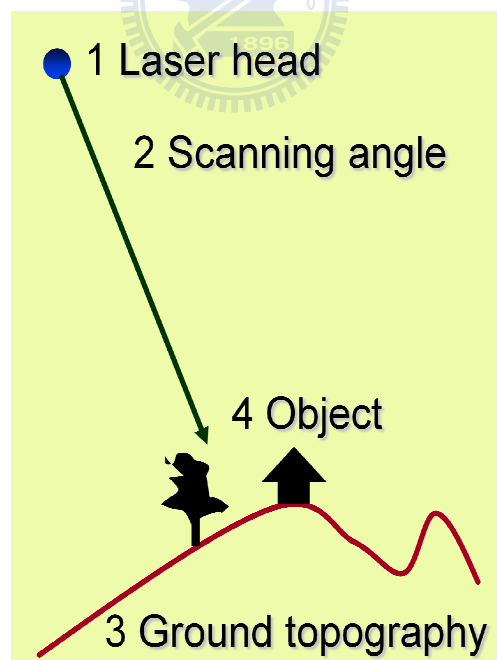


Figure 3.4 Schematic diagram showing the geometry of airborne LiDAR scanning

For discriminating landslide and non-landslide lands, the types of point clouds for point density enumeration can be categorized as follows: (1) all points, (2) ground points, (3) single-echoes points or only-echoes points, (4) multiple-echoes points, i.e. (first + intermediate + last) returns, (5) first-return points, (6) intermediate-return points, and (7) last-return points. Secondary indices can also be created by combining two or more types of point clouds, for example, penetration rate can be derived by the ratio of ground and all points denoting the fraction of points hitting the bare ground. For exploring the capability of point clouds for the detection of landslides, four types of point density with five searching radii are used in this study, including point density type of all points, ground points, only-echoes points, and multiple-echoes points. Comparison of them will be made to search for most descriptive ones for landslides.

Point density can be measured by various approaches (Shih and Huang, 2006). In this study, point density is measured by subdividing the surveyed area into grid cells, then computing the unit density of the number of points in a circle with certain searching radius centered at the cell center. A software application is implemented in this study to cater for the output grid size, searching radius, and type of points. This method is comparable to that by Crosby (2007). In this dedicated software application, the function of reading Terrascan PTC file for point class definition is also implemented so that various type of point density

can be designated. Point density distribution of ground points is affected by the criteria and procedures of both automated and manual editing process. Nevertheless, point density except that of ground points is mainly decided by flight operation parameters including pulse rate, look angle, flight height, aircraft attitude, flight speed, strip overlap, terrain relief, and above-ground objects. Because the average ground points of the selected study area is 0.75 pts/m², 1 m is selected for grid spacing. To cater for the effects of the uniformity of point distribution, ground surface undulation and land-cover types, five searching radii are used, i.e. 0.707m, 1.414m, 3.0m, 5.0m, and 10 m.

(C) Testing site and materials



The study area is located in I-Lan County of northeastern Taiwan, on the track of the Typhoon Kalmaegi attacked Taiwan on July 16th~18th, 2008, about nine month after Typhoon Krosa on October 4th, 2007 in this area. The dataset for the experiment was taken on 4th November, 2008 after Typhoon Kalmaegi. In general, the accuracy of bare grounds checked in the field is about 0.15 m. An area covering 2 km by 2 km is selected for the experiment. The overall point density of the study area is 2.75 points/m² with ground point density of 0.75 points/m² (Table 3.2).

Table 3.2 Attributes of the LiDAR data used in point density study

Type of points	All points	Ground points	Only-echoes points	Multiple-echoes points
Total number of points	12,142,434	3,320,615	5,789,148	6,353,286
Average point density (points/m ²)	2.75	0.75	1.31	1.44
Minimum height (m)	574.08	574.08	574.08	577.72
Maximum height (m)	1290.43	1279.65	1290.43	1290.29

(D) Results and discussions

After examination of the test results of the four types of points versus five searching radii, findings are as follows:

- (1) Striping noise of point density map is obviously affected by flight speed and strip source as shown in Figure 3.5.
- (2) Point density map of multiple-echoes point gives better contrast between landslide and non-landslide areas than any maps derived from other three types of point density, as shown in Fig. 3.6 (B).
- (3) For output of 1m grid spacing, point density map with a searching radius of 1.414 m shows best result among all radii including 0.707, 1.414, 3, 5, and 10 m. This result is subjected to the density of all points and ground points. A larger radius cannot give better enhancement of landslides.
- (4) Although the overall point density of only-echoes points of the whole study area is similar to that of multiple-echoes points as shown in Table 3.2, a conspicuous contrast of landslide area is observed on the density map of

multiple-echoes points other than that of only-echoes points. This is due to a high concentration of multiple-echoes points in forested land and most of bare grounds are covered by only-echoes points.

(5) Landslide feature is conspicuous in some part of the density map of ground points whereas it is vague in other parts. This is a consequence of the factors of penetration rate in different part of the area and the filtering process of non-ground points with both automated algorithm and manual editing. However, on the map of all points overlaid by ground points, landslides features can be enhanced for visualization. Nevertheless, commission errors of landslide interpretation can be serious on this map, especially in those bare lands which are not landslides. These errors might be eliminated by slope gradient of ground surface in a later step.



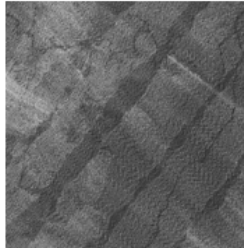
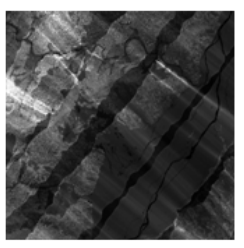
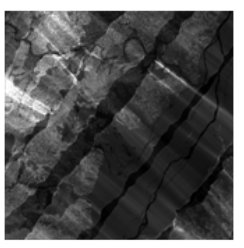
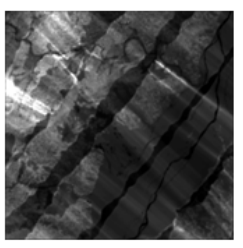
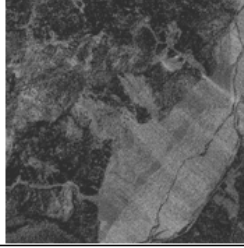
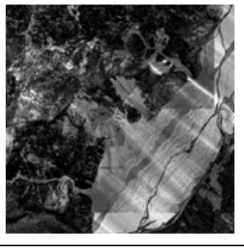
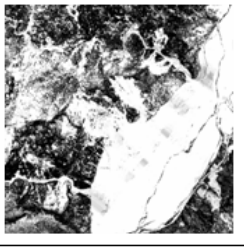
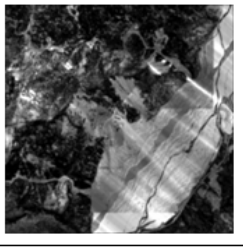
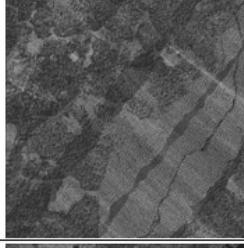
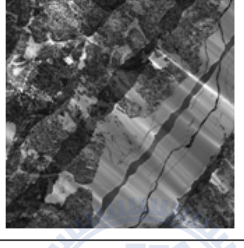
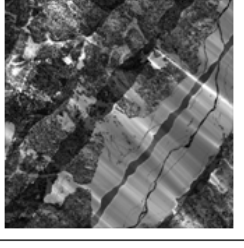
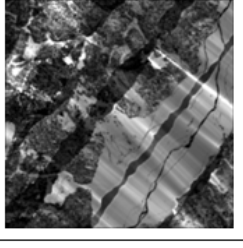
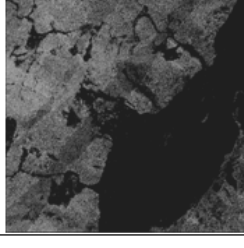
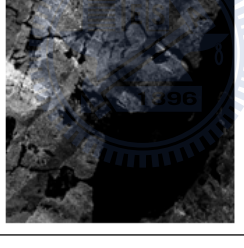
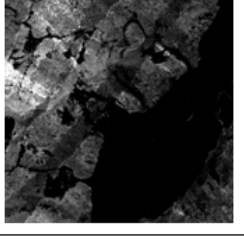
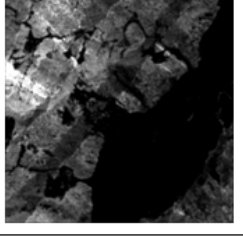
	Original point clouds	Density With R=1.414	Density With R=3.0	Density With R=10.0
All points				
Ground points				
Only returns				
Multiple returns				

Figure 3.5 Selected results of four types of point density and their distribution under various searching radii with 1m grid.

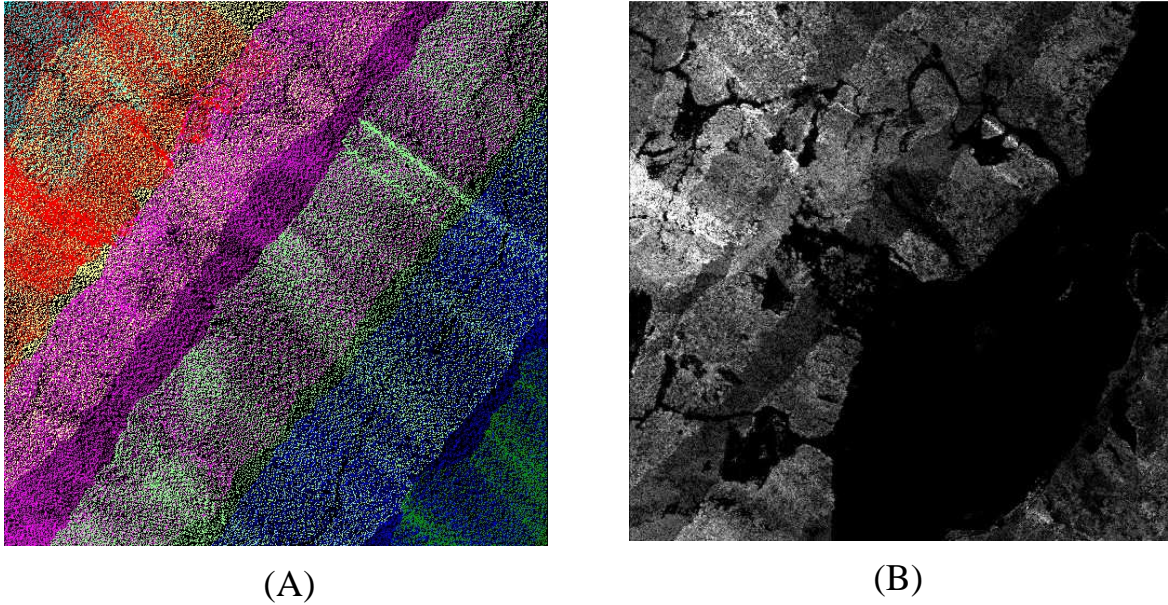


Figure 3.6 (A) Point cloud distribution with attribute of flight strip source ID.
 (B) Density map of multiple-return echoes with $r=1.414\text{m}$, grid spacing = 1m.

3.1.4 Method 3: Method of nDSM slicing

(A) Introduction

The resulted standard products of an airborne LiDAR survey thus include all points, ground points, Digital Surface Model (abbreviated as DSM) and Digital Elevation Model (abbreviated as DEM). The former two items are point vectors whereas the later two are gridded results interpolated from the former two. DEM is the one prevailingly applied. It is pointed out that the cloud of discrete points is full of latent information which can be further explored (Liu et al., 2010). LiDAR DEM has been used for landslide interpretation (Schulz, 2007; Van Den Eeckhaut et al., 2007) whereas DSM is not applied as often. Both of DSM and DEM are standard products of a LiDAR survey. A necessity to compare the

effect of them is obvious.

Because both DSM and DEM are in raster format which is compatible with remote sensing images, it is convenient to apply image processing techniques in extracting useful thematic information. The difference of DSM and DEM is known as normalized DSM, denoted as nDSM. Due to the bareness of shallow landslides, the pixel value of landslide area is theoretically near zero. This feature can never be obtained in a conventional DEM. Therefore, the properties of nDSM obtained by image subtraction will be further explored with gray-level slicing methods to find out the best enhanced thematic maps from DSM and DEM for the detection of landslides.



(B) Method

Image enhancement techniques are used for the enhancement of landslide features on DSM and DEM images. The purpose of the enhancement processing is to make the resultant images more suitable for landslide interpretation or for subsequent automated pattern recognition of landslides. Image processing can be applied in either spatial domain or frequency domain (Gonzalez and Woods, 2002). Approaches in spatial domain are to treat image pixels directly: $g(x,y) = T[f(x,y)]$, where the T function can be applied to single pixels such as contrast stretching, thresholding, or binary Image, or it can be applied globally to the whole image or a subset of the image. Approaches in frequency domain are making use of convolution theorem: $g(x,y) = h(x,y) * f(x,y)$; $G(u,v) =$

$H(u,v)F(u,v)$. $h(x,y)$ and $H(u,v)$ are the masks in spatial domain and frequency domain, respectively. $g(x,y)$ is to be solved and obtained by a Fourier Transform of $G(u,v)$. The pixel processing in spatial domain usually include (1) gray value transformation, (2) enhancement with statistical characteristics, (3) image subtraction, and (4) image averaging. In this study, image subtraction of DSM and DEM is applied first to obtain nDSM, which latently enclose all objects or features above the bare ground. Subsequently, gray-level slicing method is applied to the nDSM image to find out an optimal range of gray values to present landslide distribution.

(C) Testing site and materials

A test area is selected in I-Lan County of eastern Taiwan, the same as the one for the test of Method with indices of point cloud density in Paragraph 3.1.3 (C).

The attributes of the data sets is shown in Table 3.2.

(D) Results and discussion

Figure 3.7(A) is a gray map of nDSM obtained by subtraction of DSM and DEM of the study area. The range of the values in the resultant image is from -29.60 m to +116.68 m. The nDSM image is obviously prone of outliers or extra-ordinary values such as negative values and values larger than the height of highest possible trees. Therefore, nDSM is in no way representing all objects above bare ground and cares have to be taken for object extraction. The

extra-ordinary values are due to both definition of ground points (and thus DEM) and operation procedures of interpolation from discrete points to continuous surfaces. The distribution of these extra-ordinary points is shown in Figure 3.7(B). It is observed that the extra-ordinary points are mostly located in areas of rugged terrain and high fluctuation of relief change.

To resolve the noises of extra-ordinary values in nDSM, it is necessary to either correct the errors or reset the range of the pixel values to a designated range with specific lower bound and upper bound. Gray-level slicing method is thus applied to find out the visual effect of different settings of gray-level ranges.

Gray-level slicing is a simple and straight forward method of image enhancement. If there is a specific range of pixel values on nDSM images favorable for landslide features in natural vegetated-slopes, it will be discriminated by simple slicing method.

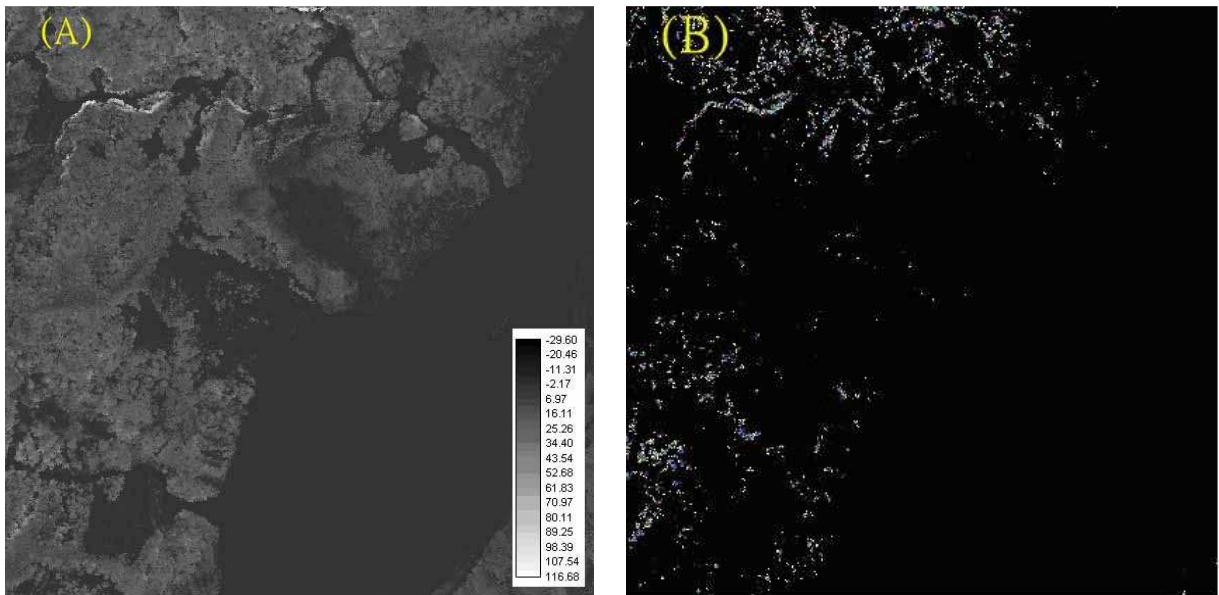


Figure 3.7 (A) Gray map of nDSM of the study area. (B) Distribution of the locations of points with extra-ordinary values.

Figure 3.8 is a blow-up of a small part of the study area, including gray maps of nDSM, DSM and DEM of identical portion of the image. The higher the digital numbers the brighter the image. In landslide area, the tone is dark due to its extreme low pixel values. On the contrary, it is bright in forested areas due to the higher pixel values of tree heights. Because pixel values of a DSM is composed of both ground height and tree height, the contrast between the areas of landslide and non-landslide is less obvious. The contrast is even less obvious for a DEM which gives only the ground height. Therefore, for visual interpretation of landslides, nDSM can be better than DSM and DEM.

Theoretically, omission error prevails if the range between the lower and upper bounds of the slices is too small. On the contrary, commission error

prevails if the range of slices is too large. Because the value of a landslide pixel on nDSM should be zero or a small number due to its physical bareness and possible sensor uncertainty, the lower bound is designated as zero and the upper bound will depend on the result of experiment in this study, tuning from +1 m upward till +20 m.

It can be observed from the results of different slicing ranges in Figure 3.9 that (1) the shape of landslides in dark tone can be conspicuously depicted in the slice of 0~1 m; (2) the shape of landslides are even obvious when the upper range becomes larger up to 10 m whereas the best is the range of 0~5 m; and (3) too many pixels of commission error are included and thus the boundary of the shape of landslides become vague in the slice of 0~20 m.

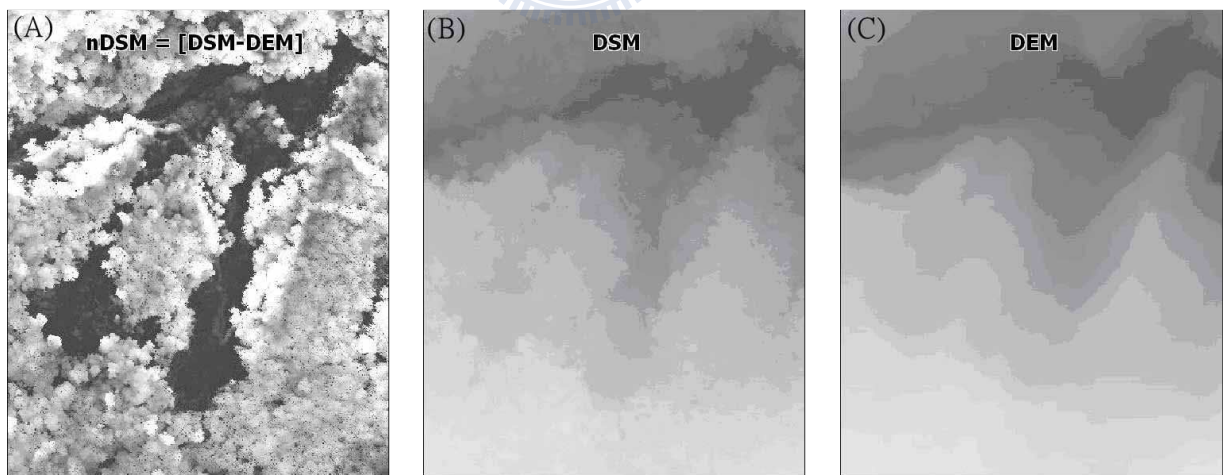


Figure 3.8 Gray maps of nDSM(A), DSM(B) and DEM(C)

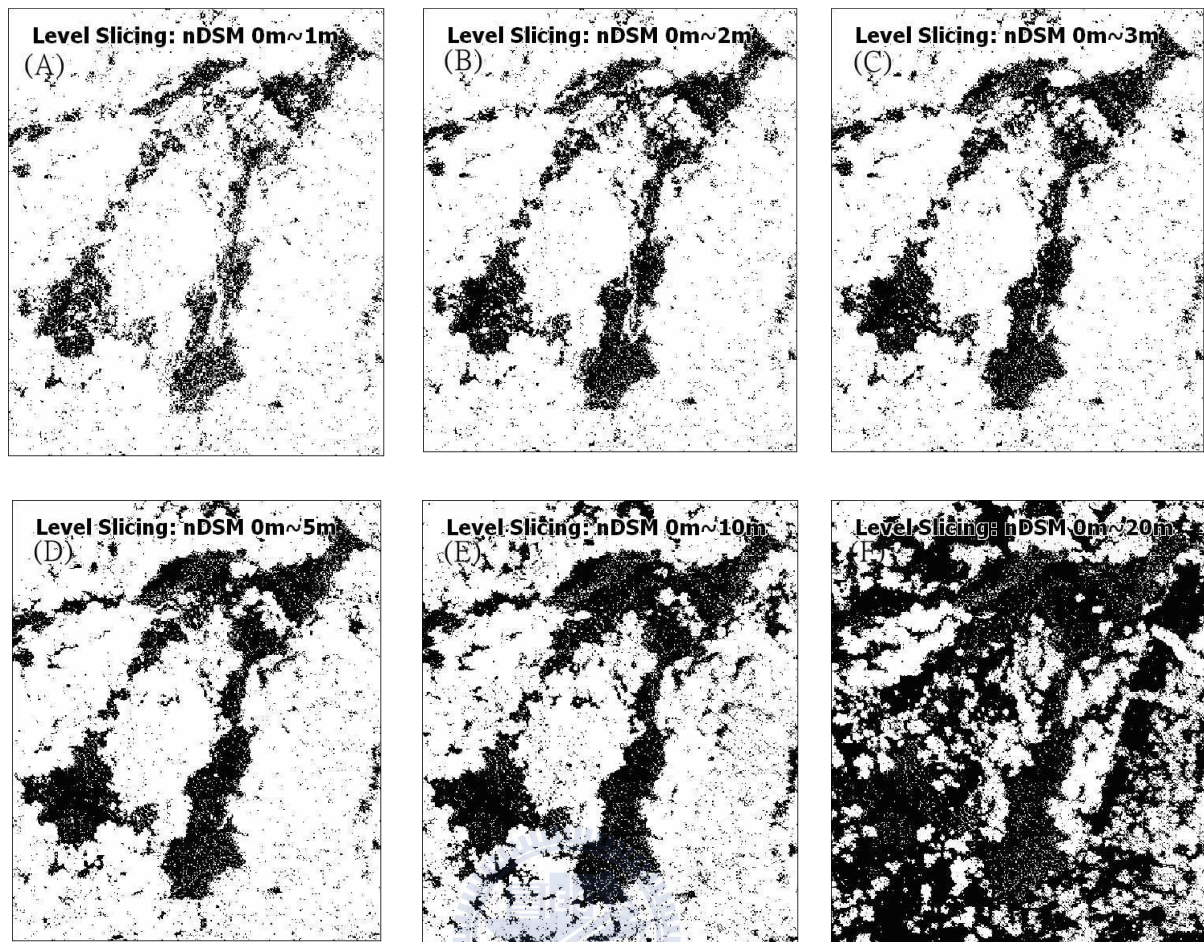


Figure 3.9 Gray-level slicing of various nDSM ranges

3.1.5 Method 4: A Hybrid Object-oriented Method

(A) Introduction

Most of the conventional automatic classification methods for landslide detection are mainly based on spectral features of remotely-sensed images other than topographic features. Because the spectral features of buildings and roads are similar to those of landslides, therefore serious mis-interpretation took place. Moreover, limitations are due to the spatial and spectral resolutions of the images. More than 50% of the rainfall-induced landslides in Taiwan are less than 50.0 m in length (Liu et al., 2012). Landslides of this scale are not readily

identifiable using images of a pixel-size larger than 10.0 m. By pixel-wise classification, landslides can occupy only individual or just a few pixels without forming an outer shape of landslides (Liu et al., 2009). Moreover, commission and omission errors of pixel-based classification can further complicate the situation. The pixel-based methods are then required to be replaced with approaches based on objects or segments (Kerle and Martha, 2010). Therefore, The main objective of this research is to combine both of an unsupervised of region-based image segmentation and a supervised classification method with SVM classifier using standard products from airborne LiDAR survey, as shown in the scheme of landslide detection in Figure 3.1.

(B) Method

Basic task of segmentation algorithms is the merge of image elements based on homogeneity parameters or on the differentiation to neighboring regions, respectively. Thus, segmentation methods follow the two strongly correlated principles of neighborhood and similarity of pixel values. The region-based approaches start in image space where the available elements either pixels or already existing regions are tested for similarity against other elements. Concerning the definition of the initial segmentation the procedures of region growing (i.e. bottom-up, i.e. starting with a seed pixel) and region splitting (i.e. top-down, i.e. starting with the entire scene) are distinguished. One disadvantage of the splitting method is that it tends to be over-segmented because a splitting always produces a fixed number of sub-regions (normally: 4)

although two or three of them might actually be homogeneous with respect to each other. As a consequence, one can apply an integration of the various methods. Thus, it leads to the split-and-merge algorithm that after a split process. If neighboring regions are similar, they should be remerged again (Chang et al., 2010).

To strengthen the automation of segmentation, clustering is adopted for region-based segmentation. The ISOCLUST is an iterative self-organizing unsupervised classifier based on a concept similar to ISODATA routine of Ball and Hall (1965) and cluster routines such as the H-means and K-means procedures (Jain and Dubes, 1988). Object-oriented analysis (OOA) is inherently more suitable, as it can address the phenomena under study such as landslides in this case, as that they are “objects”, not “pixels” that have spectral, spatial and contextual characteristics. Thus in this study, the unsupervised classification method ISODATA are applied to the nDSM image to find out an optimal range of data values to present landslide distribution (Research System, Inc., 2006).

After the segmentation, a supervised classification of the segments with SVM classifier is applied to obtain landslide class.

SVM (Support Vector Machine) is a relatively new classifier and is based on strong foundations from the broad area of statistical learning theory. Since its inception in early 90s, it has found applications in a wide range of pattern recognition problems, image classification, financial time series prediction, face

detection, biomedical signal analysis, medical diagnostics, and data mining (Witten & Frank, 2000; Hwang and Chiang, 2010; Burges, 1998; Chapelle et al., 1999). Under the basic assumption of the SVM approach, the training sample is expressed as $\{(x_1, y_1), (x_2, y_2), \dots, (x_n, y_n)\}$ where $x_i \in R^d$ represents an input mode, $y_i \in \{\pm 1\}$. The optimal decision-making formula is as follows:

$$\mathbf{w}^T x_i + b = 0 \quad (3.1)$$

The weighing vectors \mathbf{w} and b is deemed satisfactory once converged.

$$y_i(\mathbf{w}^T x_i + b) \geq 1 - \varepsilon_i \quad (3.2)$$

The value ε_i is a loose variable existing in a linear, undividable condition.

It describes the degree of module deviation under the ideal linear circumstances.

The goal of the SVM is to identify a decision support phase where the average error of the training samples is minimized. The optimization equation is

therefore derived as follows:

$$\varphi(\mathbf{w}, \varepsilon) = \frac{1}{2} \mathbf{w}^T \mathbf{w} + c \sum_{i=1}^N \varepsilon_i \quad (3.3)$$

Where C is a positive parameter assigned by the end user. It serves as a penalty for the correctness of the SVM. The C value is used to leverage the probable mis-interpretation percentage and the complexity of the algorithm. A converged optimization equation can be derived adopting the Lagrange Multiplication Method:

$$Q(\alpha) = \sum_{i=1}^N \alpha_i - \frac{1}{2} \sum_{i=1}^N \sum_{j=1}^N \alpha_i \alpha_j y_i y_j K(x_i, x_j) \quad (3.4)$$

Where $\{\alpha_i\}_{i=1}^N$ is the Lagrange multiplier while Eq. (4) fulfilling the following criteria.

$$\sum_{i=1}^N \alpha_i y_i = 0, \quad 0 \leq \alpha_i \leq C, \quad i = 1, 2, 3, \dots, N \quad (3.5)$$

$K(x_i, x_j)$ is a core function. There are four types of core functions included in the Mercer Theorem:

1. Linear : $K(x_i, x_j) = \mathbf{x}_i^T \mathbf{x}_j$ (3.6)

2. Polynomial: $K(x_i, x_j) = (\gamma \mathbf{x}_i^T \mathbf{x}_j + r)^d, \gamma > 0^d$ (3.7)

3. radial basis function (RBF): $K(x_i, x_j) = \exp(-\gamma \|x_i - x_j\|^2), \gamma > 0$ (3.8)

4. Sigmoid: $K(x_i, x_j) = \tanh(\gamma \mathbf{x}_i^T \mathbf{x}_j + r), \gamma > 0$ (3.9)

Here, γ , r , and d are kernel parameters (Burges, 1998).

The data flow is shown in Figure 3.10 where the feature space for landslide classification includes only the standard LiDAR survey products, namely ortho image, DEM and DSM. Especially, the derivatives of greenness, slope and nDSM are used for input for the segmentation (Figures 3.11). Accuracy validation will be made against the results obtained by visual interpretation using all available images derived from the same datasets (Figure 3.12). In addition, a pixel-based classification with the same datasets is also carried out for comparison.

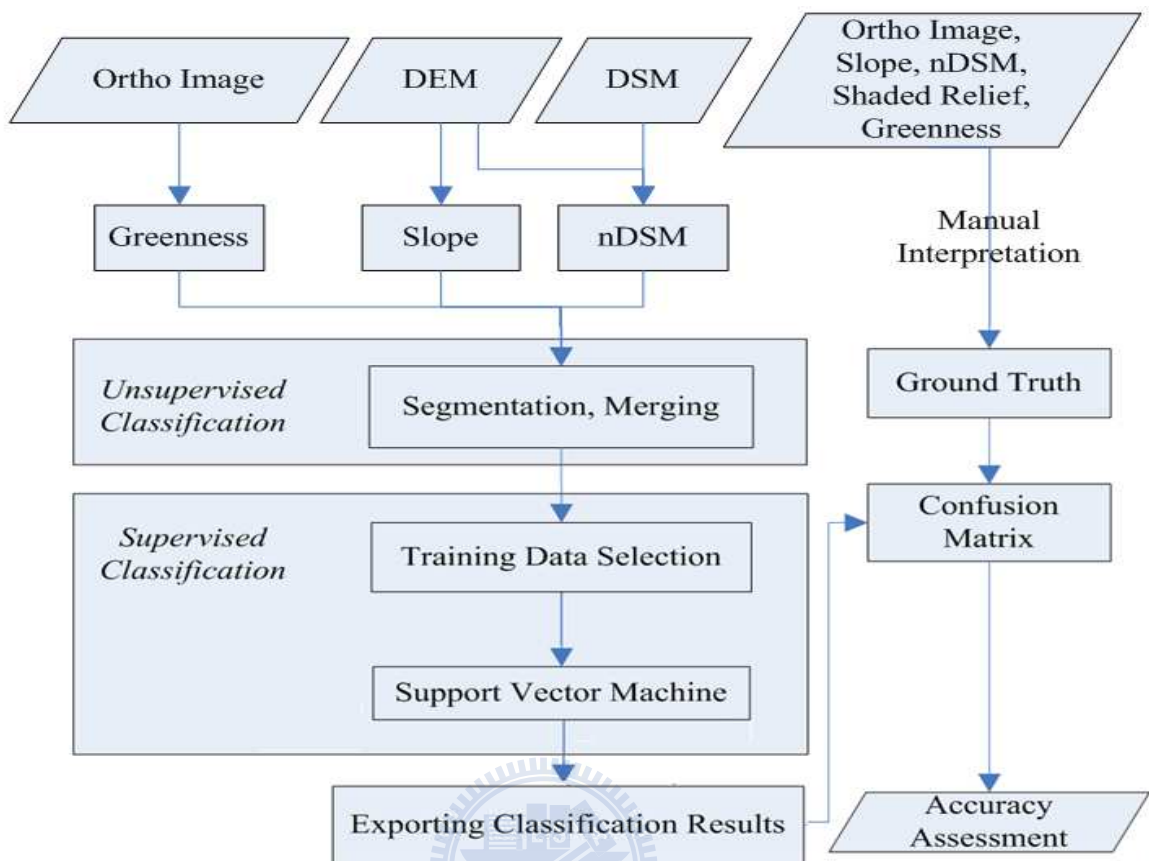
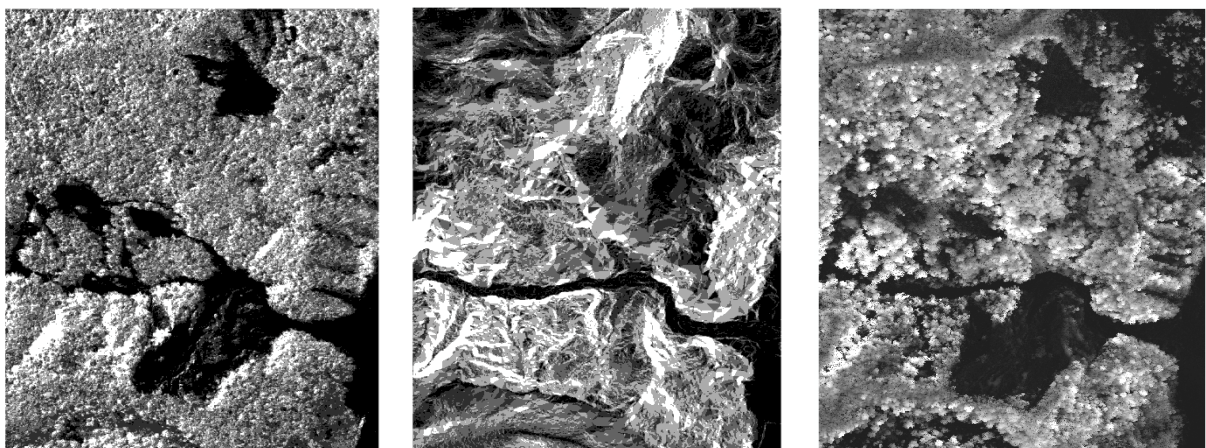


Figure 3.10 Flowchart of OOA data processing



(A) Greenness

(B) Slope

(C) nDSM

Figure 3.11 The three derivatives of orthophoto, DEM and DSM for data entry

(C) Testing site and materials

A test area is selected in I-Lan County of eastern Taiwan, the same as the one for the test of Method with indices of point cloud density in Paragraph 3.1.3 (C). The attributes of the data sets is shown in Table 3.2. For this test, only a subset of the area is used (Figure 3.12).

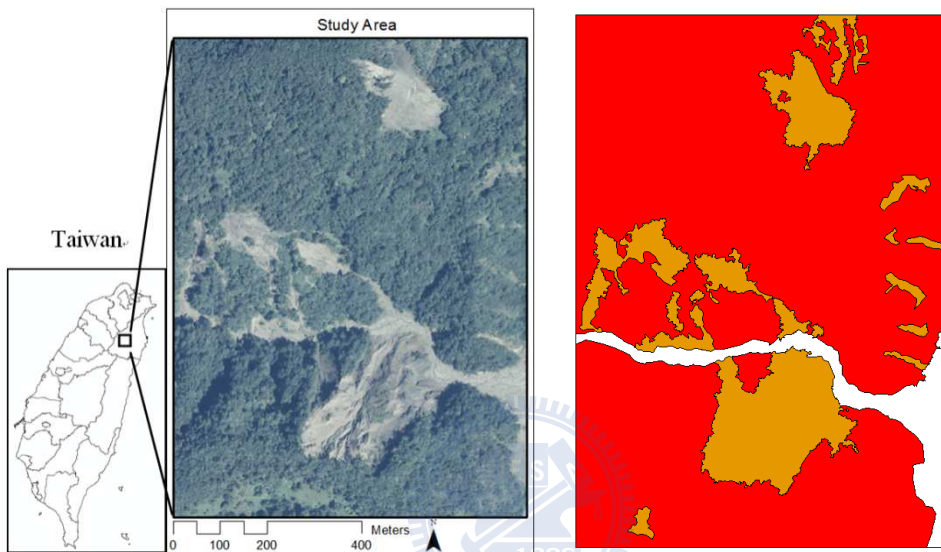
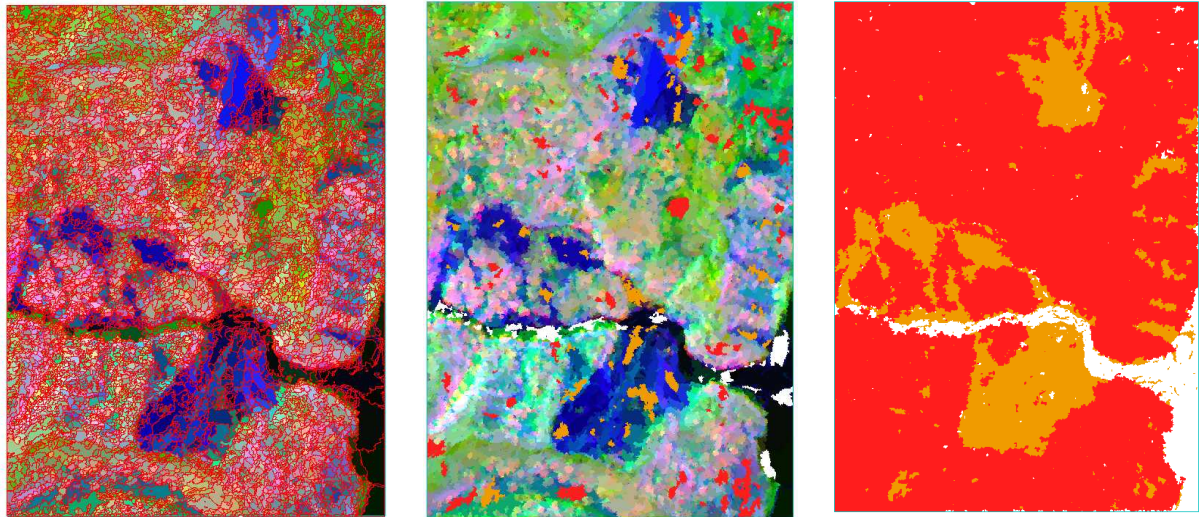


Figure 3.12 Study Area and Ground Truth for OOA Test

(D) Results and discussion

Figure 3.13 shows the results of segmentation and vector classification. The results generated by pixel-based classification are shown in Figure 3.14. The comparison between the results of the hybrid OOA method, pixel-based SVM method and those of ground truth is shown in Table 3.3. The Producer accuracy of landslide class by object-based method is 85.68% whereas that by pixel-based method is 72.01%. The user accuracy of landslide class by object-based method is 80.41% whereas that by pixel-based method is 76.2%.

Kappa coefficient and overall accuracy of object-based method are 0.817 and 93.4%, respectively. It is concluded that the hybrid OOA method proposed in this study is an effective method which is better than pixel-based method.

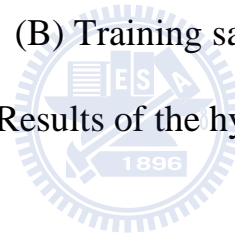


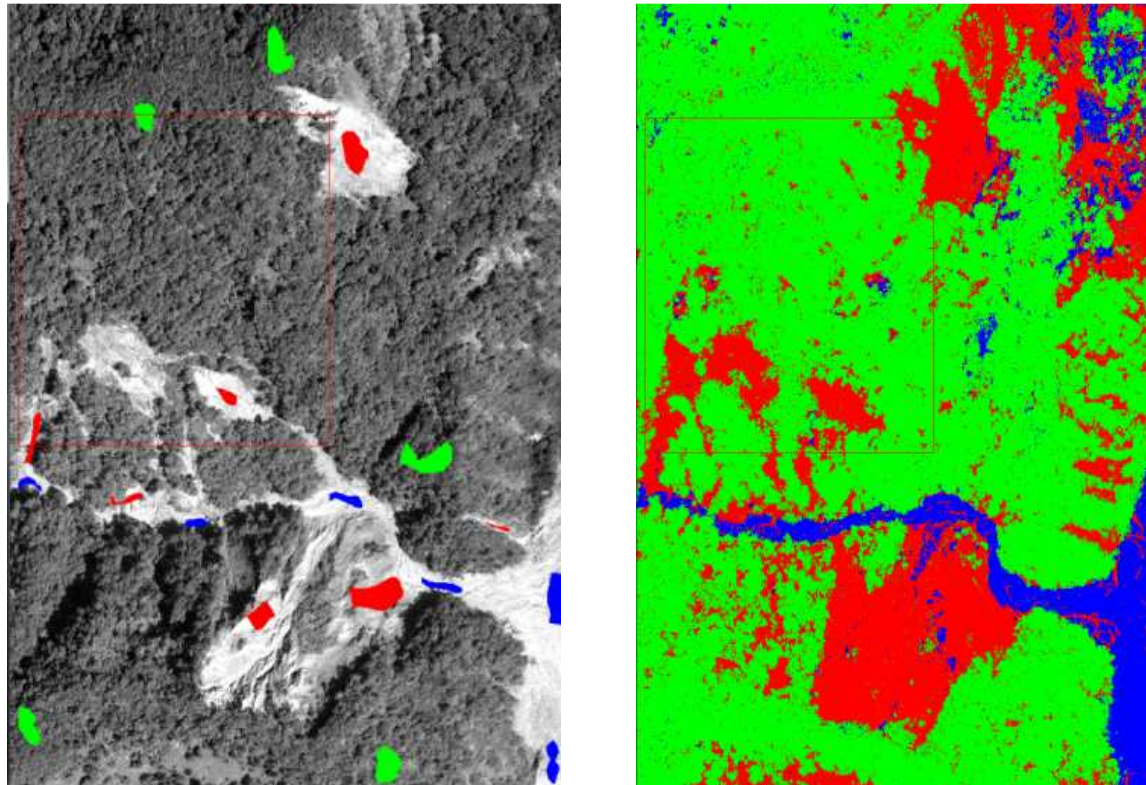
(A) segmentation

(B) Training samples

(C) OOA result

Figure 3.13 Results of the hybrid OOA method





(A) training areas on orthophoto

(B) Landslide map

Figure 3.14 The results generated by pixel-based SVM classification

Table 3.3 Confusion table of OOA classification and pixel-based classification

Object-based	PA%	UA%	Pixel-based	PA%	UA%
Landslide	85.68	80.41	Landslide	72.01	76.2
River bed	83.21	87.81	River bed	70.88	76.2
Vegetation	95.72	96.59	Vegetation	94.55	93.53
Kappa Coefficient = 0.817			Kappa Coefficient = 0.704		
Overall Accuracy = 93.4%			Overall Accuracy = 89.64%		

3.2 Detection of Deep-seated Landslides

3.2.1 Introduction

Expert-based method is the most popular method adopted for the detection of deep-seated landslides (PWRI, 2008; SWCS, 1992; ITRI, 1993). Because most

of the deep-seated landslides are either latent or located under forest cover, only a few of them which are in creeping or which are newly-happened in a catastrophe can be detected and treated. For deep-seated landslides, detection and characterization are the most important task before any mitigation measure can be taken or any inference of landslide kinematics and mechanics can be made.

There have been many studies using aerial photographs, satellite remote sensing and airborne LiDAR for the observation of the characteristic morphological features (Agliardi et al., 2001; Agliardi et al. al, 2009; Chigira, 2011; Chigira & Kiho, 1994; Chigira et al, 2003; Chigira & Yagi, 2006; Dewitte et al., 2008; Dramis & Sorriso-Valvo, 1994; Glenn et al., 2006; Ventura et al., 2011). Nevertheless, some automatic methods such as PIV and CosiCorr have been raised for detect and characterize deep-seated landslide of creeping type or large-scaled ancient landslide which are in metastability (Lo et al., 2009; Tseng et al., 2007). In this study, three methods are raised and discussed, namely (1) Expert-based Method - using LiDAR-derived shaded images or other enhanced images for visual interpretation; (2) Texture-related or OOA methods - demonstrated cases are reviewed but not tested with Taiwan case; (3) Multi-temporal change analysis - using simple DoD (Difference of DEMs) method to extract images for interpreting the activeness of the landslide.

3.2.2 Method 1: Expert-based Method

The mechanism for triggering a deep-seated landslide is complicated. Two major topics are usually adopted before further understanding of the mechanism, namely (1) detailed mapping of the features and the topography of the landslides for a description of the geospatial and geological environment; (2) susceptibility mapping and interpretation of the landslide for zoning different possibility of re-activeness.

For an ancient landslide under forest cover which may have re-activated several times in history, the delineation of the boundary and other features such as hummocky topography become the most critical part. Stereo-pairs of aerial photographs are usually used for this purpose. Figure 3.15(A) shows a 2005 high-resolution aerial photo (left) of the Gladstone, Oregon area, trees, houses, and roadways hide the contours of a large landslide. On the basis of this image, there is little geohazard risk in the area. In a DEM image derived from LiDAR data for the same area (right) the surface is created by digitally removing all vegetation and man-made structures, resulting in a true surface shape. The landslide scarps and toes in the middle of image are clearly visible. Statewide LiDAR mapping proposal was thus initiated to identify areas at risk in Oregon State (Lewis, 2006). Therefore, LiDAR-derived images become a superior surrogates of traditional aerial photographs being used for expert-based method due to its capability of virtual deforestation (Dewitte et al., 2008; Glenn et al.,

2006; Ventura et al., 2011).

The geomorphic features shown in Figures 2.2 and 2.3 are those to be observed on LiDAR-derived images. Figure 3.16 shows two examples of deep-seated landslides in LiDAR-derived image at I-Lan County. Figure 3.16 (A) and (C) are shaded-relief images of DEM whereas (B) and (D) are images of DSM. There are two deep-seated landslides on the images annotated on Figure 3.16 (A) and (B). Obviously, the top landslide is a recent one where the scarp remains and the lower one is older where the main scarp is covered by forest and becomes vague. On the DSM-shaded image (D) on which landslide boundary was not annotated, the boundary of the lower landslide is not obvious, whereas the scarps of the top landslide are conspicuous. In addition, a scarp to the north of the top landslide is becoming obvious if it is closely observed. Therefore, there is a high susceptibility of developing an even newer deep-seated landslide at this place.

Both shallow landslides and deep-seated landslides can be observed on these images. Another observation of these images. By comparison of the lower part of shallow landslides in Figure 3.16 (C)&(D) and Figure 3.14 (A), DSM-derived images give better contrast for shallow landslide areas where the area covered by landslides has smoother surface. However, for the interpretation of deep-seated landslides especially old ones, DEM-derived images give better results of feature mapping. In conclusion, the best practice should make use of all DEM and DSM data for this purpose rather than just use one of them.

Deep-seated landslides usually evolve for long time or re-activate when triggering factors prevail such as rainfall or earthquake. Evidences should be found in the field to support the observation on images.



(A) orthophoto

(B) LiDAR DEM

Figure 3.15 A comparison of two images: color aerial photograph (left) and shaded-relief image of airborne LiDAR DEM (right) (Lewis, 2006).

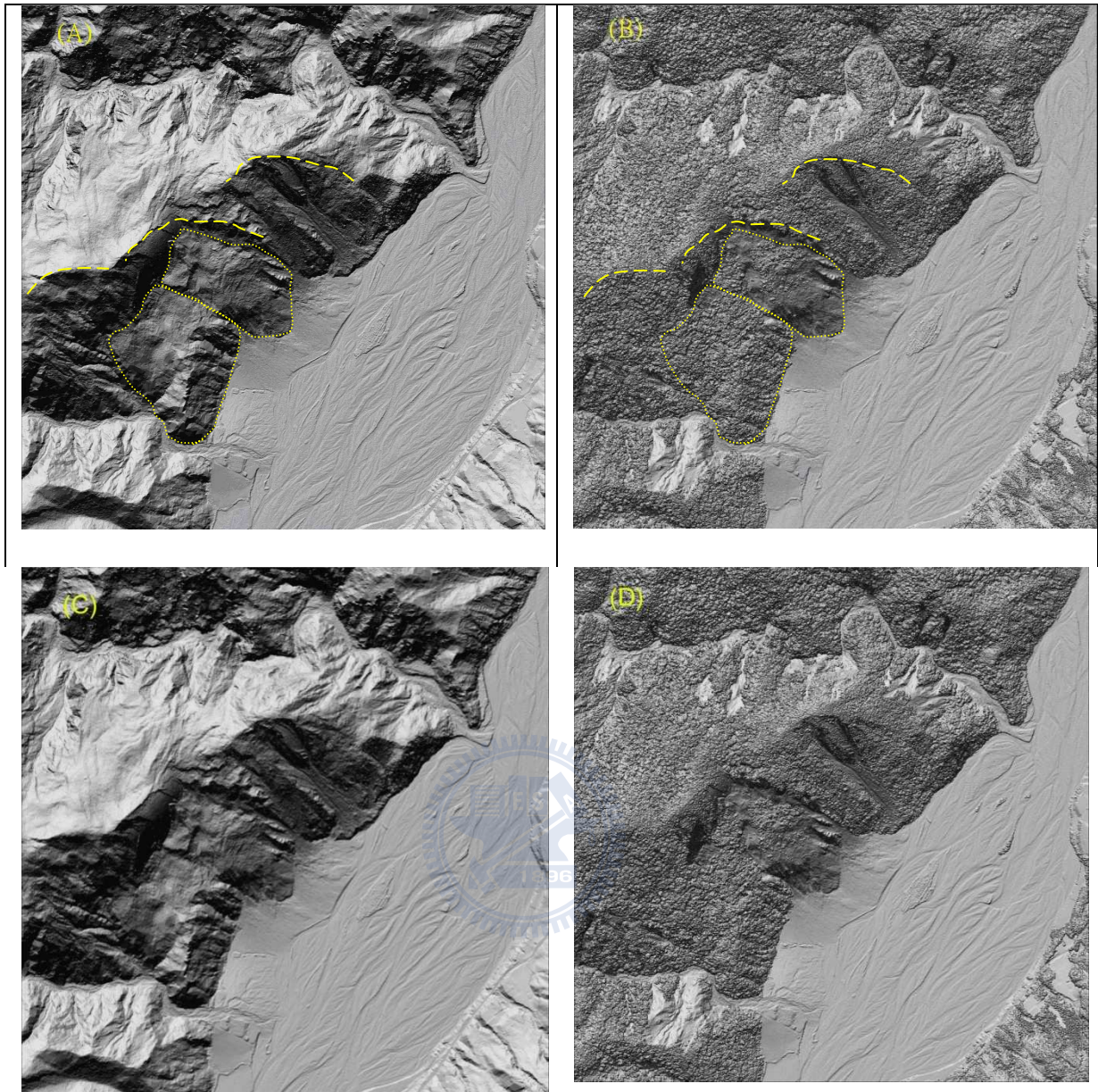


Figure 3.16 Deep-seated landslides revealed in LiDAR-derived image at I-Lan.

3.2.3 Method 2: Texture or OOA Method

This is one of the major academic research area in using LiDAR data for the investigation of deep-seated landslides (Dewitte et al., 2008; Glenn et al., 2006; Ventura et al., 2011; McKean and Roering, 2004).

The first example as shown in Figure 3.17 was made by McKean and

Roering (2004). Airborne LiDAR DEMs data was used to characterize a large landslide complex and surrounding terrain near Christchurch, New Zealand. It is found that the bedrock landslide is rougher than adjacent unfailed limestone terrain. Four statistical measures of surface roughness are raised and any of the statistics can differentiate landslide and unfailed area. The second example as shown in Figure 3.18 was published by Glenn et al., (2006). Similarly, roughness is the core point for the automatic detection of the landslide. The roughness of this study is done by semivariogram and fractal analyses. It is concluded in this case that topographic elements are related to the material types and the type of local motion of the landslide. Weak, unconsolidated materials comprising the toe of the slide, which were heavily fractured and locally thrust upward, had relatively high surface roughness, high fractal dimension, and high vertical and lateral movement.

Since roughness is the major concern in the automatic detection of landslides, not only for deep-seated ones but also for shallow landslides. As explained in expert-based method, contrast caused by surface roughness is the best indicator for visual interpretation. The usefulness of roughness for automatic detection of shallow landslides was also proved by local cases (Yang et al., 2010). Nevertheless, factors of deep-seated landslides are complicated and the geological and morphological environment of each individual landslide are not the same. Therefore, roughness may be a good indicator under certain conditions but it may not be a good indicator for other conditions. Figure 3.19 is

an example of Li-Shan area in central Taiwan (ITRI, 1993). The landslide complex in this area may not be easily detected by automatic method. The several segments of main scarps on top of the LiShan and several deep-dissected ditches are readily visible. There are also some prominent lineaments to the east of the landslide complex. This may give indications that complex structure control may take place. All these questions have to be answered by other means rather than just by the results of the interpretation of LiDAR-derived images.

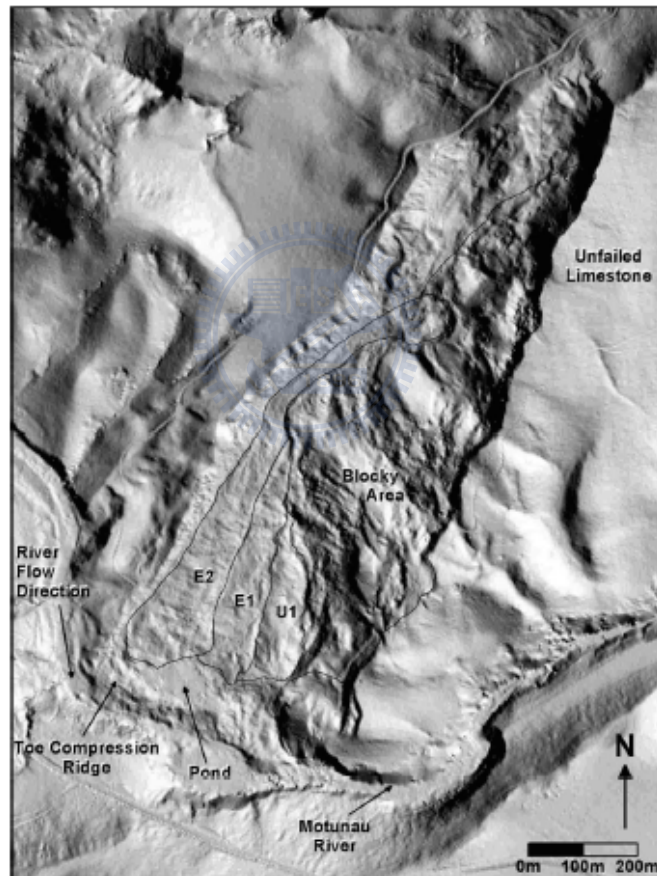
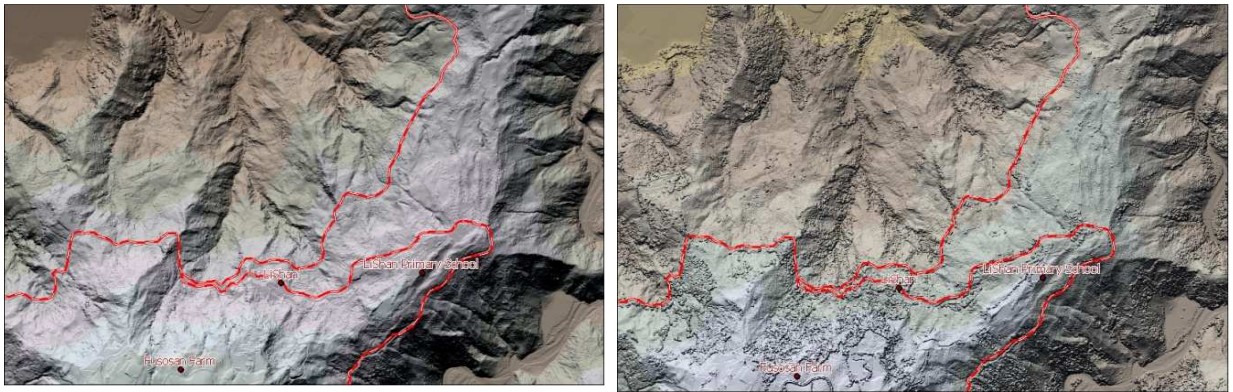


Figure 3.17 Shaded relief image of the Coringa Landslide and immediate surroundings. The primary kinematic units within the slide are earthflows E1 and E2, the area of compression U1 and the Blocky area with incorporated limestone blocks (McKean and Roering, 2004).



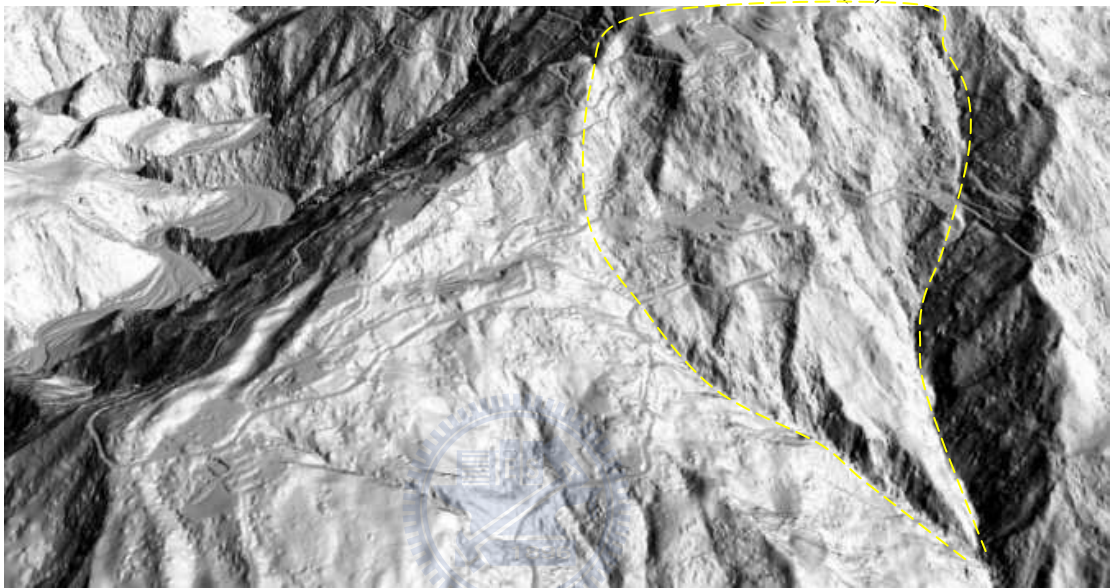
Figure 3.18 Shaded relief image of the Salmon Falls landslides for semivariogram and fractal analyses. UB=Upper block, B=Body, T=Toe.

(Glenn et al., 2006)

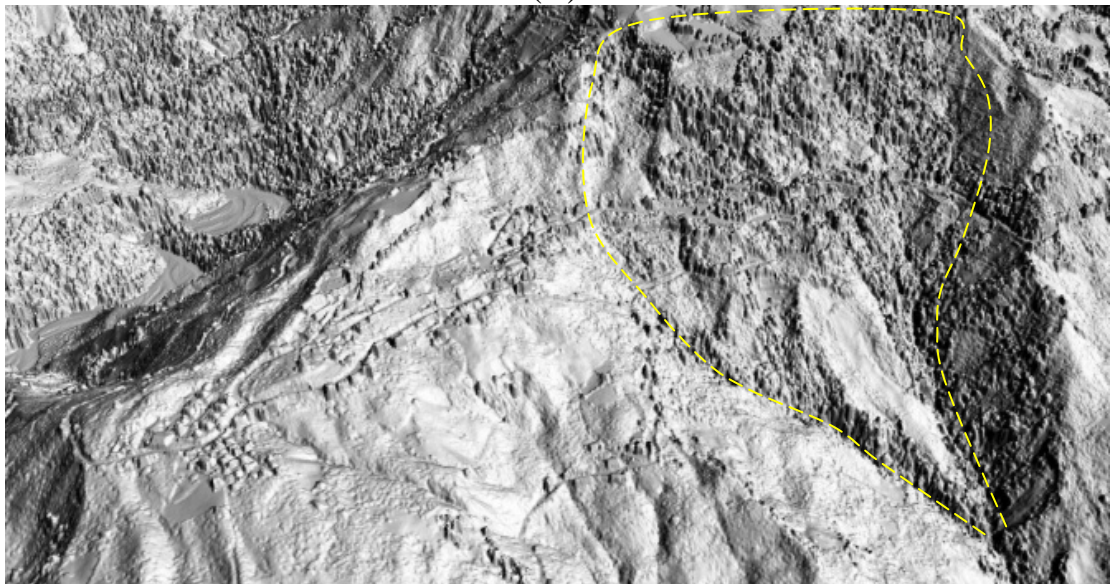


(A)

(B)



(C)



(D)

Figure 3.19 LiDAR-derivatives of Li-Shan landslide complex, central Taiwan

3.2.4 Method 3: Multi-temporal Analysis

(A) Introduction

The purpose of the analysis applying multi-temporal LiDAR data is to analyze the activity or susceptibility of the landslide. The method proposed for deep-seated landslide is a simple DoD method (Difference of DEMs). To demonstrate the potential of the simple DoD method, the three DEMs in Hsialin Slide obtained in three surveys are used.

Old deep-seated landslides may re-activated several times in history. However, this may evolve as long as more than a century time such as Tsaoling landslide, of which the first time of movement was recorded in 1862 due to an earthquake (Chen et al., 2005). Tracking of landslide displacements by multi-temporal DTMs either created by InSAR, photogrammetric or airborne LiDAR becomes important especially when multi-temporal LiDAR survey have been made (Dewitte et al., 2008; Ventura et al., 2011).

(B) Method

It is straight-forward to apply the difference of two DEMs for representing landslide volume caused by a landslide event (Liu et al., 2010 and 2011), e.g.

$$\Delta V_{21} = \sum (DEM_{T_2} - DEM_{T_1}) \quad (3.10)$$

Where DEM_{T_2} represents the DEM of the accurate topography after the event and DEM_{T_1} represents that before the event. ΔV is the volume change after the event, which is a summation of the difference values of each individual

corresponding pixels of DEMs. A negative value of ΔV indicates the area is erosive. Whereas a positive value of ΔV indicates the area is sedimentary.

Basic issues behind the method of simple subtraction of two DEMs include a common datum of different datasets and data quality of them. Simple subtraction method would not be applicable if the uncertainties are too large due to these two basic issues. If two DEMs are generated by two surveys using different datum, it is required to unify both the geodetic and the vertical systems. In addition, to assure the quality of DEM, it is required to abide by a strict survey plan and to apply a solid validation process. The two DEMs used in this study are both surveyed with identical geodetic and vertical systems, namely TWD97 and TWVD 2001. A strict guideline becomes a pre-requisite for this purpose. Data quality should be checked to validate the datasets. The experimental data are obtained by applying a common LiDAR Survey Guideline (MOI, 2006).

The three datasets obtained for this study are with two different height systems. One is with orthometric height and the other two with ellipsoid height. Therefore, geoid undulation of the study area was applied to standardize these three datasets to a common height system either orthometric or ellipsoid height. In our case, ellipsoid height system is used. This step has to be cautious and checked before applied the simple difference method. Three difference images are derived at first for further interpretation, including V_{21} , V_{32} , and V_{31} , e.g.

$$\Delta V_{21} = \sum (DEM_{T2} - DEM_{T1}) \quad (3.11)$$

$$\Delta V_{32} = \sum (DEM_{T_3} - DEM_{T_2}) \quad (3.12)$$

$$\Delta V_{31} = \sum (DEM_{T_3} - DEM_{T_1}) \quad (3.13)$$

(C) Study site and materials

One of the most catastrophic disaster in Taiwan is Hsiaolin Slide triggered by typhoon Morakot occurred on 9th August 2009 at Shiaolin Village in Kiaosiung City of Southern Taiwan (Dong et al., 2011; Juang and Lee, 2011; Hu et al., 2010; Lin et al., 2011)(Figure 3.20). Three times of airborne LiDAR survey were conducted in this area. The LiDAR images of the respective times are shown in Figure 3.21. The major event of typhoon Morakot occurred on 9th August 2009. Therefore, the airborne LiDAR survey conducted in June 2006 portrayed the topography before the event whereas the LiDAR survey conducted on 18 and 23 June 2010 portrayed the topography after the event. A catastrophic change of the topography can be expected. Another airborne LiDAR survey for the same area was conducted on 16 and 27 October 2010, that is four months after the former survey. A comparison of the topographic change between June and October of 2010 can reveal the change of post event process and local instability in this period of time can be observed.

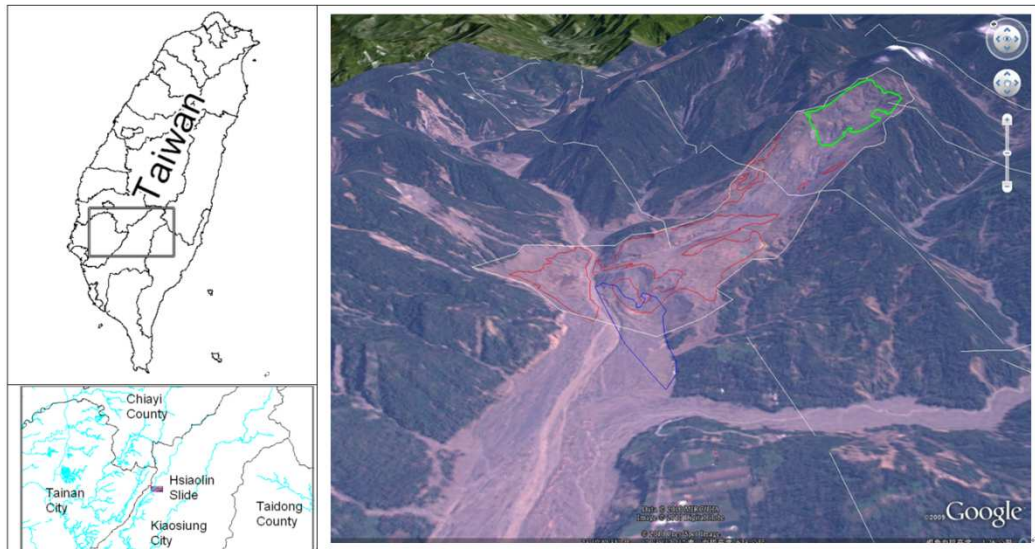
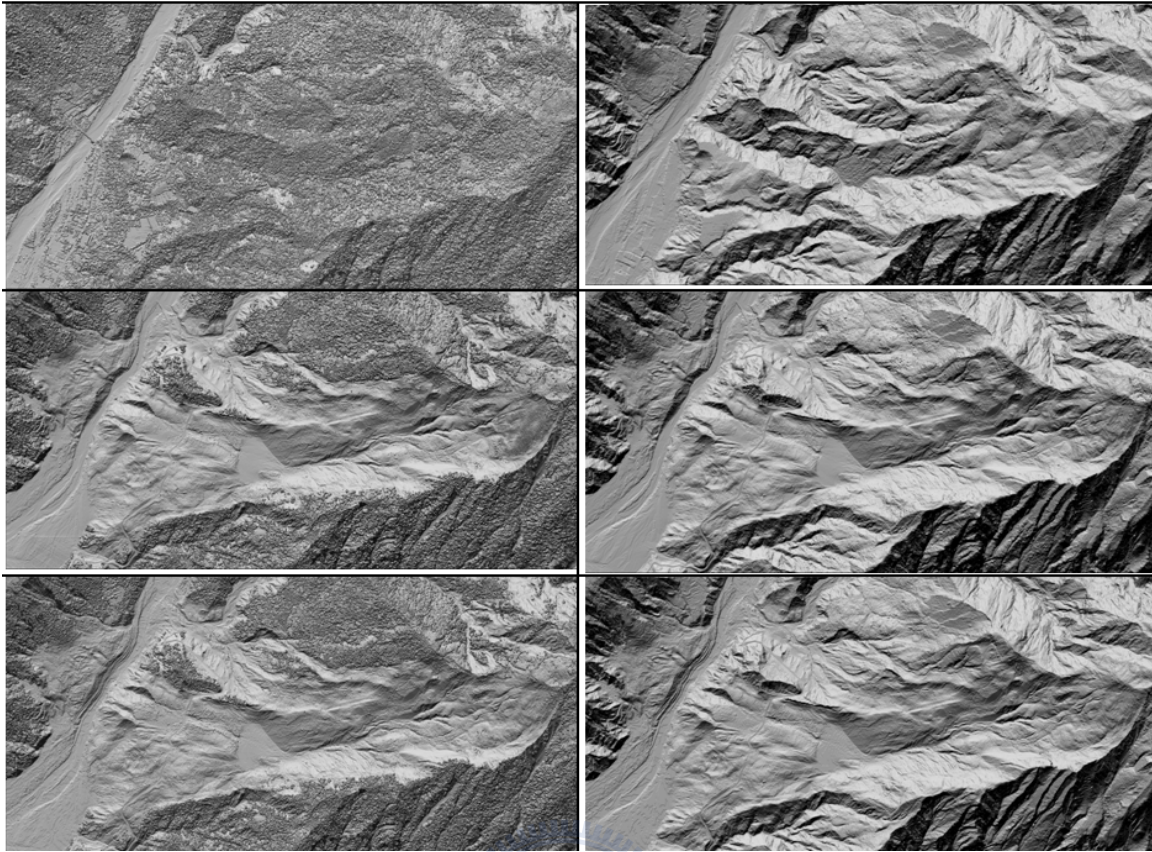


Figure 3.20 The location of Hsiaolin Slide and the vicinity. The landslide boundary is draped on the 3D perspective view of aerial photograph taken after the event.





Legend	DSM 2006	DEM 2006
	DSM 2010-06	DEM 2010-06
	DSM 2010-10	DEM 2010-10

Figure 3.21 Three DSMs and DEMs of Hsiaolin Slide

(D) Results and discussion

Some observations of the results of T2 as compared to T1 and those of T3 as compared to T2 will be presented in this paragraph.

The difference of T2-T1 reflects the topographic change of typhoon Morakot, the main event. As shown on top diagram of Figure 3.22, the area coverage of Hsiaolin Slide is 224.3 hectares with A-A'=3059 m, A-B=1880 m, B- B'=1516 m, A-B-B'=3396 m, and A-B'=3315 m. In middle diagram of

Figure 3.22, isoplethic lines are plotted every 5 m from -85 m to +85 m for the range of the difference between T2 and T1 from -86.87 m to +85.66 m. Two major depleted areas and four accumulated areas can be readily identified. N1 is estimated with a negative volume of 26,515, 325 m³. This area is the main part of the disastrous landslide with a deepest sliding mass of 86.87 m in depth. N2 is with a negative volume of 1,614,475 m³. This is a secondary landslide along old stream valley. P1 is with a positive volume of 4,638,809 m³. The accumulated landslide deposits were located in the right-hand side of Chisan River which is opposite to the location of the sliding mass. P2 with a positive volume of 8,852,825 m³. The major part of the sliding materials were moved along an old stream valley and accumulated in the valley bottom, thus the deepest deposition with +85.66 m was located in this part.

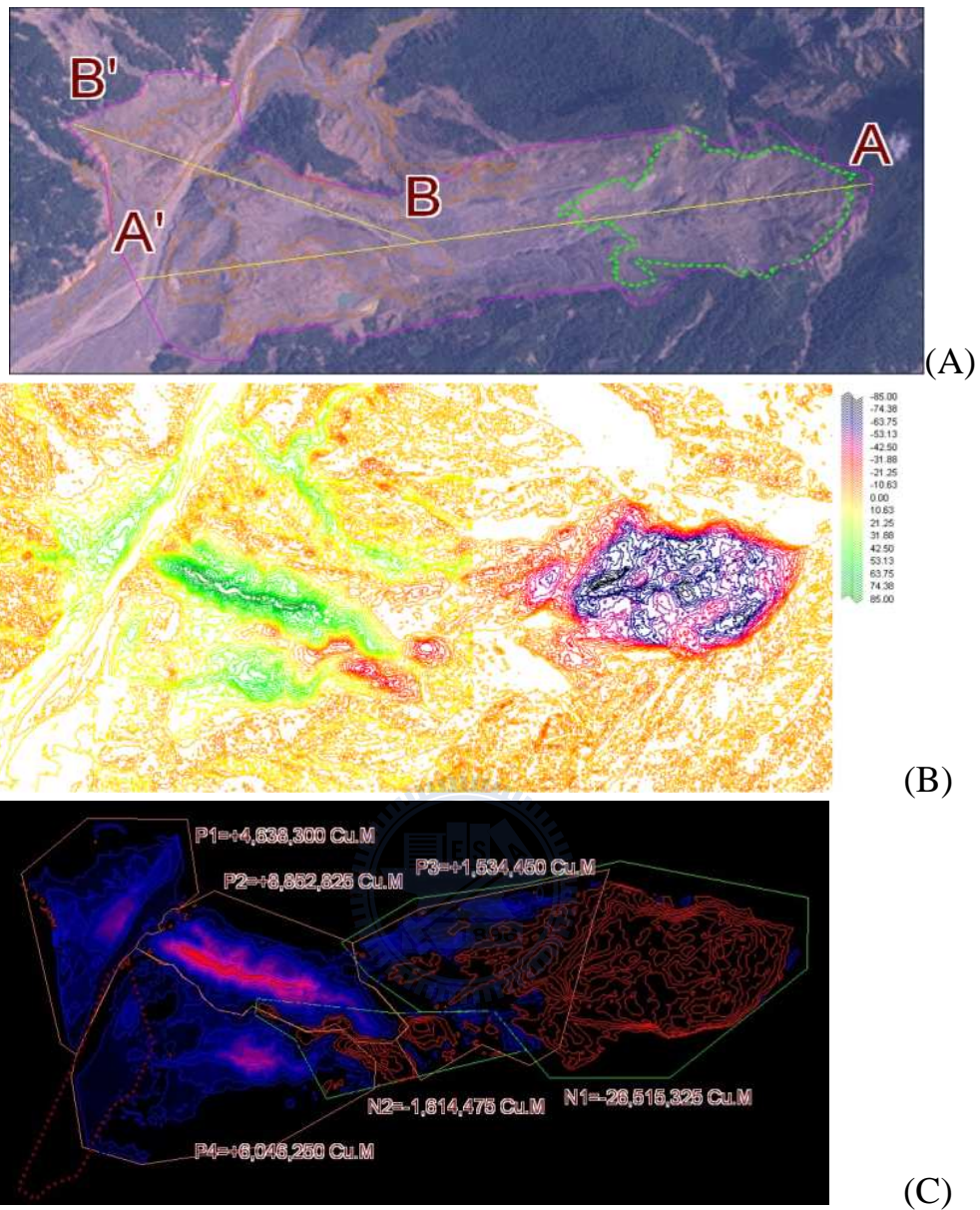


Figure 3.22 Topographic Features of Hsiaolin Slide and its subdivisions

The difference of T3-T2 reflects the topographic change after the main event typhoon Morakot. A distinct deposit of 48,960 m² and a depleted area of 34,070 m² can be observed on the upper part of the landslide which can be further identified in Figure 3.23. The deepest depth of the deposit is 37 m and the largest depth of the depleted area is 26 m. In other words, after the main event of typhoon Morakot, with the change from June to October, local slope of

instability was readily identifiable on the difference image. Figure 3.24 is a longitudinal cross section of Hsiaolin Slide, showing that the original slope of the depleted area was 22.3° (β) and the resulted slope after sliding event became 31.7° (α). If we look closely at the ground surface after the event as shown in Figure 3.25, there were unconsolidated materials remaining on the steep slope of the top part of the landslide, which are the origin of the re-activated materis.

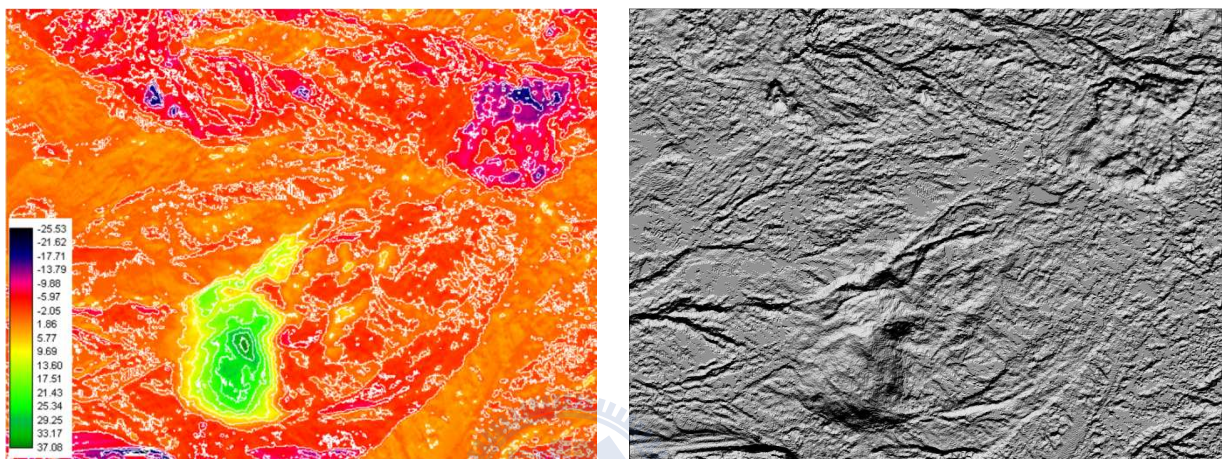


Figure 3.23 (A) color coded image of V32; (B) hsaded relief image of V32.

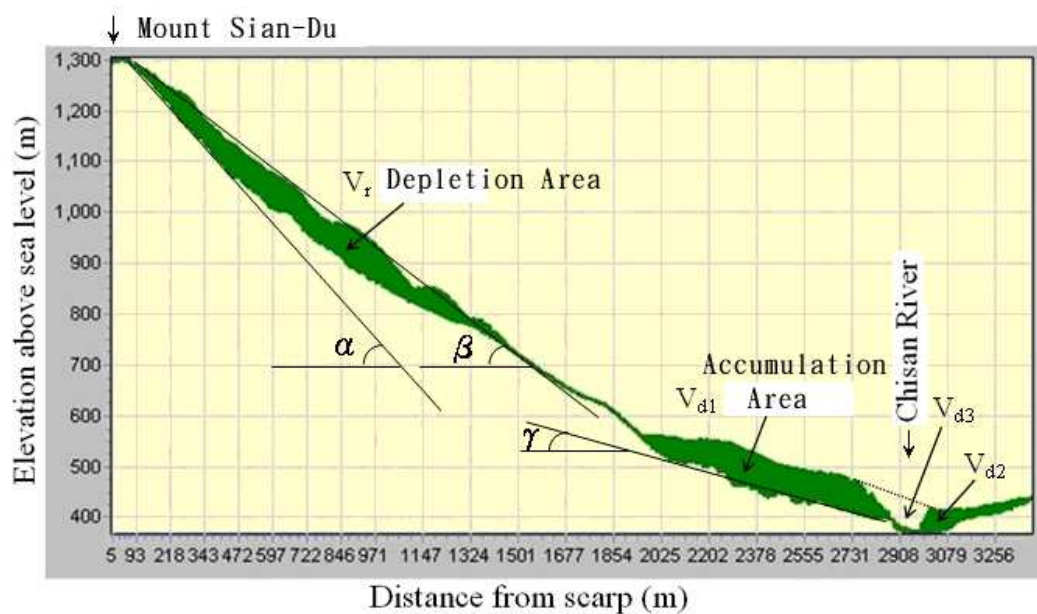


Figure 3.24 Cross section of Hsiaolin Slide along A-B-B' shown in top diagram of Fig. 3 $\alpha=31.7^\circ$, $\beta=22.3^\circ$, $\gamma=8.6^\circ$.



Figure 3.25 A close-up of the depletion area of Hsiaolin Slide. Remnants of unconsolidated materials still existed on the bare surface. The dash-line is the isoplethic line with -20 m. The area covers 48.68 hectares.

In summary for the multi-temporal analysis:

- (1) Multi-temporal airborne LiDAR datasets are useful for quantifying the time-series change of deep-seated landslides in the physiographic settings of Taiwan.
- (2) Simple difference method can be applied for extracting the change of topographic surface between two consecutive time. However, precautions of common datum and consistent accuracy of respective datasets have to

be maintained.

- (3) A national airborne LiDAR project is to be implemented from 2010 to 2015 (Liu & Fei, 2011). Multi-temporal airborne LiDAR data will become available for most of the area in Taiwan. The importance of applying multi-temporal analysis become obvious.
- (4) Movement slip vectors might be able to be obtained by further study using PIV or CosiCorr methods.



Chapter 4 Landslide Monitoring and Volume Change Analysis

Using Airborne LiDAR Data

In this chapter, methods of volume estimation for both individual landslide and whole study area are proposed. Experiments for landslide volume change with airborne LiDAR data before and after the specific event are presented and an empirical power law is derived to model the relation between area A (m^2) and volume V (m^3) of landslides by using the results of area and volume of individual landslides.

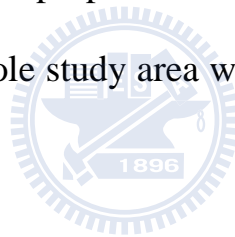


4.1 Introduction

The most urgent and fundamental issue raised after a landslide disastrous event is to understand the most up-to-date status of the disaster for the purposes of disaster emergency response and prevention. One of the key issue is to know how many landslides and where are they or how big is the landslides or even how much sediments will it be generated by the event. Therefore, remote sensing techniques are employed extensively (Rau et al., 2007; Bell et al., 2005&2006; Joyce, 2009; Teeuw, 2007; Highland and Bobrowsky, 2008).

Several techniques such as DInSAR, LiDAR, GPS, and aerial photogrammetry are capable of supplying accurate 3D topographic data (Tarchi

et al., 2003; McKean and Roering, 2004; Chen et al., 2005&2006; Glenn et al., 2006; Demoulin, 2006; Jaboyedoff et al., 2009&2010&2012). Because the archive of old aerial photographs in Taiwan contains around one million of aerial photographs starting from 1943, stereophotogrammetric analysis of aerial photographs can be a good source for obtaining DEM and DSM for understanding either the evolution of the landscape or the change of volume in a specific event. Nevertheless, the national LiDAR mapping program (Liu and Fei, 2011) will form a basis for estimate volume change of landslides if additional airborne LiDAR survey is conducted after an event. Therefore, the main objective of this research is to propose methods of volume estimation for both individual landslides and whole study area with airborne LiDAR datasets before and after the specific events..



4.2 Method of Landslide Volume Analysis

For the estimation of landslide volumes in a study area, two methods are proposed: (1) Simple DoD Method; and (2) Method of Accumulating Individuals. For the estimation of each individual landslide, three methods are proposed: (1) Method of 3D Sections; (2) Method of Average Sections; and (3) Grid Method. The whole area estimation approach and the individual landslide estimation approach will be discussed as follows:

(A) Whole Area Estimation Approach

As described in the Method of Multi-temporal Analysis for deep-seated

landslide, the Simple DoD Method is a Difference of DEMs approach with a simple and straight forward formula, e.g. $\Delta V = \Sigma(\text{DEM}_{T2} - \text{DEM}_{T1})$, where DEM_{T2} represents the DEM of the accurate topography after torrential event and DEM_{T1} represents that before torrential event. ΔV is the volume change after the event. A negative value of ΔV indicates the area is erosive. Whereas a positive value of ΔV indicates the area is sedimentary.

Figure 4.1 shows an example of the DoD Method. When a simple overlay subtraction is made with the 2010 DEM being subtracted by 2005 DEM, the resultant image will be a map of depletion (with negative value) and accumulation (with positive value). However, if it is inspected closely with re-classed image as shown in Figure 4.2. All the area of positive value (possible deposits) is masked out with a value of 0 and the all the area of negative value (possible landslides) is assigned a value of 1. Obviously, the portion of the negative area is too big and most of the shapes of the possible landslides are not correct. Too many isolated irregular spots can be observed. This indicate too many commission errors are included. The threshold method is thus used to filter out some low values due to uncertainties of the datasets and other environmental issues. The total estimated volume for Figure 4.2(A) when threshold is not applied is $13,193,828 \text{ m}^3$, whereas the total estimated volume for Figure 4.2(B) when threshold is set as -3 m is $10,360,912 \text{ m}^3$. The difference of volume of these two thresholds is as large as $2,832,916 \text{ m}^3$ ($\sim 21.47\%$). In Figure 4.2(B), in addition to spotted negative areas, it is also observed that there

are negative areas along the streams. This is due to down-cutting of the stream in this up-stream area. Therefore, volume of the so-called landslides may be over-estimated. In an operational sense, manual editing will be required to filter out these areas for a better estimation.

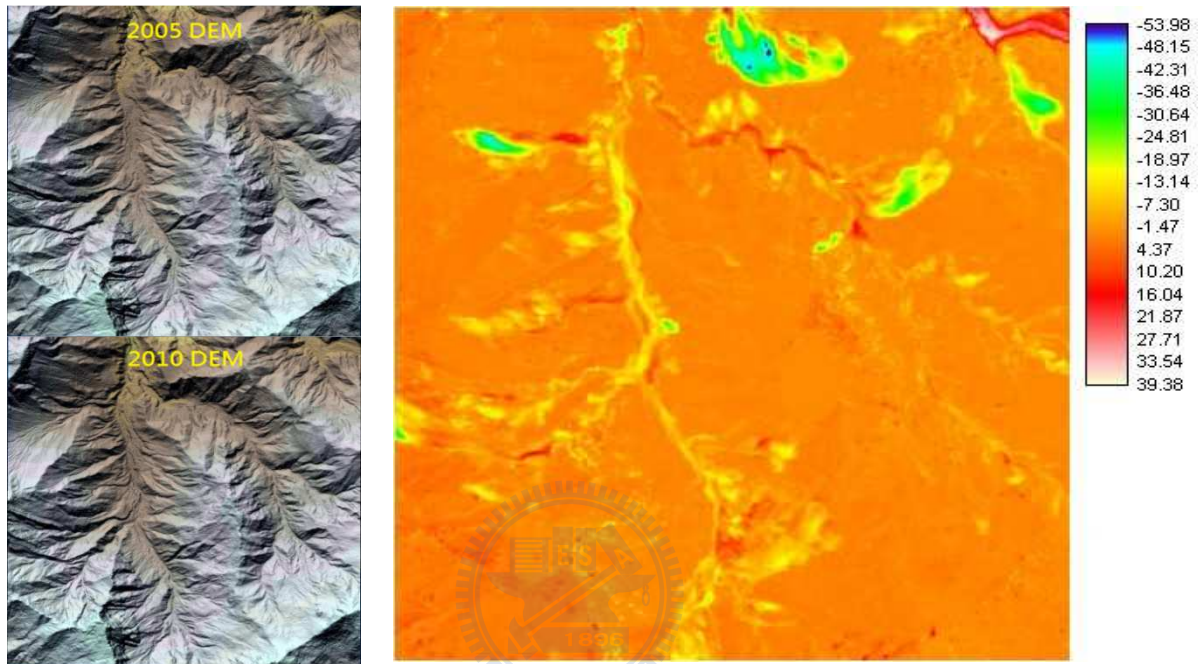
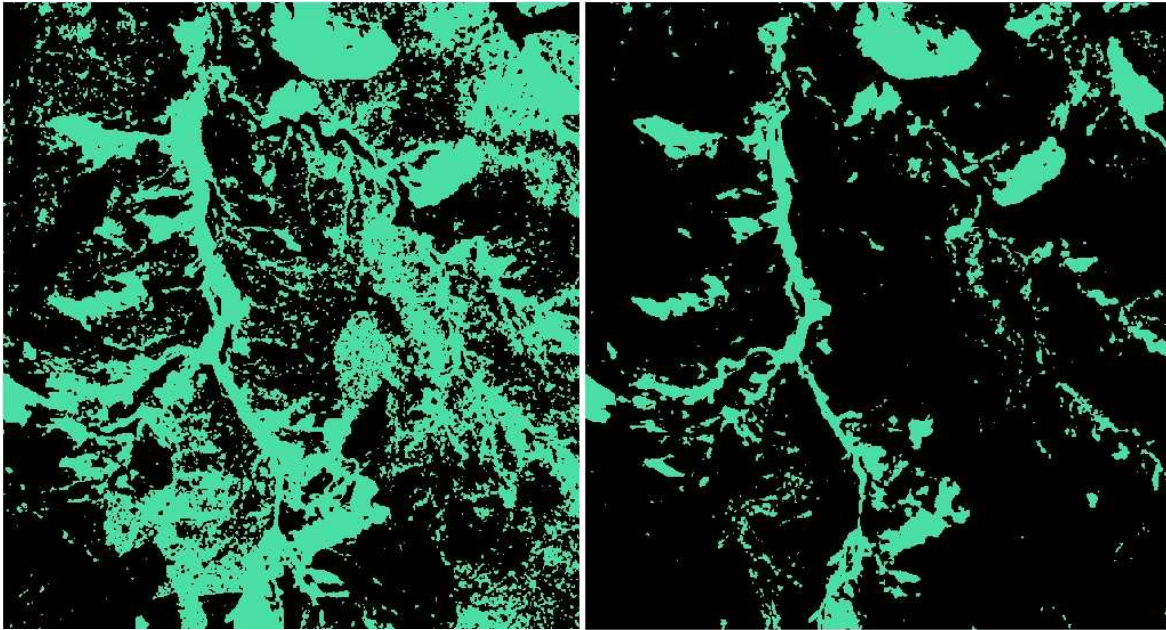


Figure 4.1 A simple difference of 2010 DEM and 2005 DEM and the DoD

result where the legend shows the value of the difference in meters.



(A) threshold = 0

(B) threshold = -3 m

Figure 4.2 Different thresholds applied to the DoD results: (A) not applied;

(B) a threshold of -3 m.

It is also mentioned in the Method of Multi-temporal Analysis for deep-seated landslide, basic issues behind this method include uncertainties such as common datum, data quality, and environmental issues. Especially, the major uncertainties are from the areas that covered by forest. Methods can be used to cater for these issues including (1) the masking method which applies a mask for the forested land, (2) the point-cloud-merging method which merges point clouds of the two respective survey for editing, (3) full waveform method to search for more ground points under forest, and (4) others. These methods remain for further study.

For the estimation of landslide volumes in a study area, the alternative for

the Simple DoD Method is the Method of Accumulating Individuals which estimates the volume (V) by accumulating individual volume (v_i) of all landslides in the study area. The method of the estimation of each individual landslide will be given in the following section. The formula is described as follows:

$$V = \left(\sum_{i=1}^n v_i \right) \quad (4.1)$$

where V is the landslide volume; n is the total number of landslide; v_i is the volume of each of the individual landslides in the study area.

As shown in Figure 4.3, with the assistance of ancillary information and other LiDAR-derived images, each individual landslide can be extracted from the overall landslide map of the whole study area generated by the simple DoD method. Subsequently, the total volume of the study area can be obtained by adding up all the individual landslide volumes.

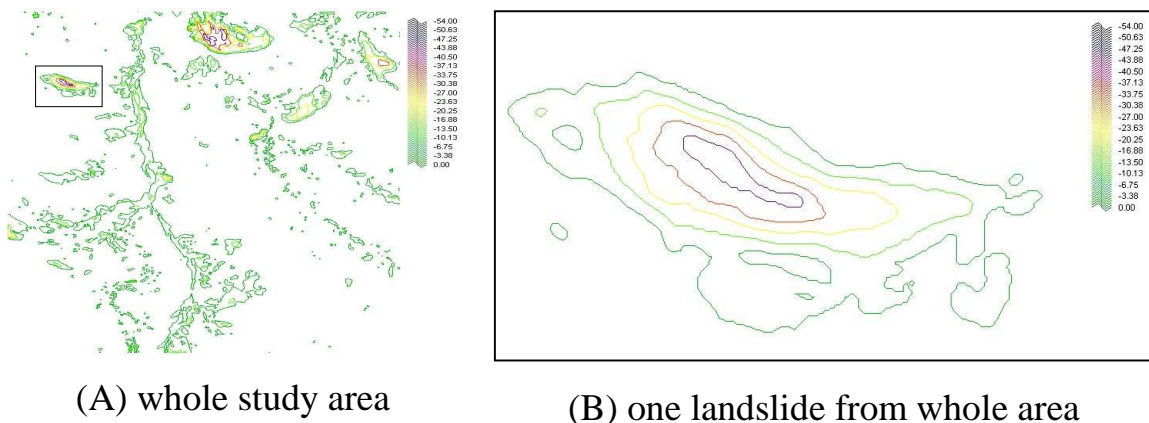


Figure 4.3 Each individual landslide (B) can be extracted from the overall landslide map (A) generated by DoD method.

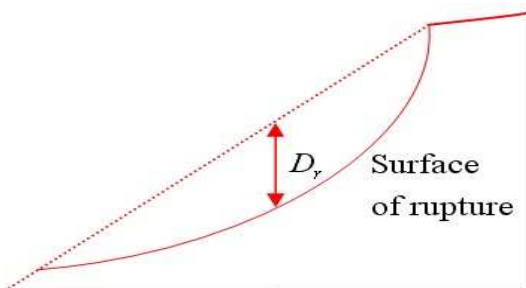
(B) Individual Landslide Estimation Approach

For the estimation of each individual landslide, three methods are proposed: (1) Method of 3D Sections; (2) Method of Average Sections; and (3) Grid Method.

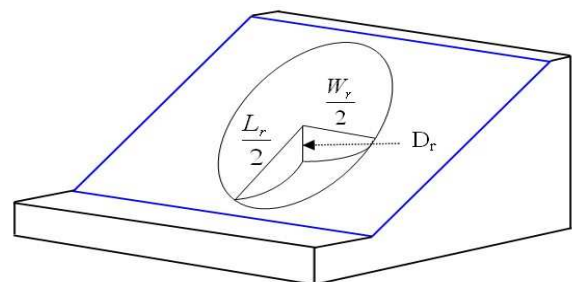
Method of 3D Sections is a method using three landslide features to represent a landslide body, i.e. (1) W_r : Width of surface rupture; (2) L_r : Length of surface rupture; and (3) D_r : Depth of surface rupture (Figures 2.3 and 4.4). In this method, a landslide body is represented by the lower half of an ellipsoid. This method is useful for estimating a landslide volume by in-situ measurements. And, it can be applied after the specific event without referring to measurements of the land surface before the event. The formula is described as follows:

$$V = \frac{1}{6} \pi D_r \times W_r \times L_r \quad (4.2)$$

where V is the landslide volume; D_r is the depth of surface rupture; W_r is the width of surface rupture; L_r is the length of surface rupture.



(A) cross section



(B) 3D perspective

Figure 4.4 Landslide volume estimation using three landslide dimensions

Method of Average Sections (Figure 4.5) is a method using the area of fixed-interval cross sections along the longitudinal axis of the landslide to estimate the volume. The formula is described as follows:

$$V = h \left(\sum_{i=1}^n A_i \right) \quad (4.3)$$

where V is the landslide volume; n is the total number of cross sections; h is the fixed interval between two cross sections; A_i is the area of i th cross section.

Grid Method is a method using a grid for the difference between the DEMs before and after landslide event to estimate the landslide volume. Each grid element has a value which represents the depletion (with negative value) or accumulation (with positive value) in the event. In the extent of the landslide, the absolute value of each grid element is the thickness or depth of the landslide at the specific site. Therefore, it is a straight-forward method when multi-temporal LiDAR DEMs are used for landslide volume estimation. The formula is described as follows:

$$V = A \left(\sum_{i=1}^n \sum_{j=1}^m h_{ij} \right) \quad (4.4)$$

where V is the landslide volume; A is the unit area of each grid element; m and n are the row and column number of the grid; h_{ij} is the depth of the landslide at the pixel(m,n).

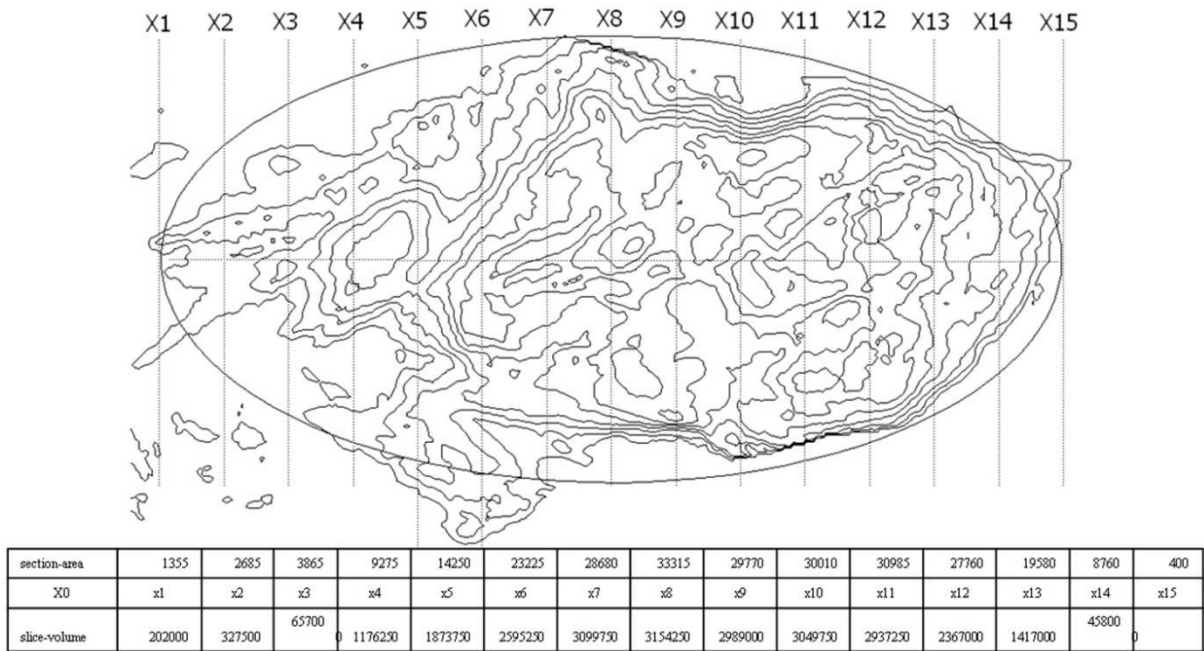


Figure 4.5 Landslide volume estimation using areas of cross sections of fixed-interval

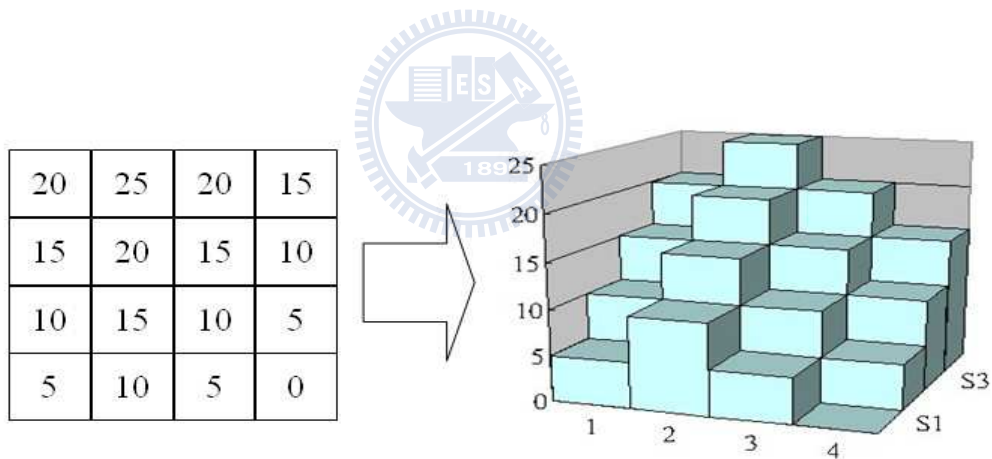


Figure 4.6 Landslide volume estimation using a grid of landslide depths.

In addition, because the area (A) and volume (V) of each individual landslide can be estimated by aforementioned Grid Method if multi-temporal DEMs are used, it is straight forward to derive the relationship between A and V for the study area.

4.3 Study Area and Materials

For demonstrating the volume estimation of each individual landslide, the case of Hsiaolin Slide will be give first. The study area and materials can be referred to the discussion in Method 3 (Multi-temporal Analysis) for deep-seated landslide detection in Paragraph 3.2.4(C) and Figures 3.19 and 3.20.

An additional site in Namashia District of Kaohsiung City (Figure 4.7) will be used to demonstrate (1) the extraction of individual landslides from the overall landslide map; (2) Method of Accumulating Individuals; and (3) Derivation of the power law for the relationship between area (A) and volume (V) of the study area.

The mapname of the study area is Ternbausan-One in Namashia District, southern Taiwan (Figure 4.7), about 2 km apart from Hsiaolin Slide. The extent is about 2,579 m x 2,775 m, around 7 km². There are very few landslides on orthophoto taken in 2005 whereas landslides are everywhere on Formosat-2 orthoimage taken in 2010 of the same area. As shown inFigure 4.8, two times of LiDAR data are used, for representing the accurate topography before and after 2009 Morakot rainfall event. The first LiDAR dataset was acquired in 2005 (MOI, 2006) and the second one in 2010 (SWCB, 2010). The point density of both datasets is more than 1 point/m². The grid-size of final DEM is 1 m. The orthometric height of each grid cell conforms to the accuracy standards required by the National Draft LiDAR Specifications (MOI, 2006). The premises for applying two DEMs for landslide volume estimation require that both the datum

and the quality of the two DEM datasets are maintained. To assure the quality of the DEM, strict standard operation procedures are followed (MOI, 2006).

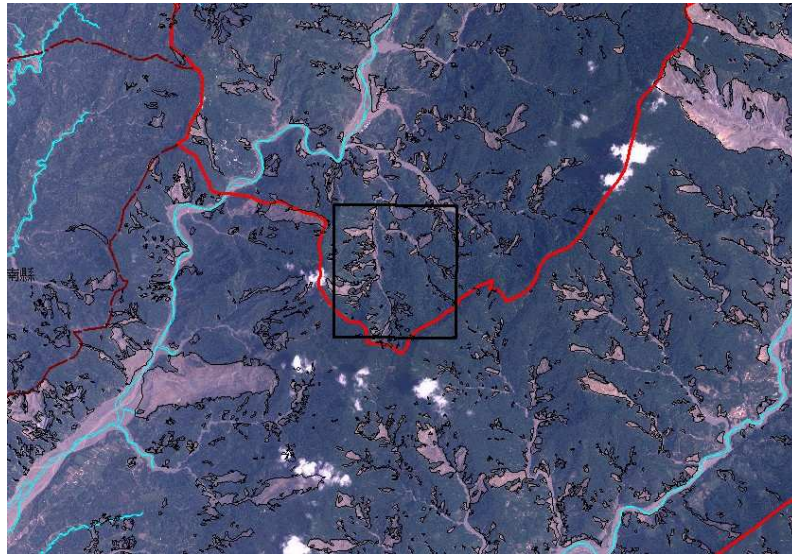
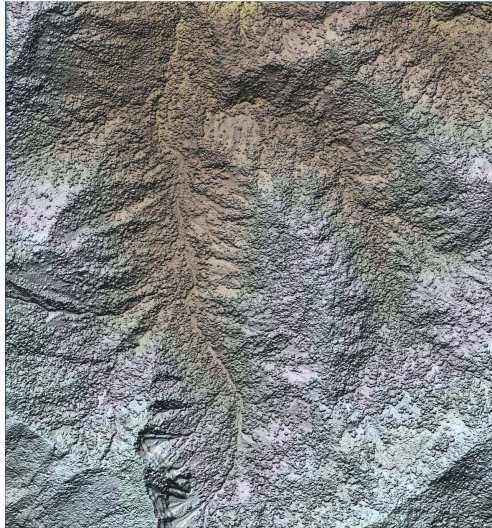


Figure 4.7 The study area of Namashia District of Kaohsiung City.

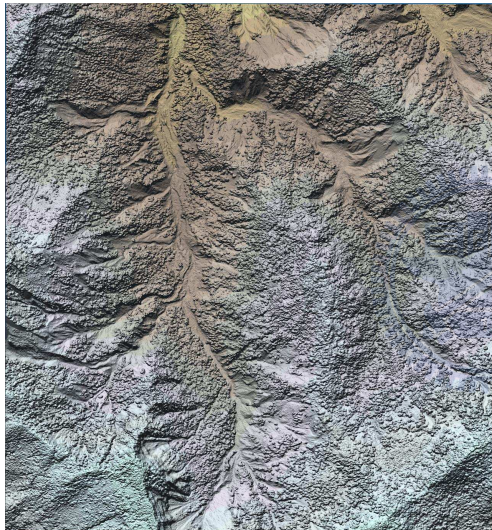




(A) 2005 DSM



(B) 2005 DEM



(C) 2010 DSM



(D) 2010 DEM

Figure 4.8 LiDAR Data used in Namashia study area

4.4 Results and Discussion

4.4.1 Hsiaolin Case for Individual Landslide Estimation

The results of applying the three methods of individual landslide will be presented in the paragraph, including (1) Method of 3D Sections; (2) Method of

Average Sections; and (3) Grid Method.

As shown in Figure 3.23, because the travel distance of Hsiaolin Slide (~2000 m) is larger than the length of rupture surface (~1500m), the landslide volume can be estimated by Method of 3D Sections. Figure 4.9 shows the Hsiaolin Slide and its subdivisions. In total, there are 7 subdivisions with negative values. Subdivision A is the major landslide body and it is used for demonstration of the Method of 3D Sections. When the ellipse for the landslide is selected, the L_r (2376 m) and W_r (695 m) can be easily measured whereas the depths to the rupture surface are variable in all places of the landslide. An estimation of a representing depth has to be made. It is known that the deepest depth is 85 m. An intelligent guess of the average depth would be from 50 m to 85 m. And, by applying formula 4.2, the estimated volume may vary from 25,036,378 m³ to 42,575,390 m³.

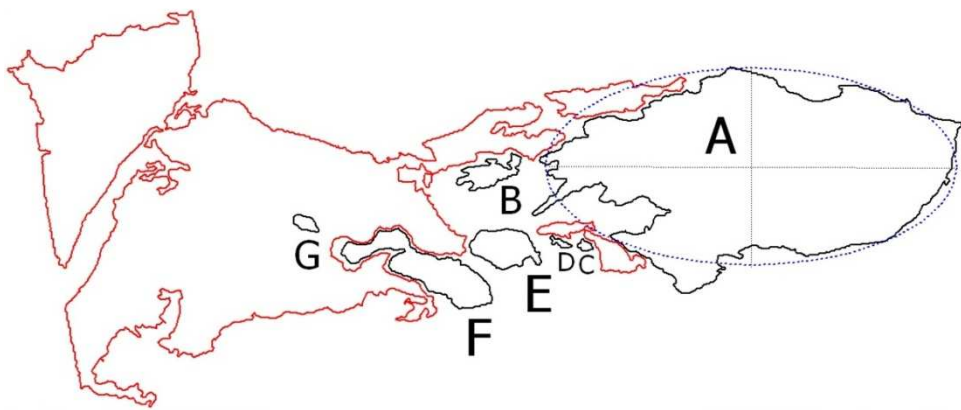


Figure 4.9 Hsiaolin Slide and its 7 subdivisions. The landslide is represented by an ellipse for the dimensions of width and length. Black lines are isopleths of -5 m and red lines are isopleths of +4m. Subdivision A is the major landslide body.

With 15 cross sections and fixed interval of 50 m between sections, the estimated volume using Method of Average Sections is 26,303,750 m³.

In Grid Method, The landslide volume is calculated by using 2010 DEM subtracted by 2005 DEM. In calculation, the failure surface was divided as 1 m² grid, and the negative value of grid subtraction represents the area that was eroded. Therefore, for the landslide, the summation of the negative value of every grid times the grid area is counted as the volume of landslide (Formula 4.3). Thus, With a grid of 1 m resolution, the estimated volume using Grid Method is 26,465,275 m³.

The results obviously show that the variation of the volumes given by Method of 3D Sections is larger than that of other two methods. Therefore, Grid Method would be more preferable due to it's easier in automation if high resolution DEM can be obtained from LiDAR surveys.

4.4.2 Namashia Case for Whole Area Volume Estimation and Power Law

The test site in Namashia District of Kaohsiung City (Figure 4.7) is used to demonstrate (1) The extraction of individual landslides from the overall landslide map; (2) Method of Accumulating Individuals; and (3) Derivation of the power law for the relationship between area and volume of the study area.

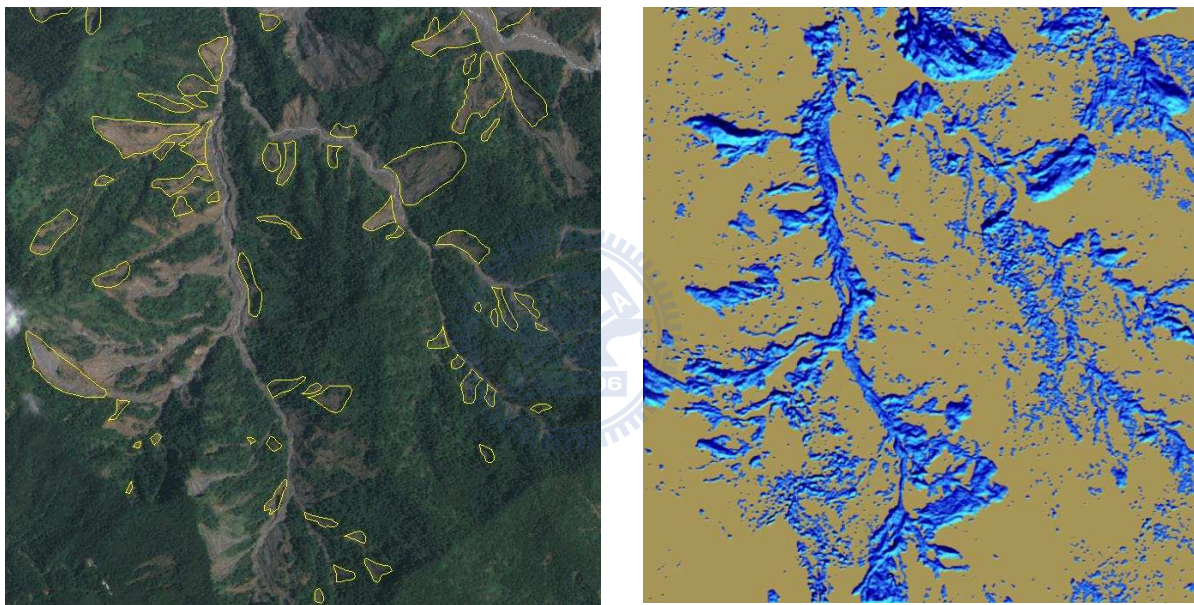
A 2D landslide map (Figure 4.10) has to be generated first. Then, extraction of individual landslides are made one by one from the 2D landslide map (Figure 4.11). Thus, the area and volume of each individual landslide can

thus be estimated. For the estimation of landslide volumes in a study area, the alternative for the Simple DoD Method is the Method of Accumulating Individuals which estimates the volume (V) by accumulating individual volume (v_i) of all landslides in the study area as shown in Formula 4.1.

To derive the regression relationship between A and V , Guzzetti et al. (2008&2012) tested different fitting techniques including least-square linear fit, robust linear fit, robust-resistant regression, and least-square, non-linear fit to account for problems associated with the fitting of log-transformed data spanning multiple orders of magnitude. Guzzetti et al. (2009) suggested robust-linear fitting (Venables and Ripley, 2002) for minimizing the effects of the outliers. This fitting method is also used for regression of the landslide volume V and landslide area A in this study, $V = kA^a$.

The result of the Ternbausan-One area with 50 landslides shows that $k = 0.099$, $a = 1.395$, and R-squared coefficient of determination = 83.7%. As shown in Figure 4.12, a dash line in the figure depict a separate study in the neighborhood using 488 points of landslides in a geological environment of well-cemented sandstone and shale, $k = 0.0146$, $a = 1.523$ (Tseng et al., 2011). Because of the geology in Ternbausan-One area is mainly composed of shale and silts, The surface materials of this area are more soft and weathered than those of the neighborhood area. Therefore, the power law gives a meaningful result that higher volume of deposits of unit area is generated in study area than that in the neighborhood area with, that is more sedimentation in this area than

the other area. It was also reported by Guzzetti et al. (2008) that $k = 0.0844$ and $a = 1.423$. These empirical formulas reflect different physiographic conditions including geology, soils, climate and denudation processes (Kalderon-Asael et al., 2008). It is concluded that further experiments can be applied with the methods proposed in this paper for the extraction of individual landslides from the overall landslide map and, subsequently, for the derivation of the relationship between landslide area and volume.



(A) Orthophoto

(B) DoD-shaded image

Figure 4.10 Interpretation of a 2D landslide map on basis of orthophoto and DoD-shaded images

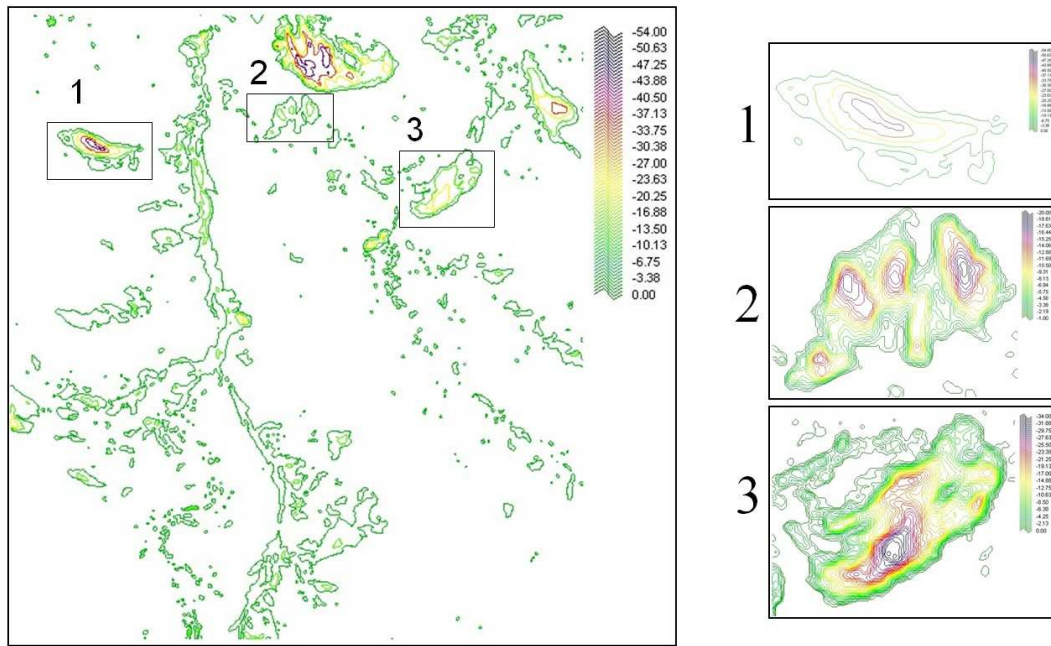


Figure 4.11 Extraction of individual landslides are made one by one from the whole landslide map

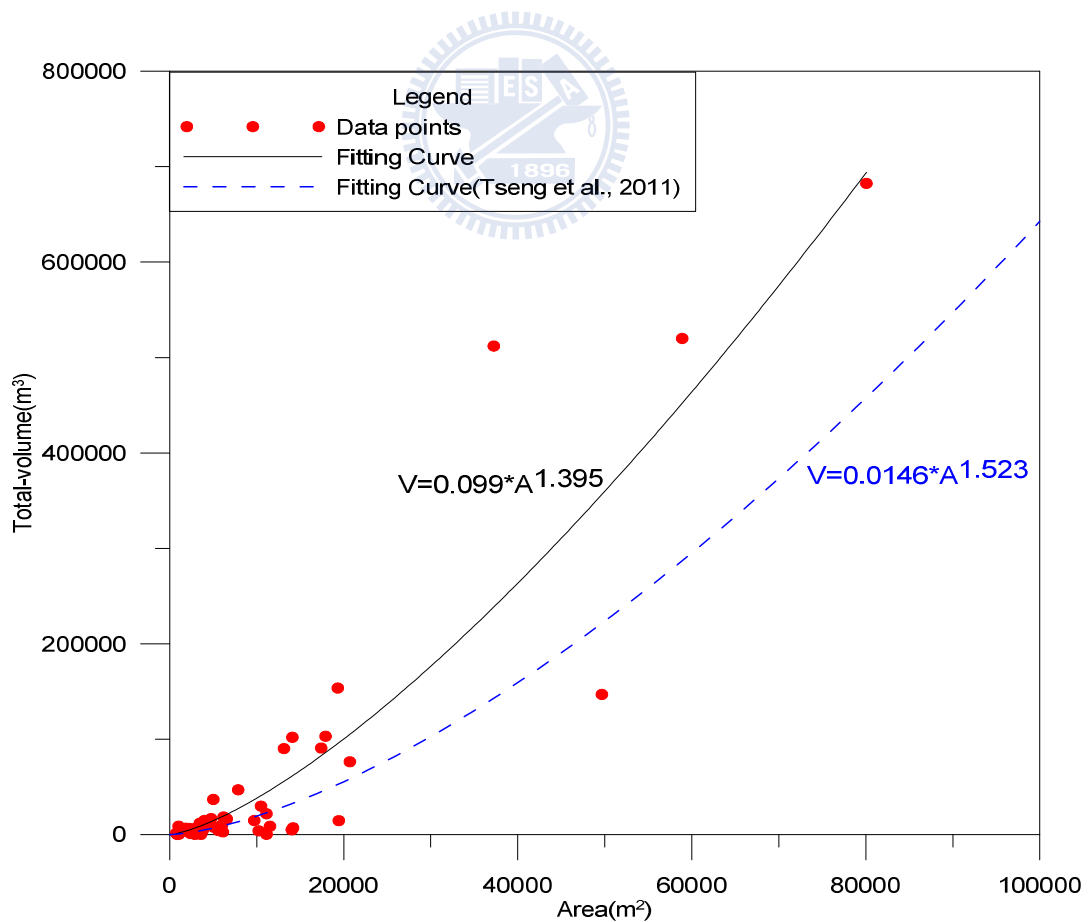


Figure 4.12 Empirical formula of landslide area A (m^2) and volume V (m^3) of the data points of landslides in the study area, $V=kA^a$.

Chapter 5 Landslide Extraction with a Geomorphological Model

In this chapter, methods and experiments are made for establishing a geomorphological model for extracting landslides using multi-temporal LiDAR data.

5.1 Introduction

As stated in the motivation of this dissertation in chapter 2, landslides is one of the most frequent natural disasters in Taiwan as well as in the world. In addition, high resolution LiDAR-derived products allow more accurate landslide modelling by improving their geometrical characterization. Expert knowledge of the geomorphometric properties of landslides may be required to establish an automatic interpretation method. High resolution and high accuracy LiDAR DEM and DSM and orthophotos are now basic constituents of NSDI in Taiwan (Liu and Fei, 2011). Therefore, it is high time to further apply geomorphometry in active landslide study (Liu et al., 2009).

A geomorphometric model is urgently needed for disaster management. Therefore, the purpose of this study is to develop a geomorphometric model based on highly accurate and high resolution LiDAR topographic data with

parameters calibrated by optimized thresholds (SWCB, 2010). The demonstration case in this study was located in southern Taiwan near Hsiaolin village, the village destroyed by Typhoon Morakot. The landslide type which can be detected by this model is a shallow landslide (Liu et al., 2009).

5.2 Study Area and Materials

Materials for this research include high resolution satellite images and airborne LiDAR data.

5.2.1 Physiographic Settings of the Study Area

Hsiaolin village is located in Chiahsien District, Kaohsiung City (Figure 5.1). The study area is covered by 9 map-sheets of 1/5000 national photomaps: 95193025~95193027; 95193035~95193037, and 95193045~95193047. The village is located on a river terrace of Chisan River. The geological map in Figure 5.2 (Song et al., 2000) shows that the area is situated in the Western Foothill Zone of Miocene sedimentary formations including Changchikeng Formation, Tangenshan Sandstone, Yenshuikeng Shale, and Peliao Shale. The area is primarily covered by Tangenshan Sandstone and Yenshuikeng Shale. Tangenshan Sandstone consists of alternate layers of sandstone and shale, whereas Yenshuikeng Shale consists of alternations of siltstone and shale with occasional lens-type conglomerates. The river terrace materials include recent fluvial and colluvial deposits of sand and gravel.



Figure 5.1 SPOT image taken on 2009/08/24 after Typhoon Morakot. The 8-digit numbers are the map numbers of national 1/5000 map series.

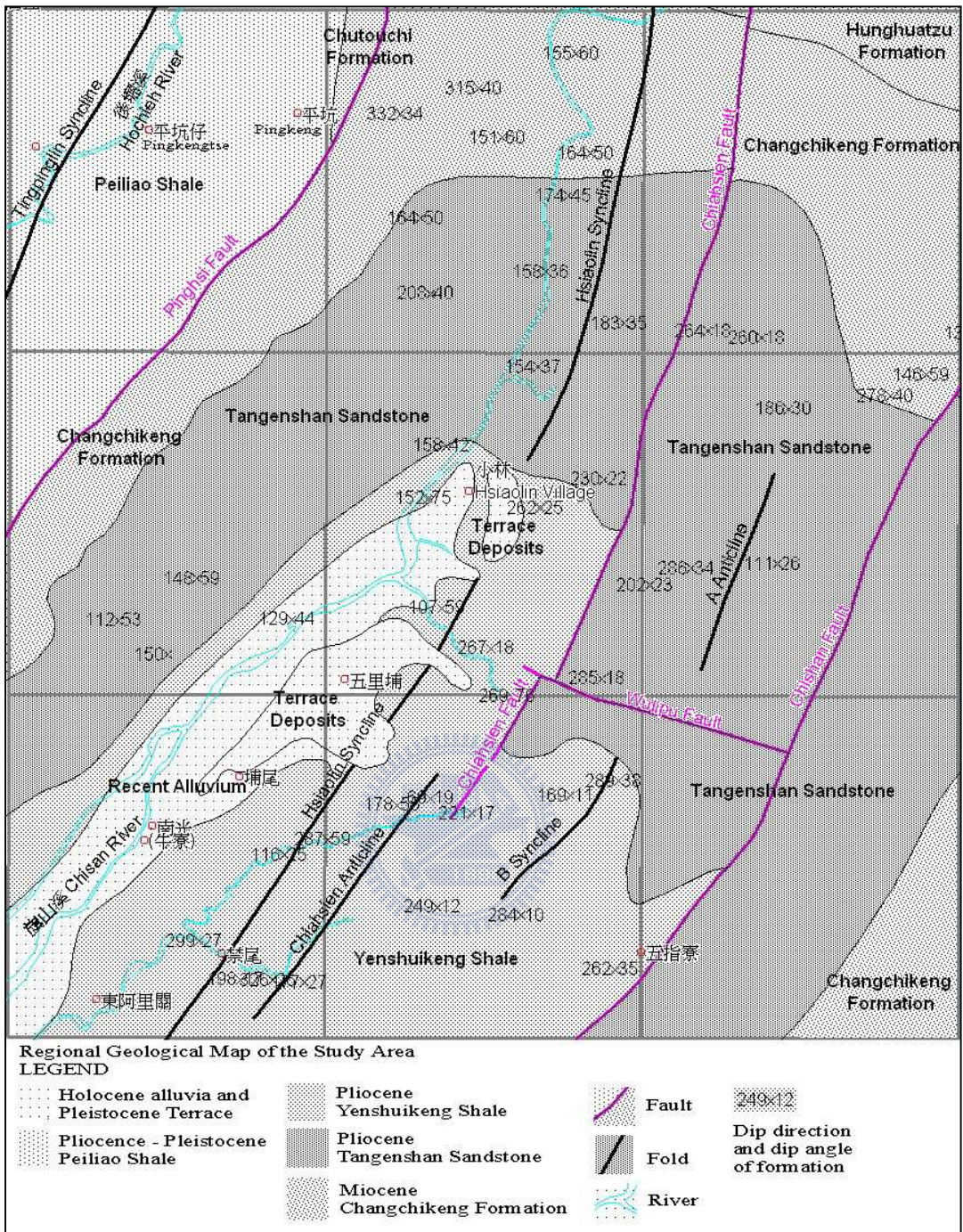


Figure 5.2 A regional geological map near the Hsiaolin village (Song et al., 2000).

5.2.2 Satellite images

This study uses SPOT images taken at approximately the same season as the

first LiDAR survey in 2005 used for comparison. The Formosat-2 image taken after Typhoon Morakot was collected and compared with the second LiDAR survey in 2010. In addition, there are several typhoon events from 2007 to 2009. Therefore, this study also uses SPOT images acquired from 2005 to 2009 (Figure 5.3) to analyze landslide recurrence rate. The resolution of enhanced-mode SPOT images is 2.5 m, pan-sharpened Formosat-2 image have a resolution of 2.0 m.

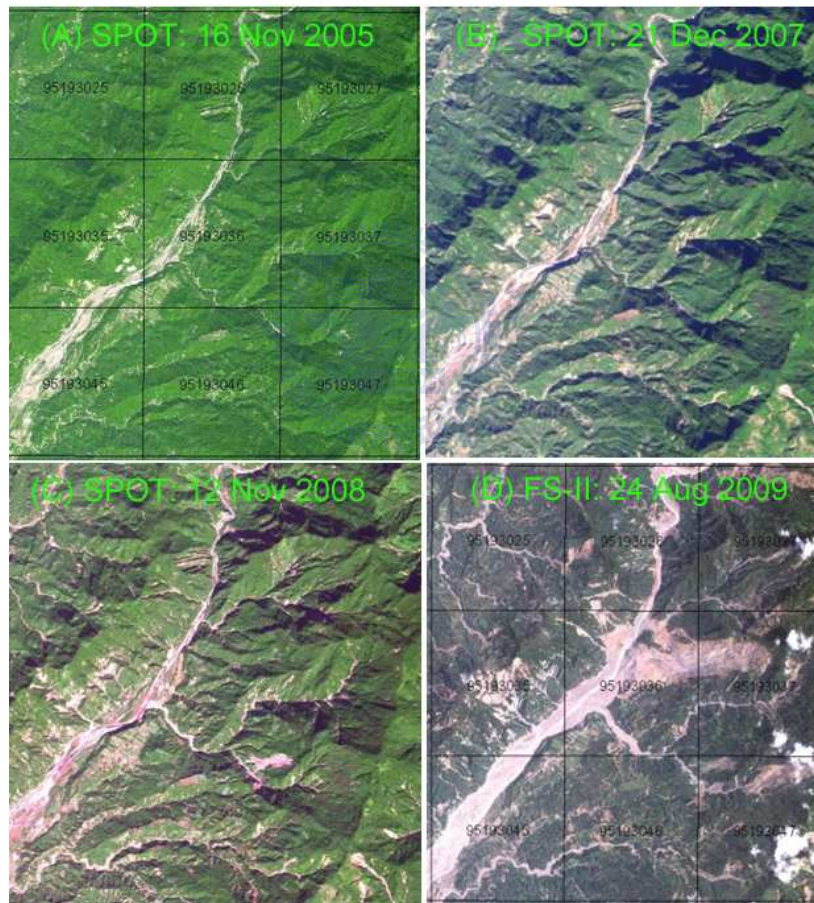


Figure 5.3 Satellite images of the study area from 2005 to 2009. Bright grey features on the images are mostly landslide scars. Landslide occurrence increasingly increases in this period of time, as shown in Figure 5.8

5.2.3 Airborne LiDAR data

LiDAR data before and after Typhoon Morakot were collected for this study. The LiDAR feature of multiple returns provides a good means for editing the point clouds and produce DSM, DEM, and CHM (Canopy Height Model) or DBM (Digital Building Model). This in turn enables the analysis of multi-temporal datasets. As Figure 5.4 shows, the DEM and DSM in this study are based on 2005 LiDAR survey. The landscape suffered from dramatic changes after Typhoon Morakot (Figure 5.5). The large landslide near Hsiaolin Village is the most conspicuous example. Figure 5.6 shows the DEM and DSM of the study area acquired in 2009 after Typhoon Morakot. Both of the LiDAR datasets in this study were surveyed using a common guideline (MOI, 2006) and a common datum—TWD97 for geodetic coordinates and TWV2001 for vertical system—to maintain the same level of accuracy. The RMSE (Root mean square error) was 16.7 cm with a standard deviation of 16.3 cm for 2005 LiDAR data. The RMSE was 20.2 cm with a standard deviation of 18.3 cm for 2009 LiDAR data. RMSE is a measure of the dispersion between the coordinates obtained by Airborne LiDAR and those surveyed in the field. Whereas, standard deviation is a measure for the concentration of the differences between these two datasets. The accuracy of these two datasets meets the requirement set in the MOI guideline (MOI, 2006).

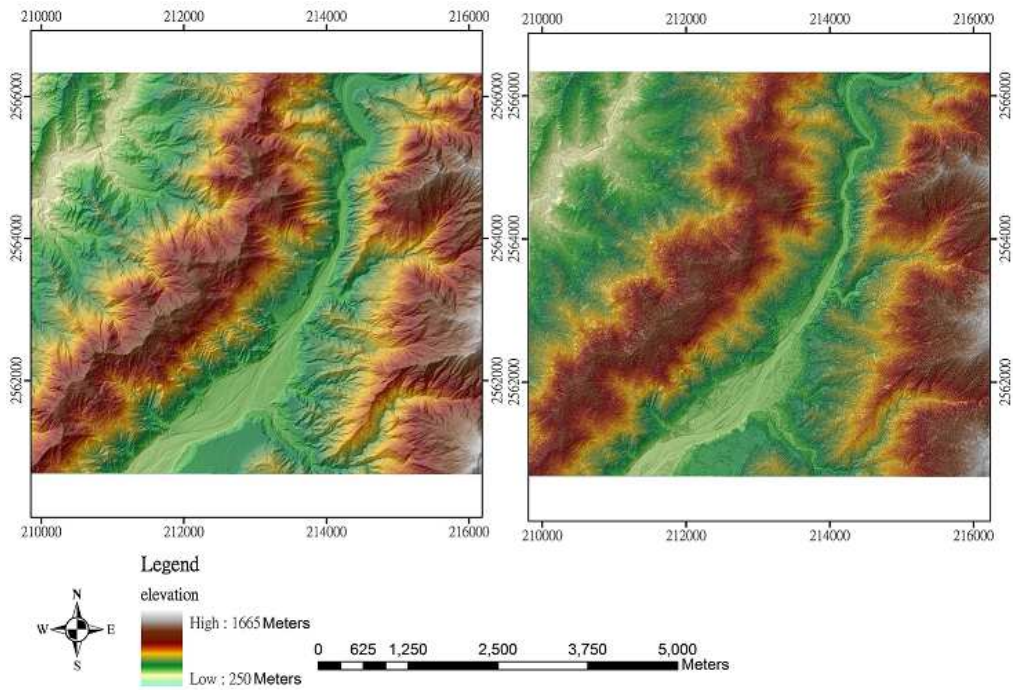


Figure 5.4 DEM and DSM images before Typhoon Morakot



Figure 5.5 3D perspective views of Hsiaolin Village before and after Typhoon Morakot. Hsiaolin Landslide has a volume of ~25 million cubic meters with a maximum depth of 85 m on top area and a maximum length of 3396 m from top to the other side of Chisan River. The landslide completely destroyed the village.

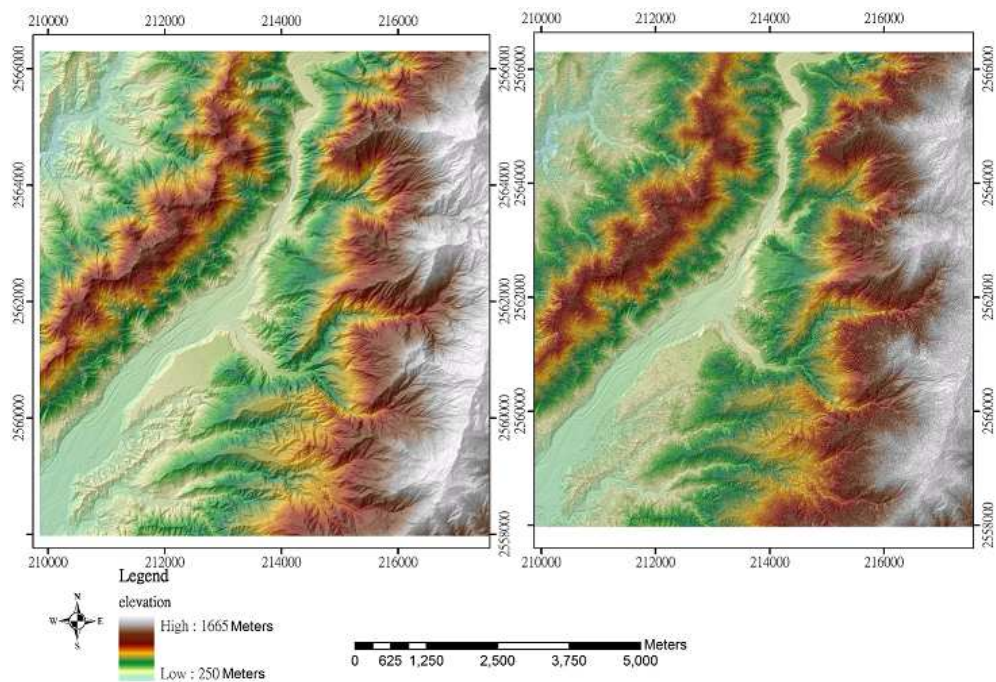


Figure 5.6 DEM and DSM obtained after Typhoon Morakot. As compared to those of Figure 5.4, dramatic landform change can be found in river valley as well as mountain slopes, especially the example of Hsiaolin Landslide.

5.3 The Geomorphological Model for Landslide Extraction

5.3.1 Introduction

The proposed model includes both global and local detection procedures, and uses a supervised classification method for global landslide detection. The focus of this paper is on global detection. Because of the diversity of the geologic and topographic environments in which landslides occur, omission and commission errors are unavoidable when using the global approach. Thus, local landslide detection is required to increase the accuracy of the resulting landslide

map (Liu et al., 2009). With the attendance of geological expert, the local approach employs several interactive manual editing tools to compile landslide information and minimize commission and omission errors. Therefore, the aim of the global detection is to include as much as possible the areas which are vulnerable to landslides. For error analysis, the user accuracy, producer accuracy, average accuracy, and overall accuracy were calculated from a confusion matrix (Kohavi and Provost, 1998).

Figure 5.7 shows the flowchart of the geomorphometric model established in this study. Landslide areas possess geomorphometric characteristics that can be used to establish a geomorphometric model to describe the topographic feature of landslides. As the first step, global parameters based on landslides extracted from satellite images by classifying bare land and then filtering out commission errors produced by bare agriculture lands and debris flows were obtained. Landslide polygons were then overlaid on parametric maps derived from 2005 LiDAR data. The parametric parameters of the extracted samples were then used as training sample globally. Thresholds of various parameters were derived based on statistics of the training samples of landslides. Threshold values of the six geomorphometric parameters (T1~T6) were defined a priori based on some user-defined training areas, that is, the landslide polygons. The mean and standard deviation values of each index were calculated and the threshold values were set to be the mean \pm 3 standard deviations. The proposed method classifies a pixel as a landslide pixel if the following expression is true:

$(\text{Slope} > T1) \cap (\text{Roughness} < T2) \cap (\text{Curvature} > T3) \cap (\text{OHM} < T4) \cap (\text{Greenness} < T5) \cap (\text{Wetness} > T6)$. Otherwise, it is classified as a non-landslide pixel. Because the global landslide detection algorithm is pixel based, isolated landslide pixels were removed by morphological filtering (e.g., opening and closing). Small landslides were eliminated by setting a minimum mapping unit. Finally, the detected landslide pixels were converted into vector-based polygons. In other words, the pixel conforms to the threshold criterion is designated as 1, otherwise it is designated as 0. The area of the intersecting set of all the parameters was categorized as landslide area. This is a dichotomic multi-criteria evaluation approach.

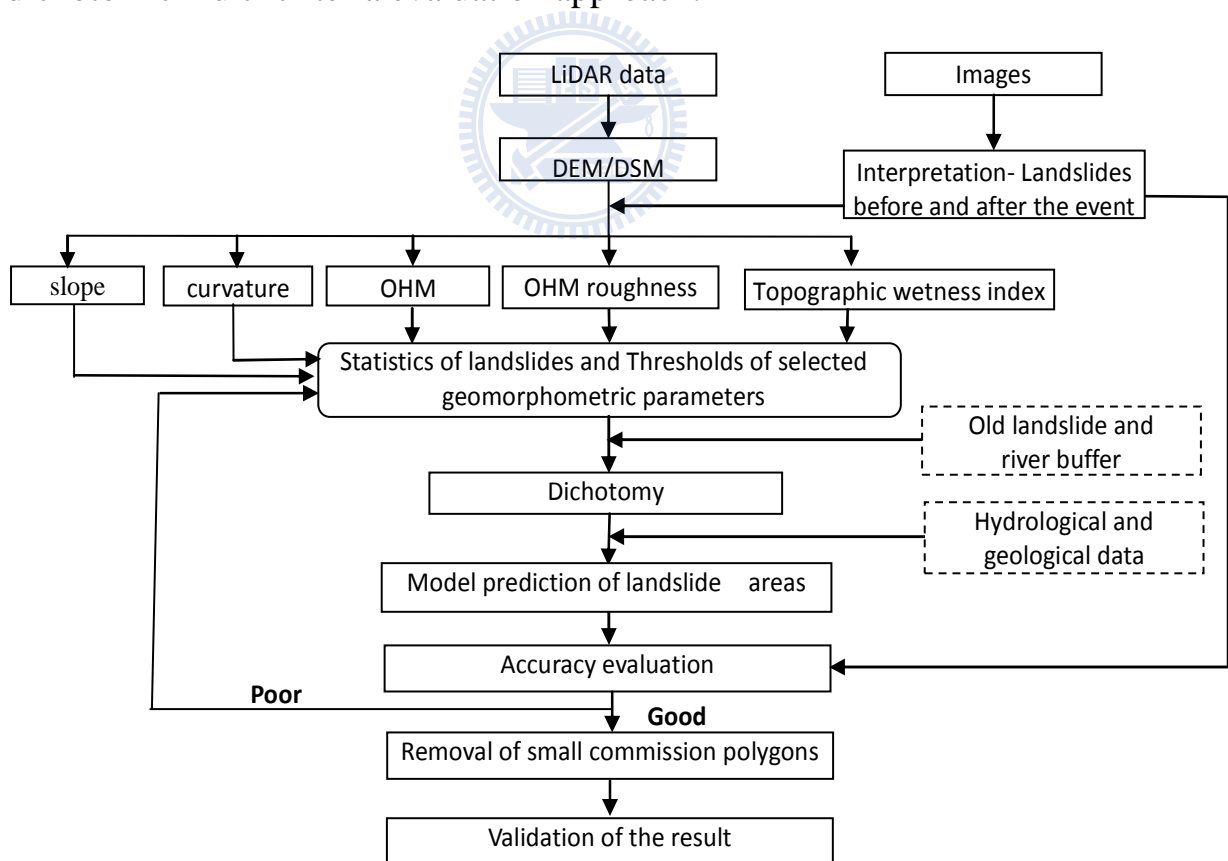


Figure 5.7 Flowchart of the geomorphometric model

5.3.2 Geomorphometric Parameters of Landslides

For extracting landslides from high accuracy and high resolution LiDAR data, parameters for establishing the model were selected based on the criteria usually used in manual interpretation of landslides, including the 2D and 3D landslide features detailed previously in Table 3.1. The parameters of the geomorphometric model in this study were derived from LiDAR DEM and DSM. The major parameters in this model include slope, surface curvature, OHM (object height model), OHM roughness, and topographic wetness index. In addition, NDVI (Normalized Difference Vegetation Index) or greenness is one of the most important indexes for landslide recognition due to that fresh shallow-seated landslides are characterized by bare land without or with little vegetation cover. Therefore, it is also included in the model. A number of vegetation indices, such as the NDVI (Jackson et al., 1983), EVI (Enhanced Vegetation Index) (Liu and Huete, 1995), and LAI (Leaf Area Index) (Chen and Black, 1992) have been used in remote sensing for analyzing vegetation cover. Of these indices, NDVI is the standard method for comparing relative biomass and vegetation greenness in remotely sensed images. A higher NDVI indicates a higher level of healthy vegetation cover. The greenness index is similar to the NDVI, except that it substitutes a green band for the near-infrared band.

These parameters are also closely related to the factors for landslide susceptibility (Tarolli et al., 2011). The control factors of slope stability usually include slope angle, strength of materials, and pore water pressure (Turner and

Schuster, 1996). If the slope gradient is high, the slope can be unstable. Slope angle was thus selected as the first parameter because of its importance, and can be easily derived from DEM. Because DEM represents the bare ground surface and DSM represents the upper envelope of all the objects above the bare ground surface, the difference between these two well-defined surfaces is minimal in the area of rainfall-induced landslide. In this case, the OHM, defined as the difference between these two surfaces, can be a good parameter for automatic landslide recognition. After wash out or sliding, the surface of landslides in nature should be smoother than the surroundings. Surface roughness is an objective and useful measurement of landslide topography (Glenn et al., 2006; Woodcock, 1977; Mckean and Roering, 2004). Landform curvature is another critical factor controlling the susceptibility of landslide occurrence (Pirotti and Tarolli, 2010).

The definition of the parameters is as follows (Wilson and Gallant, 2000; Zhou and Liu, 2006):

(1) Slope. The slope angle of a landslide is the angle between the horizontal surface and the ground surface of the longitudinal axis of the landslide. The slope angle for each landslide can be derived from LiDAR DEM data. A variety of methods are available for terrain slope gradient estimation. However, the details of a high-resolution terrain model may introduce high variations in changes of local slope gradients (Sharpnack and Akin, 1969). This study adopts the method proposed by Parker (1997) to overcome this problem, that is

the derivatives of the Gaussian function are convoluted with the DEM in the x and y directions, respectively, and then combined to estimate the slope.

(2) OHM. Object height models (i.e., OHMs) are obtained by subtracting DSM from DEM to describe the height of objects above bare ground. The OHM describes the heights of above-ground objects in raster format. Objects close to zero in height may represent the bare soil that characterizes landslides.

(3) OHM Roughness. Roughness is a derivative of OHM, defined as one standard deviation in a 5 x 5 moving window. This measure, which is a function of geological structure and lithology, describes the relief variation in the local area. Because most landslides occur in bare soil areas, the surface is smoother than that of forested areas. Thus, a surface roughness index can be used to detect landslide areas. To account for the high terrain variation in mountainous areas, this study uses object heights rather than surface heights. For simplicity, the standard deviation of object heights within a local window serves as the surface roughness index.

(4) Curvature. Curvature is the second derivative of the surface (Schmidt et al., 2003). Two optional output curvature types are possible: the profile curvature is in the direction of the maximum slope, and the plan curvature is perpendicular to the direction of the maximum slope. The curvature is the slope form and has a significant effect on surface runoff, soil erosion, and deposition processes (Stefano et al., 2000). This study applies a 15 x 15 medium filter to the DEM to suppress any accidental height changes in the high resolution elevation model.

The curvature along the slope direction was then calculated with a 5 x 5 mask.

(5) Topographic wetness index (TWI). Wetness is derived from the concentration of a small watershed (Kirkby, 1975; Wilson and Gallant, 2000). Topography is often one of the major controls of the spatial pattern in saturated areas, which in turn is a key to understanding the variability of hydrological processes. The topographic wetness index has become a widely-used tool to describe wetness conditions. The formula is as follows:

$$\omega = \ln\left(\frac{A}{\tan \theta}\right) \quad (5.1)$$

where A is the local upslope contributing area and θ is local slope.

(6) NDVI or greenness. This parameter is derived from satellite images or orthophotos acquired at a compatible time as the LiDAR survey. In other words, there are no rainfall events between the time that both the LiDAR data and the images or orthophotos are acquired. Because rainfall-induced landslides of natural slopes are mostly covered by densely-vegetated surroundings, the vegetation index is critical for indicating the areas of bareness. The most popular index is the NDVI:

$$\text{NDVI} = (\text{NIR}-\text{R})/(\text{NIR}+\text{R}) \quad (5.2)$$

where R stands for the grey value of the red band and NIR stands for grey value of the near infrared band. Theoretically, if the image digital values are calibrated to stand for the reflectance of the target, the NDVI can be widely

applicable. However, the digital numbers of the red band and NIR band of digital aerial cameras are not calibrated for this purpose. Therefore, the NDVI value is a relative indicator of vegetation cover. NDVI can be applied to modern digital aerial cameras, which usually include an NIR band. If color aerial photographs include only RGB bands, an alternative greenness parameter can be used. Greenness is also a relative indicator with radiometric values that are not normalized:

$$\text{Greenness}=(G-R)/(G+R) \quad (5.3)$$

where G is the grey value of the green band, and R is the grey value of the red band. The values of NDVI and Greenness range from -1 to 1. Nevertheless, the range for these values in landslides may change depending on natural weather, terrain conditions and type, and camera sensor settings. A relatively low value implies that the area of the pixel is low vegetated or bare.

5.4 Results and Discussion

5.4.1 Establishing The Geomorphometric Model of Landslides

Bare land has a relatively low reflectance in the infrared region of the electromagnetic spectrum. This feature can be used in unsupervised classification to obtain a preliminary map of landslides. On an interactive screen, manual editing of the results can filter out commission errors such as bare crop fields and debris flows. Figure 5.8(A)-(D) show the distribution of landslides over four different years. Six typhoons affected Taiwan in 2008: Kalmaegi,

Fung-wong, Nuri, Sinlaku, Hagupit, and Jangmi. A comparison of the images in 2007 and 2008 reveals more landslides in 2008 (Figure 5.8E). The number of landslides increased substantially after the torrential rainfall of Typhoon Morakot (Figure 5.8F).

The recurrence rate of landslides, defined as the repetitive occurrence of landslides between two different times, was 65% between 2007 and 2008. The recurrent rate was even as high as 95.9% between 2009 and 2008. 64.1% of the landslides in 2008 reappeared in 2009 after Typhoon Morakot. The high recurrence rate between succeeding years shows that landslides happen in similar environmental conditions. To verify the accuracy of the landslides obtained by satellite images, conventional aerial photo-interpretation was conducted. It is shown that the overall accuracy was 92.4% with omission error of 9.2% and commission error of 16.1%.

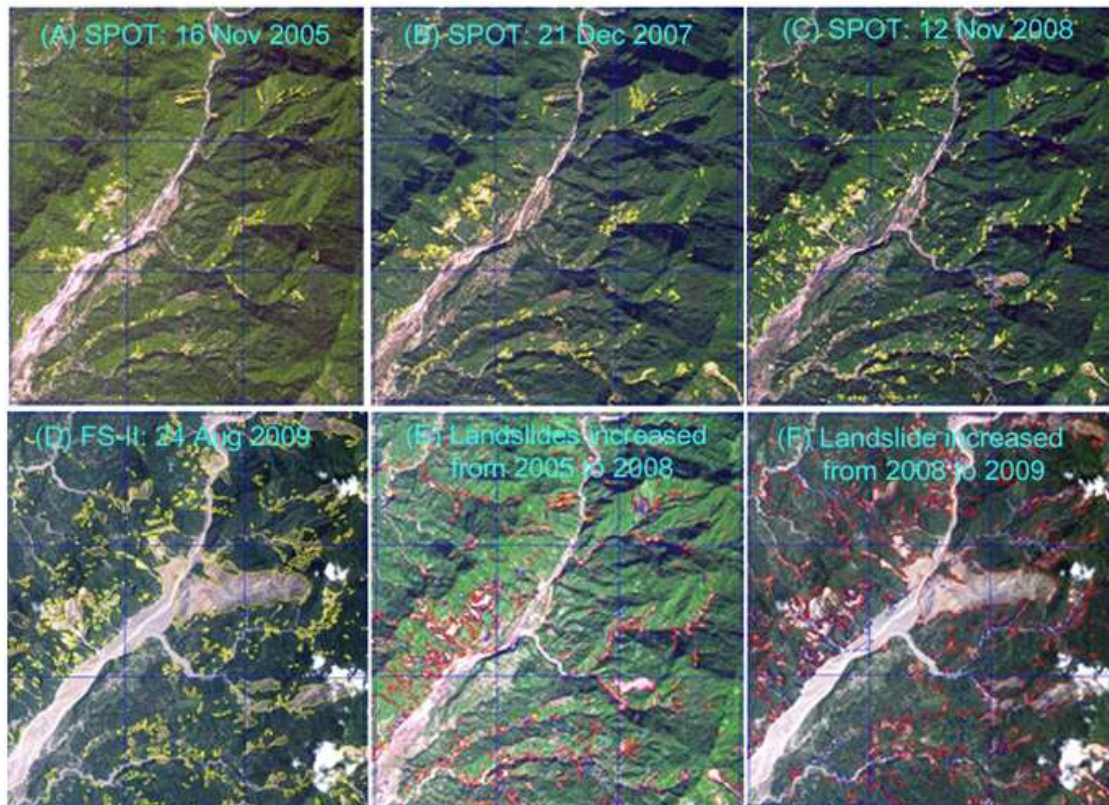


Figure 5.8 Landslide distribution between 2005 and 2009. Landslides on images are high-lighted with yellow polylines. New landslides are in red polylines when comparing images taken in 2005 and 2008 (E) and those in 2008 and 2009, respectively.

5.4.2 Statistics of Geomorphometric Parameters

Figures 5.4 and 5.6 are the primary data of DEM and DSM obtained in 2005 and 2009, respectively. For further understanding the features of landforms, geomorphometric parameters are extracted from these primary datasets. Figure 5.9 shows the distributions of major LiDAR-derived geomorphometric parameters selected for landslide recognition in this study.

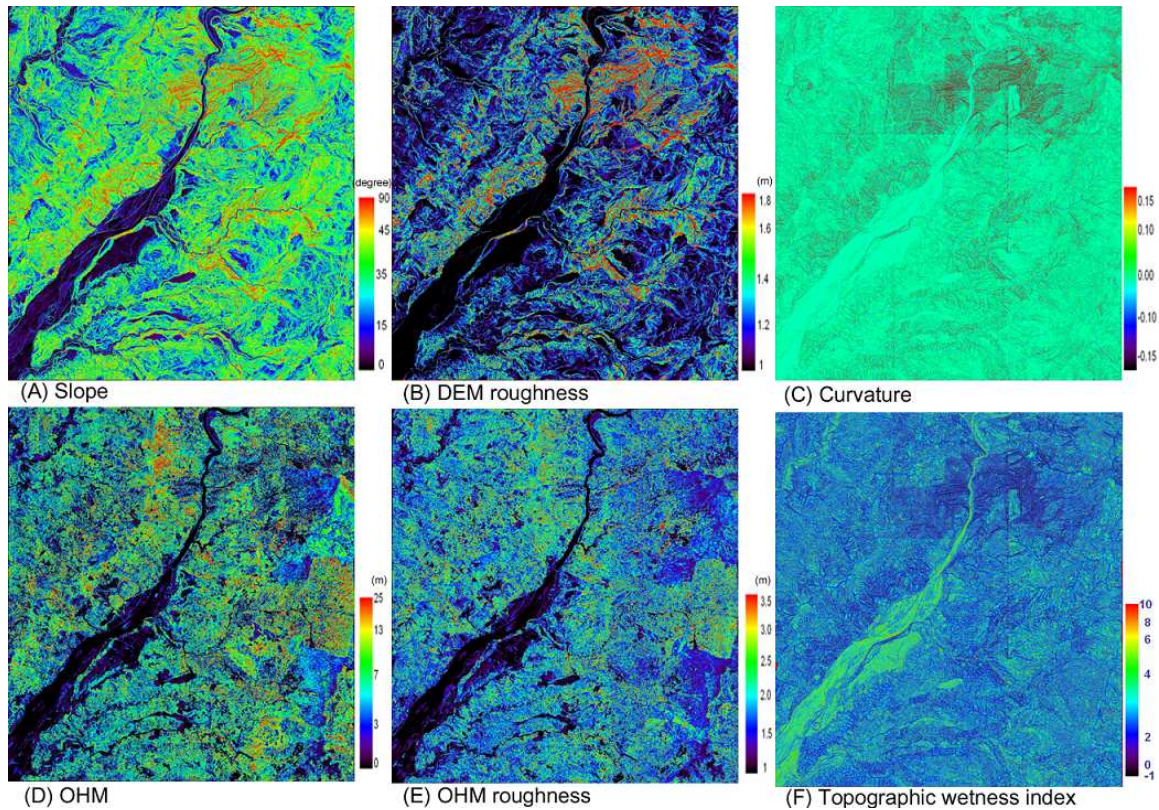


Figure 5.9 The distributions of major LiDAR-derived geomorphometric parameters selected for landslide recognition in this study. The coordinates of the maps are (209810 , 2566339) and (217609 , 2557916) for the lower right and upper left, respectively.

Figure 5.10 shows the frequency distribution of geomorphometric parameters based on 2005 landslide data. Figure 5.11 shows the frequency distribution of these parameters based on 2009 landslide data. The average slope of landslides in 2005 is 31.2 degrees. The surface roughness is generally below 1.5 m, with a cumulative fraction of 90% below 1.5 m (Figure 5.10B). On basis of the OHM derived from the difference of DSM and DEM, the average OHM is 9.1m with 20% and 30% of all the landslide pixels having a value below 0.5 m and 3.3 m,

respectively. Figure 5.10D is a frequency distribution of OHM. The major fraction of OHM is distributed between 5 m to 20 m. A cumulative fraction is 37% and 92% for OHM under 5 m and 20 m, respectively. Only 8% of OHM exceeds 20 m, indicating commission errors of trees can be as high as 8%.

Figure 5.11 shows the frequency distribution of geomorphometric parameters based on 2009 landslide data obtained from images after Typhoon Morakot. In other words, the training samples of the geomorphometric parameters are obtained from the LiDAR data taken in 2009. The average slope of the landslide areas is 33.8 degrees, with a major range in 25~50 degrees. A cumulative fraction is 25% and 90% for slope under 25 and 50 degrees, respectively. The average roughness is 1.2 m, with 90% less than 1.5 m. The average curvature is -0.008, showing that most of the slope forms are more concave than convex. The OHM ranges from 5~20 m with an average of 9.1 m. Similarly, there are 30% of the landslide pixels having an OHM less than 3.3 m. The average roughness of OHM is 2.6 m, with a standard deviation of 1.2 m.

The frequency distributions of various parameters derived by landslides in 2005 and 2009 show no obvious differences. In both cases, the average slopes fall within the range of 30~50 degrees, with a roughness of 1.1~1.7 m, curvature of -0.04~-0.02, OHM under 17 m, and OHM roughness of 1.5~3.5 m.

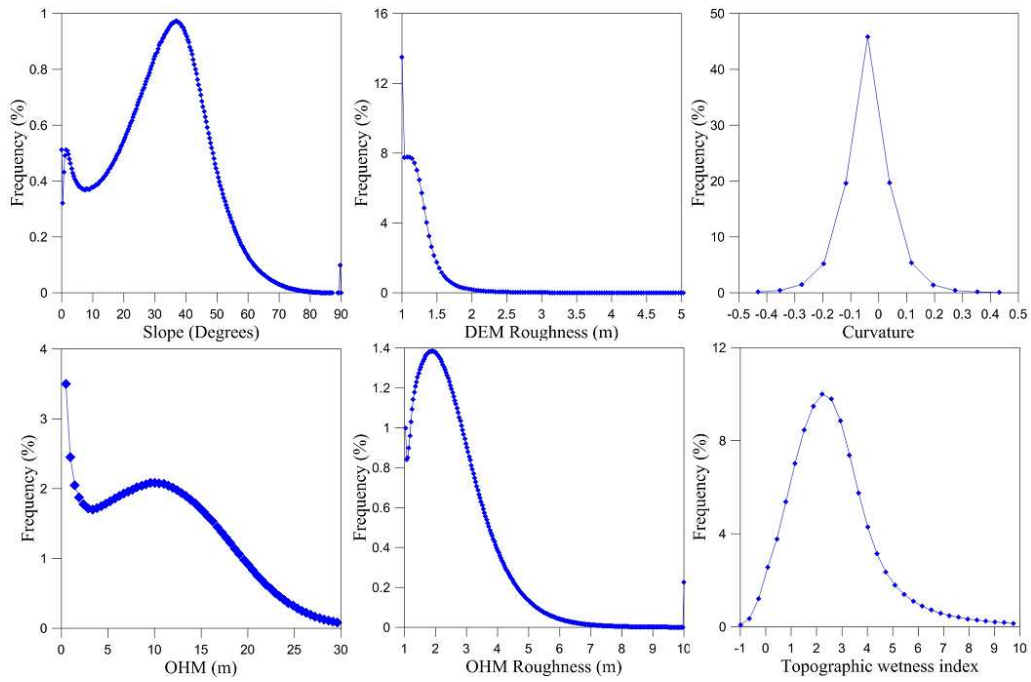


Figure 5.10 Frequency distribution of geomorphologic parameters of landslides

in 2005.

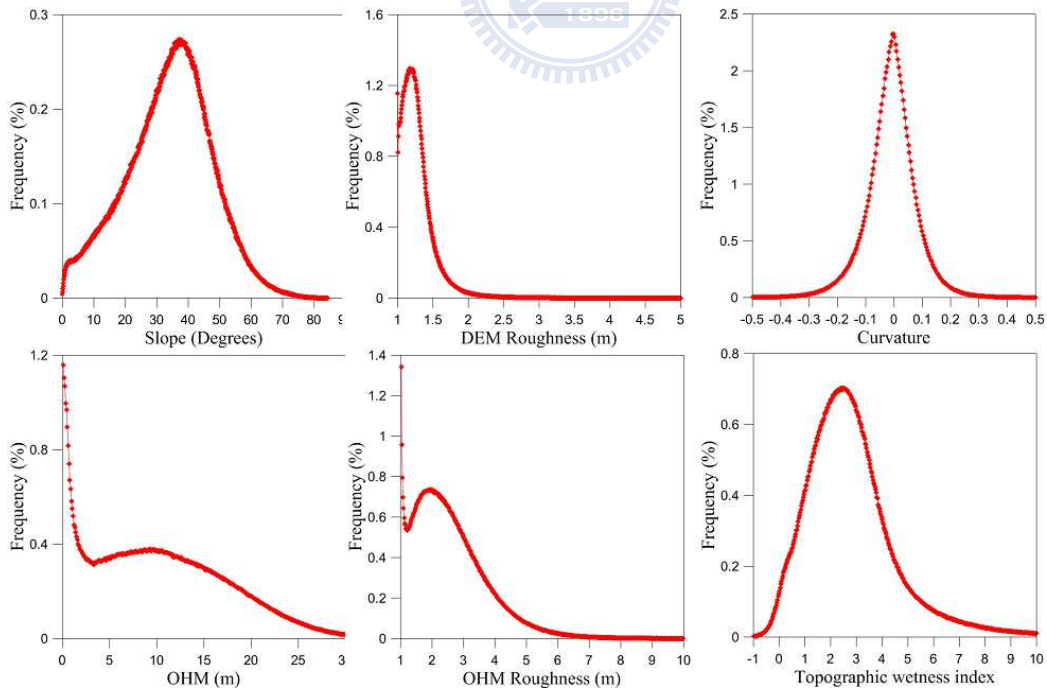


Figure 5.11 Frequency distribution of geomorphologic parameters of landslides

in 2009.

When using the landslides in 2008 for training samples, the slope ranges from 25~55 degrees, with an average of 38.2 degrees. As a comparison, the general average slope for 2009 landslides is 33.8 degrees, with an OHM of less than 20 m, roughness less than 1.5 m, and average curvature of -0.018. More concave slope forms were present in 2008 than in 2009. Before the Morakot landslide event, the average OHM was 7.3 m, and the average roughness was 2.4 m with a standard deviation of 1.2 m.

The average slopes of 2008 landslides are higher than those of 2009 landslides. However, the curvature for 2008 is less than that for 2009. There are no obvious differences in OHM and roughness. In 2008, a total of 60% of the landslides have an area of less than 0.5 hectares, whereas the average area of individual landslides in 2009 become larger, with 73% of them possessing an area of less than 1.0 hectare.

5.4.3 Verification of the Geomorphometric Model

By comparing the spatial distribution of landslides in 2005 and 2009, this study shows that the recurrent rate is as high as 55%. It is therefore reasonable to suppose there is a higher susceptibility in the buffer zone of old landslides. River bank erosion is another important trigger factor for river bank landslides, and upstream erosion has the same effect. Therefore, the proposed model includes buffer zones for river bank and upstream areas. In addition to six

geomorphometric parameters, the model includes buffer zones of old landslides and river banks and up-streams.

A sensitivity analysis of the different combinations of thresholds was conducted to find out the optimum combination of thresholds. Tries with major ranges of each parameters have been tested (Table 5.1). The final optimized results show that the overall accuracy obtained in this study is 68.2%, where the user accuracy is 42.6% and the omission error is 57.4%. Because spatial resolution of DEM and DSM is 1 m, slivers or dispersed isolated small patches of landslides generated when grids are transformed into vectors can be treated as noise. In this study, polygons with an area smaller than 50 square meters are filtered out and manually edited to delete some commission errors, improving the accuracy of the final result. Figures 5.12(A) and 5.12(B) are examples of the modeled results of landslides in 2008 and 2009, respectively. After manual editing, Tables 5.2 and 5.3 show that the average accuracies in 2008 and 2009 are 76.6% and 72.5%, respectively. Because landslides only covers small fraction of the study area, the result detected by the model with loose criteria set for the parameter thresholds can be prone to commission errors. This leads to user accuracy as low as 5.0% and 20.2% for 2008 and 2009, respectively. For conservation purposes, commissions cause no big problems, whereas omission errors overlook hazardous areas. Therefore, this model remains meaningful though further effort is required to filter the commission errors.

Table 5.1. Tries of different combinations of thresholds for model parameters

tries	slope (degree)	DEM roughness (m)	curvature	OHM (m)	OHM roughness (m)	Wetness	Overall accuracy (%)	Producer accuracy (%)	Omission error (%)	User accuracy (%)	Commission error (%)
1	>22	<1.8	>-0.15	<25	<4.5	>0.5	53.59	15.67	84.33	56.45	43.55
2	>23	<1.8	>-0.15	<25	<4.5	>0.5	53.81	15.68	84.33	56.1	43.89
3	>24	<1.8	>-0.15	<25	<4.5	>0.5	54.22	15.68	84.32	55.46	44.54
4	>25	<1.8	>-0.15	<25	<4.5	>0.5	54.72	15.75	84.25	54.93	45.07
5	>22	<1.7	>-0.15	<25	<4.5	>0.5	54.95	15.76	84.24	54.58	45.42
6	>23	<1.7	>-0.15	<25	<4.5	>0.5	55.35	15.77	84.23	53.94	46.06
7	>24	<1.7	>-0.15	<25	<4.5	>0.5	55.91	15.84	84.16	53.31	46.68
8	>25	<1.7	>-0.15	<25	<4.5	>0.5	56.14	15.84	84.16	52.97	47.03
9	>22	<1.6	>-0.15	<25	<4.5	>0.5	56.55	15.86	84.16	52.32	47.68
10	>23	<1.6	>-0.15	<25	<4.5	>0.5	57.16	15.93	84.07	51.61	48.39
11	>24	<1.6	>-0.15	<25	<4.5	>0.5	57.09	15.74	84.06	51.26	48.74
12	>25	<1.6	>-0.15	<25	<4.5	>0.5	57.8	15.76	84.04	50.62	49.28
13

Table 5.2. Model accuracy for 2008 training samples in polygons

Category	Landslides (hectare)	Non-landslides (hectare)	Producer accuracy (%)	Overall accuracy: 76.61% Average accuracy: 51.47%
Landslides	75.54	1,430.51	5.02	
Non-landslides	105.88	4,957.16	97.91	
User accuracy (%)	41.64	77.61		

Table 5.3. Model accuracy for 2009 training samples in polygons

Category	Landslides (hectare)	Non-landslides (hectare)	Producer accuracy (%)	Overall accuracy: 72.51% Average accuracy: 54.19%
Landslides	317.18	1,245.36	20.3	
Non-landslides	560.31	4,446.24	88.7	
User accuracy (%)	36.15	78.12		

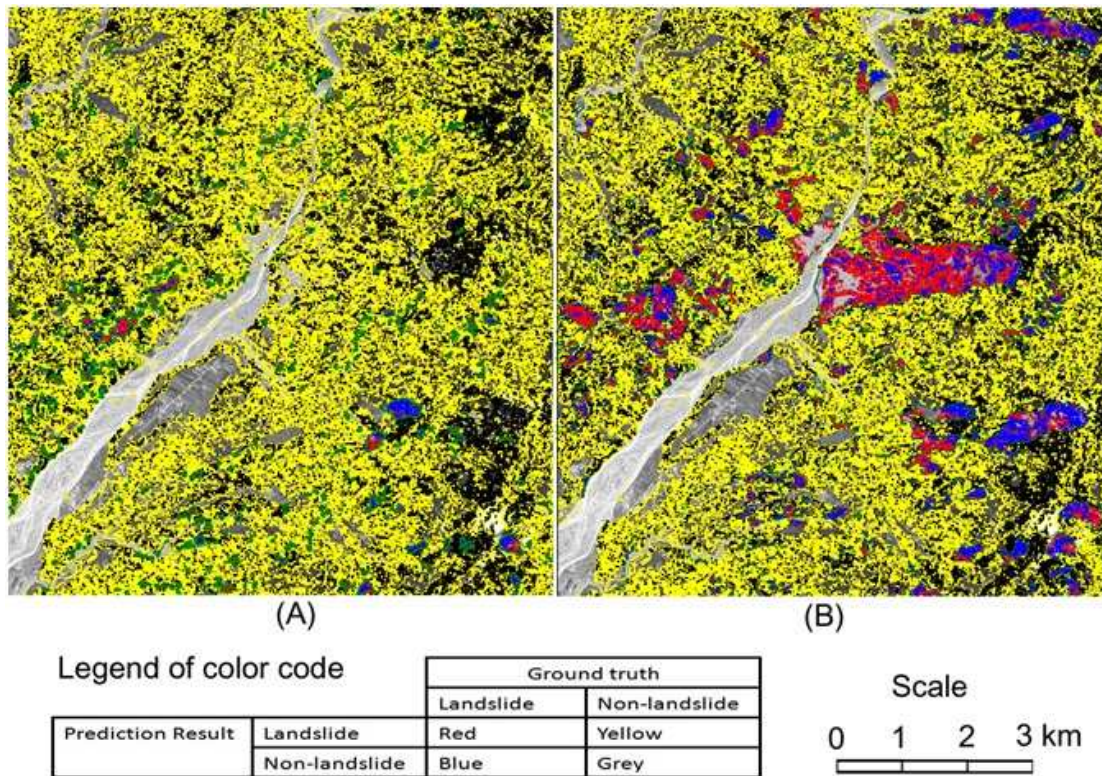


Figure 5.12 Landslide prediction with geomorphometric model: (A) Prediction of 2008 landslide susceptibility based on 2005 landslides in vector segments. (B) Prediction of 2009 landslide susceptibility based on 2005 landslides in vector segments.

5.5 Summary of establishing the geomorphologic model

Both of the LiDAR datasets used in this study, including the one obtained from the Ministry of the Interior in 2005 and the one obtained from July 23, 2010, to July 28, 2010, were manually edited for ground points. This editing produced a DEM and DSM grid of 1-m resolution. The parameters of the geomorphometric model were generated using these high resolution data. These parameters include slope, curvature, OHM, OHM roughness, and topographic

wetness index. Based on the training samples of landslide polygons in 2009, modeled results give an overall accuracy of 65.8%. Because the recurrent rate from 2005~2009 is more than 55%, the model includes buffer zones of old landslides, river bank, and upstream erosions. To account for sliver noise, polygons smaller than 50 m² were filtered out. The accuracies of the model results improved to 76.6% and 72.5% when using training samples of landslide polygons in 2008 and 2009, respectively. These results show that the geomorphological model proposed is effective for landslide extraction.

To improve the model, other physiographical regions should be considered to calibrate the parameters. In addition, more parameters including hydrological conditions and geological environments should be considered to ensure the inclusion of all possible factors of susceptibility. Rainfall is one of the most important factors in hydrological conditions. The critical rainfall and rainfall intensity required to trigger a specific landslide is a challenge for future research. Soil moisture is another important factor in hydrology which might affect landslide occurrence and requires further study. The attitudes of geological formations and the strength of rock bodies are the major factors that should be considered for inclusion in the model. As the national Taiwanese LiDAR Project progresses, more datasets of multi-temporal and various physiographical settings are becoming available. Future research should also investigate the dependence of morphometric parameters on triggering events or geographical locations.

Chapter 6 Conclusions and Future Works

6.1 Conclusions and contributions

In conclusion, a comprehensive review and methods in using airborne LiDAR data for landslide investigations are made in this research. The methods developed in this research cover the areas for landslide detection, for landslide volume estimation and multi-temporal volume change analysis, and for establishing a landslide extracting model. Selected examples from both shallow and deep-seated landslides are used to demonstrate and prove the effectiveness for the cases in Taiwan and for the airborne LiDAR data acquired. Generally, it is proved airborne LiDAR data can be a good tool for extracting morphometric features of Taiwan landslides.

6.2 Recommendation for future study

Technique of OOA segmentation method for the detection of deep-seated landslides in dense forest should be developed especially for the high relief terrain of Taiwan. Uncertainties of LiDAR analysis due to adverse factors should be further explored to minimize the problem in multi-temporal change analysis. Future research should also investigate the dependence of morphometric parameters on triggering events or geographical locations. Another research area will be the application of full waveform to detect the

subtle reflection from the forest floor, thus to increase ground point densities of densely-vegetated area and to suppress the uncertainties of the DEM in this environment.

To improve the model for automatic extraction of landslides, other physiographical regions should be considered to calibrate the parameters. In addition, more parameters including hydrological conditions and geological environments should be considered to ensure the inclusion of all possible factors of susceptibility. Rainfall is one of the most important factors in hydrological conditions. The attitudes of geological formations and the strength of rock bodies are the major factors that should be considered for inclusion in the model.

Finally, a national geohazard mapping program employing integrated airborne LiDAR and digital photography was launched by the Central Geological Survey. The national mapping program, spanning 2010 to 2015, was dedicated to capture an entire territory of the country with airborne LiDAR and digital imagery with the aim to explore geological hazards (Liu and Fei, 2011). More datasets of multi-temporal and various physiographical settings are becoming available. More researches should investigate the dependence of morphometric parameters on triggering events and geographical locations.

References

1. Agliardi, F., Crosta, G. & Zanchi, A. (2001) "Structural constraints on deep-seated slope deformation kinematics", *Engineering Geology*, 59(1–2), pp. 83-102. doi: 10.1016/s0013-7952(00)00066-1
2. Agliardi, F., Crosta, G. B., Zanchi, A., & Ravazzi, C. (2009) "Onset and timing of deep-seated gravitational slope deformations in the eastern Alps, Italy", *Geomorphology*, 103(1), pp. 113-129. doi: 10.1016/j.geomorph.2007.09.015.
3. ASPRS (2008) "LAS Specification Version 1.2, Approved on 09/02/2008". American Society of Photogrammetry and Remote Sensing. http://www.asprs.org/society/committees/standards/asprs_las_format_v12.pdf
4. ASPRS (2009) "Lidar_exchange_format". http://www.asprs.org/society/committees/standards/lidar_exchange_format.html.
5. Ball, G. H. & Hall, D. J. (1965) "A Novel Method of Data Analysis and Pattern Classification", Menlo Park, CA, USA: Stanford Research Institute.
6. Bell, R., Jaboyedoff, M. & Glade, T. (2005) "Detecting landslide location and volume for hazard assessments using DTM analysis in the Swabian Alb,

- Germany", Geophysical Research Abstracts, Vol. 7, 06820, 2005. SRef-ID: 1607-7962/gra/EGU05-A-06820.
7. Bell, R., Jaboyedoff, M. & Glade, T. (2006) "Estimating the landslide volume of past and future events using high resolution DEM and the Sloping Local Base Level (SLBL) approach", Geophysical Research Abstracts, Vol. 8, 04155, 2006. SRef-ID: 1607-7962/gra/EGU06-A-04155.
8. Borghuis, A. M., Chang, K. T. & Lee, H. Y. (2007) "Comparison between automated and manual mapping of typhoon-triggered landslides from SPOT-5 imagery", International Journal of Remote Sensing, 28, pp. 1843-1856.
9. Burges, C. J. C. (1998) "A Tutorial on Support Vector Machines for Pattern Recognition", Data Mining Knowl. Discov, Vol.2, 1998, pp.121-167.
10. Casson, B., Delacourt, C. & Allemand, P. (2005) "Contribution of multi-temporal remote sensing images to characterize landslide slip surface—application to the La Clapiere landslide France", Natural Hazards and Earth System Sciences 5 (3), pp. 425–437.
11. Chang, K. J., Taboada, A. & Chan, Y. C. (2005) "Geological and morphological study of the Jiufengershan landslide triggered by the Chi-Chi

- Taiwan earthquake", *Geomorphology*, no.71, 2005, pp.293-309.
12. Chang, K. J., Taboada, A., Lin, M. L. & Chen, R. F. (2005) "Analysis of landsliding by earthquake shaking using a block-on-slope thermo-mechanical model: Example of Jiufengershan landslide, central Taiwan", *Engineering Geology*, no.80, pp.151-163.
13. Chang, K. T. & Liu, J. K. (2004) "Landslide features interpreted by neural network method", *Proc. The International Archives of the Photogrammetry, Remote Sensing and Spatial Information Sciences*, Vol. XX, Part B7, 2004, pp.574-579.
14. Chang, K. T., Liu, J. K., Chang, Y. M. & Kao, C. S. (2010) "An accuracy comparison for the landslide inventory with the BPNN and SVM methods", *Proc. Gi4DM 2010*, 2010.
15. Chang, K. T., Liu, J. K., Wang, Z. Y. & Kao, Q. X. (2010) "A comparison of two OOA segmentation methods for the detection of rainfall-induced landslides using airborne lidar nDSM data", *Proc. CACS 2010*, 2010, pp.295-298.
16. Chapelle, O., Haffner, P. & Vapnik, V. N. (1999) "Support vector machines for histogram-based image classification", *IEEE Transactions on Neural*

Networks, vol. 10 (5), 1999, pp. 1055– 1064.

17. Chen, J. M. & Black, T. A. (1992) "Defining leaf area index for non-flat leaves", *Agricultural and Forest Meteorology*, 57, pp. 1–12.
18. Chen, R. F., Chan, Y. C., Angelier, J., Hu, J. C., Huang, C., Chang, K. J. & Shih, T. Y. (2005) "Large earthquake-triggered landslides and mountain belt erosion The Tsaoling case, Taiwan", *C. R. Geoscience*, no.337, 2005, pp.1164-1172.
19. Chen, R. F., Chang, K. J., Angelier, J., Chan, Y. C., Deffontaines, B., Lee, C. T. & Lin, M. L. (2006) "Topographical changes revealed by high-resolution airborne LiDAR data: the 1999 Tsaoling landslide induced by the Chi-Chi earthquake", *Eng Geol*, 88, pp. 160–172. doi:10.1016/j.enggeo.2006.09.008
20. Cheng, J. D., Huang, Y. C., Wu, H. L., Yeh, J. L. & Chang, C. H. (2005) "Hydrometeorological and landuse attributes of debris flows and debris floods during typhoon Toraji, July 29-30, 2001 in central Taiwan", *Journal of Hydrology*, 306 (1-4), pp. 161-173.
21. Chigira, M. (2011) "Geological and Geomorphological Characteristics of Deep-Seated Catastrophic Landslides Induced by Rain and Earthquakes", *Journal of Chinese Soil and Water Conservation*, 42(4), pp. 3-16.

22. Chigira, M. & Kiho, K. (1994). "Deep-seated rockslide avalanches preceded by mass rock creep of sedimentary rocks in the Akaishi Mountains, central Japan", *Engineering Geology*, 38(3–4), pp. 221:230. doi: 10.1016/0013-7952(94)90039-6.
23. Chigira, M., Wang, W. N., Furuya, T. & Kamai, T. (2003) "Geological causes and geomorphological precursors of the Tsaoling landslide triggered by the 1999 Chi-Chi earthquake, Taiwan", *Engineering Geology*, 68(3–4), pp. 259:273. doi: 10.1016/s0013-7952(02)00232-6.
24. Chigira, M., & Yagi, H. (2006) "Geological and geomorphological characteristics of landslides triggered by the 2004 Mid Niigata prefecture earthquake in Japan", *Engineering Geology*, 82(4), pp. 202:221. doi: 10.1016/j.enggeo.2005.10.006.
25. Crosby, C. (2007) "GEON Points2Grid Utility Instructions". http://lidar.asu.edu/downloads/GEON_Points2Grid_Instructions.pdf.
26. Cruden, D.M. & Varnes, D.J. (1996) "Landslide Types and Processes", in Turner A. K. & Schuster, R. J. (eds.) "Landslides: Investigation and Mitigation" - Special Report 247: Washington, D.C., Transportation Research Board, National Research Council, pp. 36-75.

27. Dadson, S. J., Hovius, N., Chen, H., Dade, W. B., Lin, J. C., Hsu, M. L., Lin, C. W., Horng, M. J., Chen, T. C., Milliman, J. & Stark, C. P. (2004) "Earthquake- triggered increase in sediment delivery from an active mountain belt", *Geology*, 32(8), pp. 733–736.
28. Demoulin, A. (2006) "Monitoring and mapping landslide displacements: a combined DGPS stereophotogrammetric approach for detailed short- and long-term rate estimates", *Terra Nova* 18 (4), pp.290–298.
29. Densmore, A. L. & Hovius, N. (2000) "Topographic fingerprints of bedrock landslides", *Geology*. April 2000. 28(4), pp. 371–374.
30. Derron, M. H. & Jaboyedoff, M. (2010) "Preface to the special issue. In: LIDAR and DEM techniques for landslides monitoring and characterization", *Nat Hazards Earth Syst Sci*. 10, pp. 1877–1879.
31. Dewitte, O., Jasselette, J. C., Cornet, Y., Van Den Eeckhaut, M., Collignon, A. & Poesen, J., (2008) "Tracking landslide displacements by multi-temporal DTMs: A combined aerial stereophotogrammetric and LiDAR approach in western Belgium", *Engineering Geology*, 99(1–2), 11:22. doi: 10.1016/j.enggeo.2008.02.006.
32. Dietrich, W. E. & Perron, J. T. (2006) "The search for a topographic signature

- of life", *Nature*, 439 (7075), pp. 411-418. 26 January 2006.
doi:10.1038/nature04452.
33. Dilley, M., Chen, R. S., Deichmann, U., Lerner-Lam, A. L. & Arnold, M. (2005) "Natural Disaster Hotspots: A Global Risk Analysis", *Disaster Risk Management Series No.5*. The World Bank. 145 p. 2005. ISSN: 0821359304. ISBN-13: 978-0-8213-5930-3.
34. Dong, J. J., Li, Y. S., Kuo, C. Y., Sung, R. T., Li, M. H., Lee, C. T., Chen, C. C. & Lee, W. R. (2011) "The formation and breach of a short-lived landslide dam at Hsiaolin village, Taiwan - Part I: Post-event reconstruction of dam geometry", *Engineering Geology*, *Engineering Geology*, 123(1-2), pp. 40-59. Jul. 2011, doi: 10.1016/j.enggeo.2011.04.001.
35. Dramis, F. & Sorriso-Valvo, M. (1994) "Deep-seated gravitational slope deformations, related landslides and tectonics", *Engineering Geology*, 38(3-4), pp. 231:243. doi: 10.1016/0013-7952(94)90040-x.
36. Dubayah, R. & Blair, J. (2000) "Lidar remote sensing for forestry applications", *J. of Forestry*, 98(6), pp. 44-46.
37. Glenn, N. F., Streutker, D. R., Chadwick, D. J., Thackray, G. D. & Dorsch, S.

- J. (2006) "Analysis of LiDAR-derived topographic information for characterizing and differentiating landslide morphology and activity", *Geomorphology*, 73(1:2), pp.131:148. doi: 10.1016/j.geomorph.2005.07.006.
38. Gonzalez, R. C. & Woods, R. E. (2002) "Digital Image Processing (second edition)", Prentice Hall, 2002, 793 pp.
39. Guth, P. L. (2001) "Quantifying terrain fabric in digital elevation models," in Ehlen, J. & Harmon, R. S., (eds.) "The environmental legacy of military operations", Geological Society of America. *Reviews in Engineering Geology*, 14:13-25.
40. Guth, P. L. (2003) "Eigenvector analysis of digital elevation models in a GIS", In: Evans, I. S., Dikau, R., Tokunaga, E., Ohmori, H. & Hirano, M. (Eds.) "Geomorphometry and Quality Control, in Concepts and Modeling in Geomorphology: International Perspectives", pp.199-220, TerraPub, Tokyo.
41. Guzzetti, F., Ardizzone, F., Cardinali, M., Galli, M. & Reichenbach, P. (2008) "Distribution of landslides in the Upper Tiber River basin, central Italy", *Geomorphology*, 96, 105–122.
42. Guzzetti, F., Ardizzone, F., Cardinali, M., Galli, M., Rossi, M. & Valigi, D. (2009) "Landslide volumes and landslide mobilization rates in Umbria,

- central Italy", *Earth and Planetary Sciences Letters*, 279, pp. 222–229.
DOI:10.1016/j.epsl.2009.01.005.
43. Guzzetti, F., Mondini, A. C., Cardinali, M., Fiorucci, F., Santangelo, M. & Chang, K. T. (2012) "Landslide inventory maps: New tools for an old problem", *Earth-Sci. Rev.* (2012), DOI:10.1016/j.earscirev.2012.02.001.
44. Heidemann, H. K. (2012) "Lidar base specification version 1.0", U.S. Geological Survey Techniques and Methods, book 11, chap. B3, 63 p.
45. Hengl, T. & Reuter, H. I. (eds.) (2009) "Geomorphometry - concepts, software, applications", *Series Developments in Soil Science*, 33, Elsevier, ISBN 9780123743459.
46. Herva, J., Barredo, J. I., Rosin, P. L., Pasuto, A., Mantovani, F. & Silvano, S. (2003) "Monitoring landslides from optical remotely sensed imagery: the case history of Tessina landslide, Italy", *Geomorphology*, 54 (1-2), pp. 63-75.
47. Highland, L. M. & Bobrowsky, P. (2008) "The landslide handbook—A guide to understanding landslides", Reston, Virginia, U.S. Geological Survey Circular 1325, 129 p.
48. Hopkinson, C. (2006) "The Influence of LiDAR Acquisition Settings on Canopy Penetration and Laser Pulse Return Characteristics", *International*

- Geoscience and Remote Sensing Symposium, 2006. IGARSS 2006. IEEE International Conference on July 31 2006-Aug. 4 2006, pp. 2420 - 2423. Digital Object Identifier 10.1109/IGARSS.2006.627.
49. Hsu, W. C., Wu, L. W. & Liu, J. K. (2012) "Airborne LiDAR survey in cloudy and extremely high-relief mountainous terrain of Taiwan", IGARSS 2012: 2679-2682.
50. Hu, J. C., Tang, C. L., Lo, C. M., Lin, M. L., Dong, J. J. & Lee, C. T (2010) "Catastrophic Hsiaolin landslide in southern Taiwan triggered by Morakot Typhoon: Insights from 3-D discrete element simulation", Geophysical Research Abstracts, Vol. 12, EGU2010-6192, 2010. EGU General Assembly 2010.
51. Huang, C.M. & Shih, T.Y. (2008) "On the Laser Incidence Angle and Airborne LiDAR Penetration Rate", Journal of Photogrammetry and Remote Sensing, 13(1), pp. 67-73. March 2008.
52. Hwang, J. T. & Chiang, H. C. (2010) "The study of high resolution satellite image classification based on Support Vector Machine", Proc. The 18th International Conference on Geoinformatics, 2010.
53. IAEG Commission on Landslides (1990) "Suggested nomenclature for

- landslides", *Bull. Int. Assoc. Eng. Geol.* 41, 13–16.
54. ITRI (1993) "A report on general investigation and mitigation scheme for Li-Shan Landslide", Soil and Water Conservation Service, Council of Agriculture. Miao-bin Su; Deng-wen Xu; Ke-jian Shou, 2003. Pictorial Book of the Mitigation Plan of Li-Shan Landslides. Soil and Water Conservation Service, Council of Agriculture. (in Chinese)
55. Jaboyedoff, M., Pedrazzini, A., Loye, A., Oppikofer, T. & Guell-i-Pons, M. (2009) "Earth flow in a complex geological environment: the example of Pont Bourquin, Les Diablerets (Western Switzerland)". In: Malet, J. P., Rematre, A, Bogaard, T. (eds) "Landslides processes—from geomorphologic mapping to dynamic modeling", proceedings of the landslide processes conference, 6–7 February 2009, Strasbourg, France.
56. Jaboyedoff, M., Oppikofer, T. & Abellan, A. (2010) "Use of LIDAR in landslide investigations: a review", Institute of Geomatics and Risk Analysis, University of Lausanne. Springerlink.com.
57. Jaboyedoff, M., Oppikofer, T., Abellan, A., Derron, M., Loye, A., Metzger, R. & Pedrazzini, A. (2012) "Use of LIDAR in landslide investigations: a review", *Nat Hazards* (2012) 61:5–28. DOI 10.1007/s11069-010-9634-2.

58. Jackson, R. D., Slater, P. N. & Pinter, P. J. (1983) "Discrimination of growth and water stress in wheat by various vegetation indices through clear and turbid atmospheres", *Remote Sensing of Environment*, 15, pp. 187-208.
59. Jain, A. K. & Dubes, R. C. (1988) "Algorithms for Clustering Data", Prentice Hall, Inc.
60. Juang, C. H. & Lee, W. F. editors (2011) "Reconnaissance of Extreme Natural Disasters of Morakot Typhoon, Taiwan", *Engineering Geology*, 123(1–2), pp. 1-148 (11 November 2011).
61. Joyce, K. E., Belliss, S. E., Samsonov, S. V., McNeill, S. J. & Glassey, P. J. (2009) "A review of the status of satellite remote sensing and image processing techniques for mapping natural hazards and disasters Progress", *Physical Geography*, 33(2) , pp. 183–207.
62. Kalderon-Asael, B., Katz, O., Aharonov, E. & Marco, S. (2008) "Modeling the Relation between Area and Volume of Landslides", in: *the Preparation for Earthquakes Report*, GSI/06/2008, Jerusalem, April 2008.
http://www.gsi.gov.il/Eng/_Uploads/348GSI-06-2008.pdf.
63. Kerle, N. & Martha, T. R. (2010) "The potential of object-based and cognitive methods for rapid detection and characterization of landslides",

Proc. Gi4DM 2010, 2010.

64. Kirkby, M. J. (1975) "Hydrograph modeling strategies", in: Peel, R., Chisholm, M., and Haggett, P. (Eds.) "Process in physical and human geography", Heinemann, London, pp. 69-90.
65. Kohavi, R. & Provost, F. (1998) "The case against accuracy estimation for comparing classifiers", Proceedings of the Fifteenth International Conference on Machine Learning, Morgan Kaufmann, San Francisco, CA.
66. Lewis, D. (2006) "Statewide LIDAR mapping proposal- Seeing landslides with LIDAR", Cascadia, 4 (2), P.1, Fall 2006. www.OregonGeology.com
67. Lin, C. W., Liu, S. H., Lee, S. Y. & Liu, C. C. (2006) "Impacts of the Chi-Chi earthquake on subsequent rainfall-induced landslides in central Taiwan", Engineering Geology, 86 (2-3), pp.87-101.
68. Lin, C. W., Chang, W. S., Liu, S. H., Tsai, T. T., Lee, S. P., Tsang, Y. C., Shieh, C. L. & Tseng, C. M. (2011) "Landslides triggered by the 7 August 2009 Typhoon Morakot in southern Taiwan", Engineering Geology, Vol. 123, Issue 1-2, Jul. 2011, 3-12.
69. Lin, M. L. & Jeng, F. S. (2000) "Characteristics of hazards induced by extremely heavy rainfall in Central Taiwan - Typhoon Herb", Engineering

Geology, 58 (2), pp. 191-207.

70. Liu, H. Q. & Huete, A. R. (1995) "A feedback based modification of the NDVI to minimize canopy background and atmospheric noise", IEEE Trans. on Geoscience and Remote Sensing, 33. pp. 457-465.
71. Liu, J. K. (1987) "Automation for landslide analysis using digital images", Remote Sensing, 1987, Vol. 8, pp. 60-90. (in Chinese)
72. Liu, J. K., Chang, K. T., Rau, J. Y., Hsu, W. C., Liao, Z. Y., Lau, C.C. & Shih, T. Y. (2009) "The geomorphometry of rainfall-Induced landslides in Taiwan obtained by airborne LiDAR and digital photography", In: Chapter 6 of Geoscience and Remote Sensing (Text book) published by In Tech on 2009/10, editor-in-Chief Pei-Gee Peter Ho. P.115-132.
73. Liu, J. K., Hsu, W. C., Chan, Y. C., Hsieh, Y. C. & Shih, T. Y. (2010) "On deriving an enhanced map of shallow-seated landslides from LiDAR DSM and DEM", Proc. 2010 RSATS Conference, 2010.
74. Liu, J.K., Lin, C.W, Tseng, C.M. & Huang, M.L (2010) "The Major Pitfalls of Voids and Artifacts for Volume Estimation of Landslides Using LiDAR DEMs", Proceedings of Asia GIS 2010 International Conference. Paper # 4R403A01.pdf.

75. Liu, J. K. & Fei, L. Y. (2011) "Taiwanese LiDAR project", GIM International, Volume 25, Issue 8, August 2011. ISSN: 15669076. CODEN: GIINA (2011).
76. Liu, J. K., Hsu, W. C., Yang, M. S., Shieh, Y. C. & Shih, T. Y. (2010) "Landslide Detection by Indices of LiDAR Point-cloud Density", IGARSS 2010, July 25 - 30, 2010. Honolulu, Hawaii, USA.
77. Liu, J.K., Hsu, W.C. & Shih, T.Y. (2011) "Volume estimation of Hsiaolin Landslide using LiDAR DEMs before and after Morakot event", IGARSS 2011, July 24 - 31, 2011. Vancouver, CANADA.
78. Liu, J. K., Hsu, W. C. & Shih, T. Y. (2012) "Characterize Landslide Size Caused by Heavy Rainfall and Earthquake with Satellite Images", Proceedings of the 31th Conference on Surveying and Geomatics, 27-28 September 2012, Chinese Culture University. (in Chinese)
79. Liu, X., Zhang, Z., Peterson, J. & Chandra, S. (2007) "The effect of LiDAR data density on DEM Accuracy", In: MODSIM07 International Congress on Modelling and Simulation, 10-13 Dec 2007, Christchurch, New Zealand
80. Lo, C. M., Lin, M. L., Dong, J. J., Chang, K. T., Chien, S. Y. & Huang, A. B. (2009) "Landslide Characterization and Zonation of Hungtsaiping Area Based on Topography, Image of Remote Sensing and PIV Technology",

Journal of the Chinese Institute of Civil & Hydraulic Engineering. Vol.21,
No.2. (2009/06), pp. 113-128.

81. Mckean, J. & Roering, J. (2004) "Objective landslide detection and surface morphology mapping using high-resolution airborne laser altimetry", *Geomorphology*, 57 (2004) , pp. 331-351.
82. Means, J.E., Acker, S.A., Fitt, B.J., Renslow, M., Emerson, L. & Hendrix, C.J. (2000) "Predicting forest stand characteristics with airborne scanning LiDAR", *Photog. Eng. & Remote Sensing*, 66(11), pp. 1367- 1371.
83. Mikos, M., Fazarinc, R. & Ribicic, M. (2006) "Sediment production and delivery from recent large landslides and earthquake-induced rock falls in the Upper Soca River Valley, Slovenia", *Engineering Geology*, 86 (2-3), pp. 198-210.
84. MOI (2006) "High Accuracy and High Resolution DEM Mapping and Database Establishment for Selected LiDAR Survey Areas and the Development of their Applications - Final Report". 315p. Ministry of The Interior, ROC. (in Chinese)
85. Naesset, E. (2002) "Predicting forest stand characteristics with airborne scanning laser using a practical two-stage procedure and field data", *Remote*

Sensing of Environment, 80(1), pp. 88-99(12).

86. NFA (2012) "Historical records of natural disasters of Taiwan from 1958 to 2011", National Fire Agency, Ministry of the Interior. <http://www.nfa.gov.tw/Show.aspx?MID=97&UID=827&PID=97>. (in Chinese).
87. Parker, J. R. (1997) "Algorithms for Image Processing and Computer Vision", Wiley Computer, New York.
88. Pike, R. J. (1988) "The geometric signature: quantifying landslide-terrain types from digital elevation models", *Mathematical Geology*. 20(5), pp. 491 - 511. ISSN: 0882-8121 (Paper) 1573-8868 (Online). DOI: 10.1007/BF00890333. Publisher: Springer Netherlands.
89. Pike R. J. (2000) "Geomorphometry — diversity in quantitative surface analysis", *Progress in Physical Geography*. 2000; 24:1–20.
90. Pirotti, F. & Tarolli, P. (2010) "Suitability of LiDAR point density and derived landform curvature maps for channel network extraction", *Hydrological Processes*, 24, pp. 1187-1197, doi:10.1002/hyp.7582.
91. Puetz, A. M., Chris, O. R. & Brian, A. (ed.) (2009) "Effects of LiDAR point density on bare earth extraction and DEM creation", in *Laser Radar*

Technology and Applications XIV. Proceedings of the SPIE, Volume 7323, pp. 73230I-73230I-8 (2009).

92. PWRI (2008) "Guidelines for the detection of streams vulnerable to deep-seated landslides", Volcano and debris flow research team, Public Works Research Institute (PWRI), Japan.
93. Raber, G. (2003) "The effect of lidar posting density on dem accuracy and flood extent delineation--a gis-simulation approach", NASA Affiliated Research Center, Department Of Geography, University of South Carolina.
94. Raju, P. & Saibaba, J. (1999) "Landslide hazard zonation mapping using remote sensing and geographic information system techniques - a case study of Pithoragarh area, U. P.", IEEE 1999 International Geoscience and Remote Sensing Symposium. IGARSS '99 Proceedings, pp. 577-579.
95. Rau, J. Y., Chen, L. C., Liu, J. K. & Wu, T. H. (2007) "Dynamics monitoring and disaster assessment for watershed management using time-series satellite images", IEEE Transactions on Geoscience and Remote Sensing, 45, pp.1641-1649.
96. Research System, Inc. (2006) "ENVI Online Help".
97. Roth, R. & Thompson, J. (2008) "Practical Applications of Multiple Pulses In

- Air (MPIA) LIDAR In Large Area Surveys", Proceedings of XXI Congress of ISPRS, July 2008.
98. Roth, R. (2010) "Technology Challenges and Options for high-point-density LIDAR", European LIDAR Mapping Forum, December 2010.
99. Roth, R. (2011) "Leica ALS70 – Point Density Multiplication for High Density Surface Acquisition", 53rd Photogrammetric Week: Multi-ray Photogrammetry, Stuttgart, September 2011.
100. Schmidt, J., Evans, I. S. & Brinkmann, J. (2003) "Comparison of polynomial models for land surface curvature calculation", International Journal of Geographical Information Science, 17(8), pp. 797-814.
101. Schulz, W. H. (2007) "Landslide susceptibility revealed by LIDAR imagery and historical records, Seattle, Washington", Engineering Geology, Vol.89, Issues 1-2, 12 January 2007, Pages 67-87. doi:10.1016/j.enggeo.2006.09.019.
102. Sharpnack, D. A. & Akin, G. (1969) "An algorithm for computing slope and aspect from elevations", Photogrammetric Engineering, 35(3), pp. 247-248.
103. Shih, T. Y. & Huang, C.M. (2006) "Airborne Lidar Point Cloud Density Indices", American Geophysical Union, Fall Meeting 2006, abstract #G53C-0919. 12/2006. 2006AGUFM. G53C0919S.

104. Song, Q. C., Lin, C. W., Lin, W. X. & Lin, W. Z. (2000) "Geological Description of the Geological Map: Chia-Xian", in 1/50000 Geological Map Series, The Central Geological Survey. (in Chinese)
105. Stefano, C. D., Ferro, V., Porto, P. & Tusa, G. (2000) "Slope curvature influence on soil erosion and deposition processes", Water Resources Research, Vol. 36, No. 2, pp. 607-617.
106. SWCS (1992) "Manual for landslide investigation, planning and design". Soil and water conservation Service (SWCS), Council of Agriculture, Taiwan. (in Chinese)
107. SWCB (2010) "Airborne LiDAR Data for Installing a Landslide Geomorphometric Model - Final Report", Soil and Water Conservation Bureau. Reported by LiDAR Team of Industrial Technology Research Institute. 179 p. (in Chinese)
108. SWCB (2010) "Applications of Satellite Imagery and LiDAR DEM for Characterizing the Origin of Debris flows - Final Report", 359p. Soil and Water Conservation Bureau (SWCB), Agriculture Council, ROC. (in Chinese)
109. Tarchi, D., Casagli, N., Fanti, R., Leva, D. D., Luzi, G., Pasuto, A., Pieraccini,

- M. & Silvano, S. (2003) "Landslide monitoring by using ground-based SAR interferometry: an example of application to the Tessina landslide in Italy", *Engineering Geology*, 68(1-2), pp. 15-30.
110. Tarolli, P., Borga, M., Chang, K. T. & Chiang, S. H. (2011) "Modelling shallow landsliding susceptibility by incorporating heavy rainfall statistical properties", *Geomorphology*, 133, 3-4, pp. 199-211.
111. Teeuw, R. M. (2007) editor, "Mapping Hazardous Terrain Using Remote Sensing", Special publication, Geological Society of London, Geological Society Special Publication No. 283. 169 p. Geological Society, 2007. ISBN: 1862392293, 9781862392298.
112. Tseng, C. H., Hu, J. C., Chan, Y. C., Chu, H. T., Lee, J. F., Wei, J. Y., Lu, C. Y. & Lin, M. L. (2007) "Non-catastrophic landslides induced by the Mw 7.6 Chi-Chi earthquake in central Taiwan as revealed by PIV analysis", *Tectonophysics*. DOI:10.1016/j.tecto.2007.11.019
113. Tseng, C.M., Lin, C.W. & Liu, J.K., (2011) "Application of High-resolution LiDAR-derived DEM in Landslide Volume Estimation", *Geophysical Research Abstracts*. Vol. 13, EGU2011-5193, 2011. EGU General Assembly 2011, Vienna, AUSTRIA.

114. Turner, A. K. & Schuster, R. L. (1996) "Landslides— Investigation and Mitigation", National Research Council, Transportation Research Board Special Report 247, National Academy Press, Washington, D.C., 673 p.
115. Van Den Eeckhaut, M., Poesen, J., Verstraeten, G., Vanacker, V., Moeyersons, J., Nyssen, J. & van Beek, L.P.H. (2005) "The effectiveness of hillshade maps and expert knowledge in mapping old deep-seated landslides". *Geomorphology*, 67 (3–4), 351–363.
116. Van Den Eeckhaut, M., Poesen, J., Verstraeten, G, Vanacker, V., Nyssen, J., Moeyersons, J., van Beek, L. P. H. & Vandekerckhove, L. (2007) "Use of LIDAR-derived images for mapping old landslides under forest. *Earth Surface*", *Processes and Landforms*, 32(5):754 - 769.
117. Van Westen, C. J., van Asch, Th. W. J. and Soeters, R. (2005) "Landslide hazard and risk zonation : why is it still so difficult?", In: *Bulletin of engineering geology and the environment IAEG*, 65 (2005) 2, pp. 167-184.
118. Venables, W. N. & Ripley, B. D. (2002) "Modern Applied Statistics with S", Fourth edition. Springer. 495 p.
119. Varnes, D. J. (1978) "Slope movement types and processes", in Schuster, R., and Krizek, R., eds., "Landslides: Analysis and Control", Washington, D.C.,

National Academy of Science, pp. 12-33

120. Ventura, G., Vilardo, G., Terranova, C., & Sessa, E. B. (2011) "Tracking and evolution of complex active landslides by multi-temporal airborne LiDAR data: The Montaguto landslide (Southern Italy)", *Remote Sensing of Environment*, 115(12), 3237:3248. doi: 10.1016/j.rse.2011.07.007.
121. Wilson, J. P. & Gallant, J. C. (2000) "Terrain Analysis", John Wiley & Sons, Inc., 479 p.
122. Witten, I. H. & Frank, E. (2000) "Data mining: Practical machine learning tools and techniques", Morgan Kaufmann, 2011. ISBN: 0123748569. 664p.
123. Woodcock, N. H. (1977) "Specification of fabric shapes using an eigenvalue method", *Geol. Soc. Amer. Bull.* 88, pp. 1231–1236.
124. Yang, M. S., Lin, M. C., Liu, J. K. & Wu, M. C. (2010) "Automatic image classification of landslides improved with terrain roughness indices in various kernel sizes", 01/2010; In proceeding of: IEEE International Geoscience & Remote Sensing Symposium, IGARSS 2010, July 25-30, 2010, Honolulu, Hawaii, USA.
125. Zhou, Q. & Liu. X. (2006) "Digital Terrain Analysis", Science Publisher, Beijing China. ISBN : 7030168852.

Appendix 1 Acronym

Acronym	Definition
ASCII	American Standard Code for Information Interchange
ASPRS	American Society of Photogrammetry and Remote Sensing
CGS	Central Geological Survey
CHM	Canopy Height Model
DBM	Digital Building Model
DEM	Digital Elevation Model
DHM	Digital Height Model
DOM	Digital Orthophoto Map
DSM	Digital Surface Model
DTED	Digital Terrain Elevation Data
DTM	Digital Terrain Model
GCPs	Ground Control Points
GIS	Geographical Information System
GPS	Global Positioning System
IAEG	International Association of Engineering Geologists
IMG	ERDAS IMAGINE file format
IMU	Inertial Measurement Unit
LAS	LASer file format
LiDAR	Light Detection and Ranging
MOI	Ministry of the Interior
NSDI	National Spatial Database Infrastructure
OHM	Object Height Model
POS	Positioning and Orientation System
RMSE	Root Mean Square Error
SVM	Support Vector Machine
TIN	Triangulated Irregular Network
TWD97	Taiwan Geodetic Datum 1997
TWVD2001	Taiwan Vertical Datum 2001
USGS	US Geological Survey

個人簡歷

姓 名：劉進金 (Jin-King Liu)

出生地：台灣彰化

出生日期：1954 年 6 月 2 日

通訊地址：新竹市 30069 光復路二段 882 號 8F-2

phone: +886-3-6589495

email: JKLIU@lidar.com.tw

現 職：達雲科技有限公司執行長 (2010-P)

學 歷：

1977 國立成功大學地球科學系學士畢

1980 荷蘭國際航空太空暨地球科學研究院畢

1985 英國倫敦大學遙測學碩士畢

2013 國立交通大學土木工程博士畢

經 歷：

1977 工業技術研究院礦業研究所遙測小組技術員

1981 工業技術研究院礦業研究所遙測小組助理研究員

1984 工業技術研究院能源與礦業研究所海外礦業發展室副研究員

1988 工業技術研究院能源與礦業研究所海外礦業發展室研究員

1991 工業技術研究院能源與資源研究所遙測技術研究室研究員兼副主任代理主任

1994 工業技術研究院能源與資源研究所土地資源研究室研究員兼副主任

1996 工業技術研究院能源與資源研究所礦產資源研究室研究員兼主任

2001 工業技術研究院能源與資源研究所礦產資源研究室正研究員兼主任

2002 工業技術研究院能源與資源研究所遙測與資訊技術研究室正研究員兼主任

2004 工業技術研究院能源與資源研究所永續資源組正研究員

2006 工業技術研究院能源與環境研究所遙測與資源資訊研究室正研究員